ABSTRACT

Title of Dissertation:	MICROFABRICATION OF X-RAY OPTICS FOR MICROSCOPY AND PHASE CONTRAST IMAGING
	Mona Mirzaeimoghri, Doctor of Philosophy, 2018
Dissertation directed by:	Dr. Don DeVoe, Department of Mechanical Engineering
	Dr. Han Wen, National Institute of Health

The short wavelength of x-ray radiation (λ = 10Å to λ = 0.1Å) gives it the ability to penetrate deeper into matter and makes it highly useful for applications in microanalysis and imaging, where it is desirable to probe beyond the surface of the material under analysis. Hard x-rays generally refer to photon energies above 10keV, while soft x-rays are between 0.1 and 10 keV. This dissertation investigates the development of two types of optical elements suitable for hard x-ray imaging: compound refractive lenses for hard x-ray microscopy and diffraction gratings for hard x-ray phase contrast imaging.

Hard x-ray lenses are useful elements in x-ray microscopy and in creating focused illumination for analytical applications such as x-ray fluorescence imaging. Recently, polymer compound refractive lenses for focused illumination in the soft x-ray regime (< 10 keV) have been created with nano-printing. However, there are no such lenses yet for hard x-rays, particularly of short focal lengths for benchtop microscopy. In the first section of this dissertation, I report the first

instance of a nano-printed lens for hard x-ray microscopy, and evaluate its imaging performance. The lens consists of a spherically focusing compound refractive lens designed for 22 keV photon energy, with a tightly packed structure to provide a short total length of 1.8 mm and a focal length of 21.5 mm. The resulting lens technology was found to enable benchtop microscopy at 74x magnification and 1.1 μm pixel resolution. It was used to image and evaluate the focal spots of tungsten-anode micro-focus x-ray sources.

In the second section of the dissertation, I describe the fabrication of nanometric x-ray gratings that will advance x-ray phase contrast imaging technologies. X-ray phase contrast imaging, unlike conventional x-ray attenuation imaging, measures the phase shift and scattering of the wavefront by the imaged material. High quality x-ray gratings are essential components in benchtop phase contrast imaging systems. Fabrication of such gratings is challenging, especially when the pitch of the gratings shrinks to less than half a micrometer. The fabrication of x-ray gratings typically involves creating a free-standing high-aspect-ratio mold, which is then filled with high atomic number elements. I report the fabrication of silicon grating molds of 400 nm pitch and up to 10 μm height, achieving a structural aspect ratio of 50. The technology of deep silicon etching was based on the Bosch process with a novel and optimized two-layer masking process.

MICROFABRICATION OF X-RAY OPTICS FOR MICROSCOPY AND PHASE CONTRAST IMAGING

by

Mona Mirzaeimoghri

Dissertation submitted to the Faculty of the Graduate School of the
University of Maryland, College Park, in partial fulfillment
of the requirements for the degree of
Doctor of Philosophy
2018

Advisory Committee:
Professor Don L DeVoe (Chair)
Dr. Han Wen
Professor Sarah Bergbreiter
Professor Miao Yu
Professor Ryan Sochol
Professor Pamela Abshire

To my parents, Es'hagh and Hannah

Acknowledgment

First and foremost I would like to express my sincere gratitude to my advisors, Dr. Han Wen and Prof. Don L. DeVoe, for their continuous support of my Ph.D. study and its related research. Under their supervision, I learned how to see the big picture and define a research problem of my own, find a solution and patiently analyze the result and most importantly I learned how to explore different angles of the problem. I was very lucky to have them as my mentors for my Ph.D. study, especially on tough and low days when I was so close to give up.

Besides my advisors, I would like to thank the rest of my thesis committee, Prof. Sarah Bergbreiter, Prof. Miao Yu, Prof. Ryan Sochol, and Prof. Pamela Abshire, for their insightful questions and invaluable comments that widen my research from various perspectives.

I thank my fellow labmates, Prakruthi Hareesh, Alex Sposito, Omid Rahmanian, and Jung Yeon Han, for all the supports they provided in the last 5 years and for all the fun we had before and after weekly lab meetings. The discussions about the research, the encouragement during the problems, and most importantly, our talks about TV series made the lab fun and memorable for me.

14 years ago, in a cold dark winter morning, at 5 am, my father was taking me to a class that I needed to take while preparing for the university entrance exam. I remember he told me to always dedicate a percentage of my income into buying books and never give up learning. Now my father does not know that I got my Ph.D. due to the Alzheimer's disease and I do not know if he will ever know, but I would like to thank him, my mom, and especially Es'hagh who has been always supportive, understanding and caring in my journey of learning.

Table of Contents

List of Figures

Chapter 1. Introduction

The electromagnetic spectrum comprises the full range of electromagnetic radiation wavelengths, including microwave, visible light, ultra violet, etc. (Figure 1). Within the space separating ultra violet and gamma radiation in the electromagnetic spectrum, x-rays exist with a photon energy (E) of a few hundred eV up to several hundred keV and wavelength of λ = 10Å (E= 1.24 keV) to λ = 0.1Å (E= 124 keV). Hard x-rays generally refer to photon energies above 10keV while soft x-rays are between 0.1 and 10 keV. Compared to visible light with wavelengths of 400 nm to 700 nm, x-rays have shorter wavelengths which give them a different behavior when interacting with materials. In particular, the ability of shorter wavelength radiation to penetrate deeper into matter makes x-ray radiation highly useful for applications in microanalysis and imaging where it is desirable to probe beyond the surface of the material under analysis.

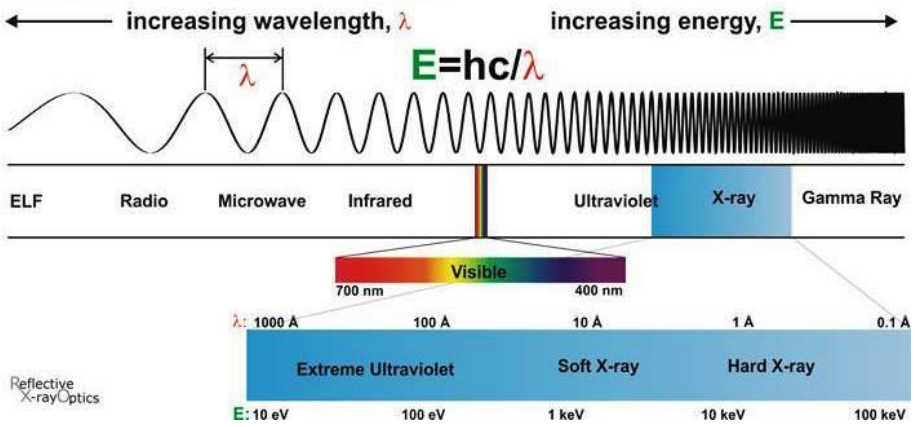

Figure 1. *Electromagnetic spectrum Source: http://www.rxollc.com/technology/index.html*

Since the time that W. Rontgen passed x-ray photons throw his wife's hand[1] and depicted the first shadow grams of the internal bone structure, x-rays have played a major role in medical

imaging procedures. However, the ionizing effects of short wavelength radiation can cause harmful damage to the human body, and thus poses a major health concern. Absorption of radiation can lead to complications such as changes in blood cell counts, skin reddening, cataracts, and cancer[2]. To reduce the harmful effects of x-rays on human tissues associated with direct intensity-based imaging, a variety of phase contrast imaging methods have been developed. X-ray phase contrast imaging refers to imaging techniques that are sensitive to the wave characteristics of x-rays. They directly or indirectly detect the diffraction and scattering of the electromagnetic wave, which can occur independently from intensity attenuation. It is a fundamental way to mitigate the harmful effects of radiation and has been proposed as early as the 1960s when the first x-ray interferometers were realized. The penetrating power and short wavelengths of x-rays lead to some advantages when applied to microscopy. The first is the ability to see through thick and opaque objects, and the second is a high diffraction limit of attainable resolution. For the first section of this dissertation research I propose to produce micro and nano optical elements that will advance imaging technologies in the above two areas.

The most sensitive x-ray phase contrast imaging techniques belong to the general category of interferometry. Michelson-Morley[3] and the Mach-Zehnder[4] interferometers are one the first demonstrations of phase contrast measurement using achromatic two-beam visible light. The first x-ray version of the phase contrast interferometer, shown by Bonse and Hart in the 1960s[5], used Bragg diffraction within monolithic crystals to split and recombine the beams. It provides the highest measured phase shift in interferometry. However, crystals require collimated and monochromatic beams which are not available from compact sources. Replacing the crystals with diffraction gratings relaxed these requirements. The first example was the x-ray Talbot-Lau interferometer proposed by J. Clauser in 1998[6]. However, the sensitivity of grating approaches is

determined by the ratio of wave propagation distance/grating period. The Talbot-Lau method is limited in sensitivity due to the need for absorption gratings, which cannot be made to very small periods for hard x-rays[7,8]. A more recent development in far-field interferometry with only phase gratings managed to overcome the sensitivity limitation. It uses phase gratings of sub-micron periods and takes advantage of a recently discovered phase Moiré effect, which, together with the classic Moiré effect, is a part of a universal Moiré effect[9].

Since the 1980s silicon and polymer based micro and nanofabrication technologies have been used in x-ray optics applications, resulting in significant improvements in resolution, precision and efficiency for x-ray diffractive and reflective optics. Advances in nanofabrication techniques, high precision lithography, and thin-film deposition have allowed the improvement of the x-ray optics over time[10]. High aspect ratio gratings[7], zone plates, multilayer Laue lens[11], reflective lens microscope[12], full-field x-ray microscope[13], micro x-ray fluorescence spectroscopy[14], scanning photoemission microscopy[15] and synchrotron radiation x-ray tomographic microscopy[16] are different types of optics that have been adopted for use with both soft and hard x-rays.

Microscopy in the hard x-ray photon energy regime (>10 keV) can take on a number of basic designs, such as projection magnification in a cone-beam, geometric magnification in a pinhole camera, and magnification based on a focusing element. The use of a focusing element offers several advantages by obviating the need for a small source spot for its resolution, allowing direct imaging of a light emitting object such as the focal spot of an x-ray tube, and supporting higher x-ray flux than a pinhole camera for faster imaging.

Focusing elements for x-ray microscopy up to 10 keV photon energy include Kirkpatrick-Baez mirrors in benchtop microscopy [17], zone plates at 8 keV [18] and compound refractive lenses (CRL) which consist of linear arrays of individual refractive lenses [12]. The first CRLs were lines of cylindrical holes drilled into aluminum blocks [12], where the small refractions of individual holes were compounded to achieve a substantial focusing effect [2]. Since this initial demonstration, CRL technology has been further developed through different designs, including parabolic [19], spherical [20], and kinoform [21] CRLs. Low-attenuation materials such as Al [12], Be [22], Si [23], C [24] and polymers[2520] together with different fabrication techniques [26], have been explored.

Miniature CRLs have particularly advantages for benchtop x-ray microscopy in the 10s of keV energy range with high magnification and short exposure times. High magnification is desirable for hard x-rays since efficient detectors in this energy range have relatively large pixel sizes, implying the need for high magnification factors to achieve high resolution. High magnification translates to short focal length of the focusing element. Furthermore, a larger numerical aperture is also desired to collect more light and shorten the exposure time. For a parabolic CRL of a fixed total length L, the focal length f scales with R^2, where R is the lens radius, while the numerical aperture scales with 1/R. Thus, miniature CRLs are desirable for hard x-ray microscopy at high magnifications.

Conventional microfabrication methods employed for lens patterning, including Si deep reactive-ion etching (DRIE) [27], diamond micromachining [28], and x-ray lithography, have provided lens radii down to a few micrometers [29,30]. However, inherent limitations of conventional microfabrication techniques meant that they only make cylindrically-focusing CRLs, thus requiring an inline arrangement of two perpendicular CRLs to achieve spherical focusing,

thereby doubling the total length of the CRL. Although not an issue for focusing a collimated beam into a spot, for microscopy and imaging applications, this design halves the imaging field of view (FOV) if the two CRLs are interleaved, due to the inverse relationship between FOV and the total length of each CRL. The alternative sequential arrangement leads to different magnification factors for the two directions. Such a combination also causes directional asymmetry of the lens point-spread function and lens aberration effects. To overcome these issues, spherically focusing CRLs of larger diameters have been made with imprinting and bubble-in-capillary fabrication techniques [20, 25], but the focal lengths from these fabrication techniques were beyond 10 cm for 10s of keV x-rays, thus limiting the level of magnification in a benchtop setup.

Recently, a nano-printing process based on two-photon photopolymerization has been explored to produce a CRL for focusing collimated beams of 9.25 keV at a 10 cm focal length [30], which demonstrated the ability to produce a bright spot of illumination. However, there is no such lens yet for hard x-rays, particularly of shorter focal lengths for high-magnification microscopy.

With the above background of the current state of x-ray optics, this dissertation investigates the development of two types of optical elements suitable for hard x-ray imaging, namely compound refractive lenses for hard x-ray microscopy, and diffraction gratings for hard x-ray wavefront imaging.

Chapters 2 and 3 report the application of two-photon photopolymerization as a new approach to the development of high performance CRL elements for hard x-ray imaging. Using this approach, a 1.8 mm long polymer CRL with a focal length of 21.5 mm at 22 keV, and numerical

aperture (NA) of 2.79×10^{-4} are demonstrated. The resulting polymer CRL was successfully used in a benchtop microscope to image and evaluate the focal spots of tungsten anode x-ray tubes at 74x magnification.

Chapter 4 describes the development of large area nanoscale gratings for use in x-ray phase contrast imaging using a deep reactive-ion etching process. By optimizing the nanoscale process parameters, a trench depth of ~ 10 μm and maximum aspect ratio of 50 for grating period of 400 nm are reported.

In Chapter 5, future directions of development are explored following a summary of the contributions from the dissertation research.

Chapter 2. X-ray refractive lenses

2.1. Introduction

Focusing optics for hard x-rays have been a long-standing challenge in x-ray science. The refractive indices of most materials fall slightly below 1 in the hard x-ray regime, making vacuum appear optically ‘denser’. Due to the small refractive index decrements of all materials, there is not adequate refractive power to focus hard x-ray beams in conventional refractive lenses. Several designs, concepts, and fabrication process have been proposed to address this issue. Despite significant progress, hard x-ray focusing is still challenging in x-ray optics due to the limitation in fabrication and material structural stability.

In this chapter, we present a new design for a low-cost fabrication process using a two-photon laser photopolymerization system to pattern epoxy-based CRLs by direct 3D nanoprinting.

2.2. x-ray optics

X-ray focusing optics are essential for microscopy and analytical imaging applications, which motivated significant development for several decades. Currently several x-ray optics exists that can generate nano-beams and provide <10 μm resolution. However, complexity of fabrication and limitation of hard x-ray performance make it difficult to achieve an ideal form of focusing optical element. The desired optics may vary based on the given application. In the following section current hard x-ray focusing optics and their limitations will be briefly reviewed.

2.2.1. Kirkpatrick-Baez mirrors

One of the most commonly used x-ray focusing elements are Kirkpatrick-Baez mirrors (K-B mirror) in which a pair of perpendicular reflecting mirrors that are curved and have extremely polished surface are used to reflect the coming incidents and focus the x-ray beam (Figure 2). These mirrors are typically fabricated from near-atomic polished silicon crystals coated with atomic layer of metals such as platinum and will be curved using a fine bending force. The focal spot in KB mirrors is extremely sensitive to any distortion to the point where even a micrometer scale deflection in the mirror will cause more than 60 times dislocation in the focal spot position. Therefore it requires precise and advanced control in fabrication, alignment and stability. In addition, it has a long focal length and can only operate up to 10 KeV.

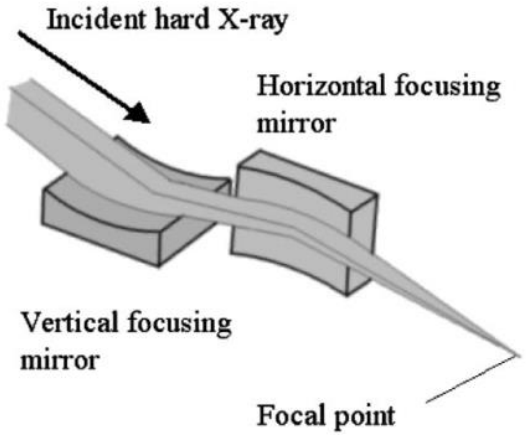

Figure 2*. Kirkpatrick-Baez mirror: a pair of perpendicular reflecting mirrors that are curved and have extremely polished surfaces are used to reflect and at the same time focus the incident x-ray beam to a spot*[31].

2.2.2. Fresnel x-ray zone plate

Another type of focusing optics is a Fresnel x-ray zone plate (FZP) that consists of many concentric circular zones with decreasing width (Figure 3). Either the transmission or the phase shift of an incident x-ray beam is alternatingly modulated by the zones, resulting in part of the beam being diffracted toward a focal point. The outermost zone width will determine the focal spot size while the zone thickness scales up with the beam energy. Therefore, ultra-high aspect ratio device is needed for operating at the hard x-ray regime to penetrate thicker samples. Despite the significant performance at the soft x-ray regime, no zone plate has been fabricated to operate at x-ray photon energy more than 8 KeV owing to the limitation in fabricating the diffractive zones with ultra-high aspect ratio.

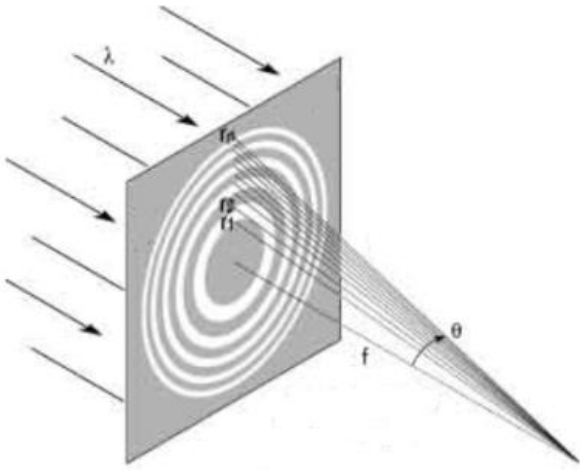

Figure 3. *Fresnel x-ray zone plate (FZP) that consists of many concentric circular zones with decreasing width. Alternating transparency or phase shift across the zones diffracts part of the incident beam toward a focal point*[32].

2.2.3. Compact refractive lens

In 1996, Snigirev introduced compound reflective lenses (CRL) (*Figure 4*) to address this issue[12]. Compound lenses contained series of tens or hundreds of individual voids in a material, to accumulate their small refractions. The problem regarding the high absorption in the material is addressed by using materials composed exclusively of low atomic number elements, such as polymers. They possess about 1000:1 ratio of phase shift over wave amplitude attenuation. Current available CRLs have long focal length and could not focus beam in hard x-ray regime due to the limitation in fabricating small aperture lens. However, compactness, high thermal stability, feasible alignments and minimized absorption make them very popular among x-ray focusing optics.

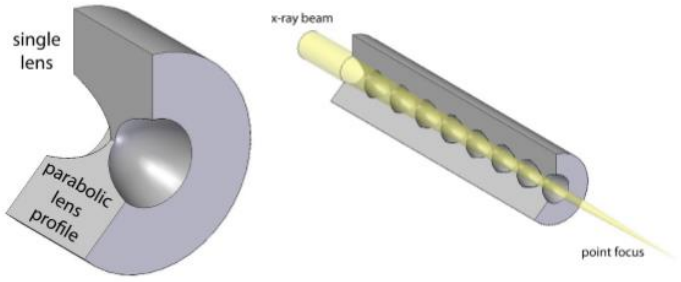

Figure 4*. Compound refractive lenses (CRL)*[33] *contained series of individual voids in a material, to accumulate their small refractions.*

A comparison between three focusing elements is shown in (table. 1) where the advantage and disadvantages of each element is listed.

Table 1. *Comparison between three focusing elements*

Optical device	Advantage	Disadvantage	Upper limit of photon keV
Curved Mirrors	High efficiency, achromatic	Long focal length, difficult to fabricate, alignment stability	10's
Zone plates	Compact	Lower efficiency, limited to soft x-rays due to fabrication limitations	8
Compact refractive lenses	Efficient	Challenging fabrication, long total length of the lens	9.25

In this chapter, the x-ray optics involved in the CRL performance is studied and a novel fabrication process is proposed to address the issues with the current available CRLs.

2.3. X-ray optics of the parabolic cylindrical CRL

Interaction of x-ray waves with a uniform material follows the general principle of electromagnetic waves. It include elastic (coherent) scattering that contributes to the refraction or diffraction of the wave, and inelastic (incoherent) scattering and absorption that contribute to a loss of the coherent amplitude of the wave[34]. These processes are summarized in the refractive index of the material as

$$n = 1 - \delta + i\beta \quad (1)$$

Where δ is the refractive index decrement that represents an increase of the wavelength in material. It has a small and positive value of about 10^{-6} for hard x-rays. The imaginary part β represents the attenuation of the coherent wave amplitude due to the inelastic scattering and photoelectric absorption processes. In low atomic number elements such as H, C, O, P, the ratio of δ/β is approximately 1000:1 for photon energies above 10 keV, although both values generally increase with the atomic number. Therefore, low atomic number elements make good phase shifting materials, but require more path lengths through the material than high atomic number elements. In practical terms, it means that polymer lenses lose less x-rays than metal of silicon lenses, but are longer.

The focusing lens for visible light is convex. For most materials the x-ray refraction index is slightly less than one, therefore the focusing lens should be concave.

2.3.1. Focal length

For a lens with spherical surfaces, the focal length using the lens maker's formula is written as[35]:

$$\frac{1}{f} = (n_1 - n_2)\left(\frac{1}{R_1} - \frac{1}{R_2}\right) \quad (2)$$

Where f is the focal length, n_1 is the lens material refractive index, n_2 is the surrounding environment refractive index and R_1 and R_2 are the radii of curvature on the two sides of the lens. Since the lens is concave and the experiment is being considered to be done in vacuum in ideal form, $n_2=1$ and $R_1=R_2=R$. Therefore, eq. 5 can be written as:

$$\frac{1}{f} = \frac{2(n_1 - 1)}{R} \quad (3)$$

Using $n = 1-\delta$ is the eq. 6, focal length is given by:

$$f = \frac{R}{2\delta} \tag{4}$$

Since δ is very small (10^{-6}), In order to get the short focal length, curvature radius needs to be small. To get the focal length within the mm scale, the curvature radius has to be within the few micron range. Meanwhile, with having the whole length of N stack of the parabolic lenses short enough in comparison to the focal length; its focal length is equal to value of the whole focal lengths added together:

$$\frac{1}{f} = \sum_i \frac{1}{f_i} = \frac{R}{2N\delta} \tag{5}$$

2.3.2. Lens shape

The ideal surface profile of an x-ray lens is not spherical. In order to focus a beam to a spot, the exit wavefront should have a spherical profile (Figure 5). To obtain that profile, the beam passing through the polymer and air should have accumulated different phases. Due to fact that the refractive index of the x-ray is less than one, the wavefront is phase shifted forward inside the polymer. The profile of the lens should produce a spherically shaped wavefront. Referring to Figure 5, the forward shift of the wave front at cylindrical radius R should be

$$\Delta = \sqrt{R^2 + f^2} - f = f\left(1 + \frac{1}{2}\frac{R^2}{f^2}\right) - f = \frac{R^2}{2f} \tag{6}$$

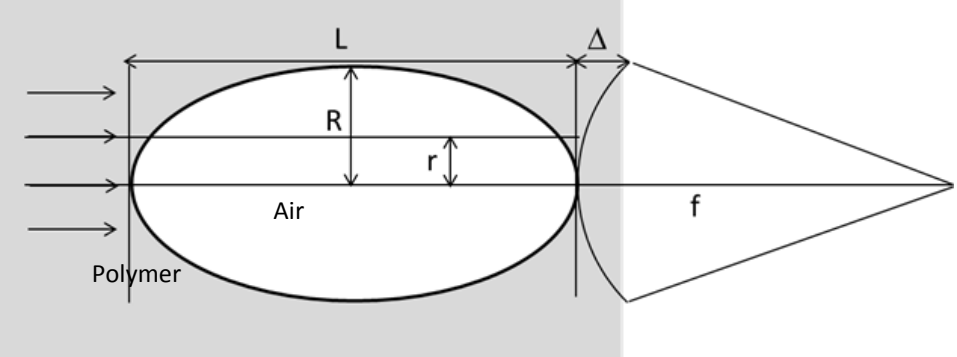

Figure 5. *Refraction of a beam passing through a parabolic lens*

The refractive index of the lens is n=1- δ, hence the maximum length necessary for Δ is given by:

$$\delta * L = \frac{R^2}{2f} \tag{7}$$

Similarly, for the rest of the structure, the beam equation can be written as:

$$L(r) = \frac{r^2}{2f\,\delta} \tag{8}$$

Which is a parabolic equation. For that reason, in order to produce the spherical wave, a parabolic lens is needed. Therefore, for a CRL made of a series of concave lenses each having a parabolic surface, the focal length is:

$$f = \frac{R^2}{2Nl\delta} \tag{9}$$

Where l is the length of an individual parabolic surface.

The number of individual lenses defines the total length of the CRL. The focal length decreases when the number of lenses, N, increases. Also, the deeper lenses will provide more refraction, therefore shorter focal length. However, the field of view (FOV) of the CRL for high magnification microscopy is estimated to be *2R*f/L*. There is an inverse relationship between

FOV and the total length of each CRL, which produce a tradeoff between the FOV and the focusing effect of the CRL.

2.3.3. Aperture

The physical aperture (D_{eff}) is the opening where the light passes in an optical system. In the polymer lenses it is the diameter of the lens, 2R.

2.3.3. Numerical Aperture

Numerical Aperture (N.A.) or the angle of light is a dimensionless parameter that defines the number of beams that will be collected at the detector. The larger the N.A. will lead to a better resolving power of a lens. It's in a direct relation with the effective aperture and can be written as:

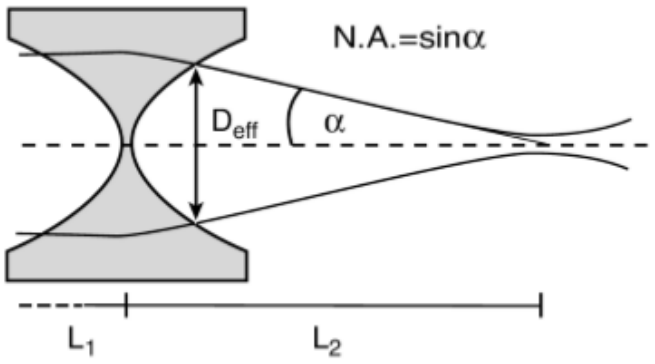

Figure 6. *The numerical aperture of a lens is defined by N.A.= sinα*[33]

$$\text{N.A.} = \sin\alpha \approx \frac{D_{eff}}{2L_2} \quad (10)$$

2.3.5. Focal Spot Size and Resolution

The focal spot size is defined by the geometry of the lens. The lateral sizes of the beam dominants the resolution of the microscope in the vertical direction and the transverse size defines the resolution in horizontal direction. The overall spot size of the beam can be written as:

$$B_t = \sqrt{B_v + B_h} = \sqrt{m^2 {d_A}^2 + (0.75.\frac{\lambda}{2N.A.})^2} \quad (11)$$

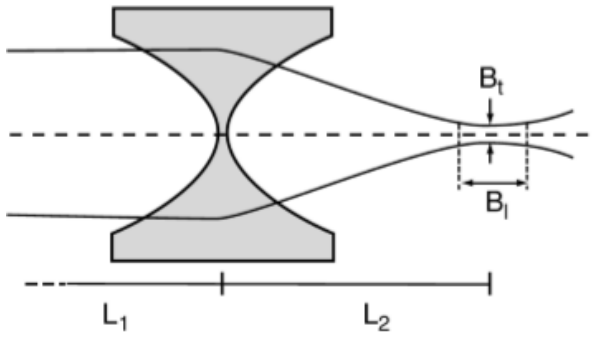

Figure 7. *Illustration of the focal spot size of a concave lens*[33]

Where m is the de-magnification ($\frac{L_2}{L_1}$) and d_A is the entrance aperture width.

2.3. Compound Refractive Lens Fabrication

Microfabrication of compound refractive lenses has been a challenging task. Different types of parabolic CRL have been investigated and various materials composed of low atomic number elements and several fabrication techniques were explored to achieve the minimum focal length along with the least absorption and best performance. Some were limited to the cylindrical shape and others were not able to reduce the focal length below 10 cm for hard x-rays. In the following section current CRL's fabrication and manufacture techniques and their limitations will be briefly reviewed.

2.3.1. Prior Fabrication Techniques of CRL

Various techniques have been reported in the literature for the fabrication of CRL optics. In one simple approach, a computer controlled drilling machine was used to form cylindrical holes in a Al-Cu alloy block[12]. Since Aluminum exhibits a high level of absorption with an atomic number of Z=13, low Z materials have also used to improve the energy range of CRL lenses[22,36]. For

example, Beryllium (Z=4) biconcave lenses were fabricated using pressing or debossing techniques, where a pressing tool with two convex paraboloids was employed to tightly press the Beryllium simultaneously on both sides However, Beryllium is not favorable due to its toxicity, grain distortion of the polycrystalline structure, and limited availability of single crystal material. The parabolic radius of Be lenses is currently limited to several hundred microns, resulting in a large focal length above 1 m[37,38,39].

An alternative approach to CRL fabrication is based on the controlled formation micro-bubbles in an epoxy matrix[20], This technique is based on filling a number of biconcave microlenses in a glass microcapillary. It utilizes the fact that a drop of liquid in a capillary tube forms a biconcave shape due to the surface tension forces. The lens material was selected as epoxy and spherical air bubbles are injected to it. The bubble radius is equal to the capillary radius, and the epoxy material between two bubbles is the biconcave lens. This fabrication method is limited to the capillary radius and the focal length is about 10 cm for soft 8 keV x-rays. Moreover, because of the inherent shape of the bubbles is spherical rather than the desired parabolic shape, this adds to the optical aberration of the CRL.

Conventional microfabrication methods have also been employed for CRL patterning. Lenses fabricated from Si (Z=14) have been patterned by DRIE, while diamond (Z=3) CRLs have been patterned by laser microimachining[26,4028]. The resulting Si based lenses have shown relatively high absorption and are able to achieve focal lengths down to 1 m on bench top systems. While Diamond shows advantages over Si with high endurance and low x-ray absorption, it ultimately cannot compete with Si because of the limitations in fabrication.[26] Making compound refractive lenses using deep x-ray lithography to pattern polymers is another technique that has been able to produce the lowest reported focal length[41]. The difference between this technique and the

conventional photolithography is that x-ray lithography can transfer the mask pattern to a thick layer of polymer or resist (400 μm SU-8)[42]. However, the patterns are still cylindrical and the focal length is more than 10 cm. Furthermore, an inherent limitation of these conventional microfabrication techniques is that because they are cylindrical processes, they are applicable only to relatively simple optics such as cylindrical lenses, which doubles the number of lenses needed for microscopy applications.

Current limitations in fabrication of CRLs with cylindrical and bubble shaped 3D structures are limiting the focal length and minimum resolution achieved by the available devices. A novel and low cost fabrication process using a two-photon laser photopolymerization system is proposed to pattern CRLs by direct 3D nanoprinting.

2.3.2 Fabrication of CRL with Nanoscribe 3D printing

In this work, a two-photon laser photopolymerization process is explored to pattern epoxy-based CRLs by direct 3D nanoprinting as a novel and highly promising technique for lens fabrication. Unlike existing fabrication methods that use mold or air bubbles to fabricate the lenses, any desired shape is printable in this technique. The developed process has been shown to enable the formation of micron-scale CRL arrays with 19 mm focal length, 82x magnification and better than 2.4 μm resolution.

2.3.2.1.Two-photon Polymerization[43]

The general principle of the two-photon polymerization is that a molecule absorbs two photons simultaneously, where the first photon boosts the molecule into a virtual state for a short duration to allow it to absorb a second photon to reach the final state, with an energy increment that is twice that of a single photon. This process is driven by a focused femtosecond laser. Specifically,

polymerization occurs when the weakly cross-linked polymers break by the absorption of the photons and generate two radicals, which will react with monomers. Radicalized monomers will react with each other and create three dimensional highly cross-linked polymers. The polymerization is localized at the laser focal point. The focal point is scanned in 3D space to write the designed structure. The unpolymerized part is then removed by solvent after laser exposure. The process enables high-resolution patterning below the diffraction limit of the laser beam [43].

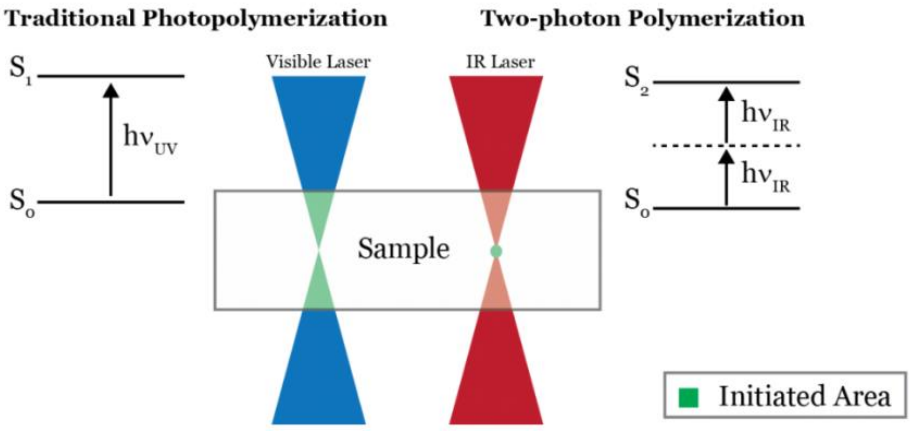

Figure 8. *Photon energy absorption in traditional and two-photon polymerization. A molecule that absorbs a single photon in the visible light range can also absorb two infrared photons of half the energy in quick succession. Source: http://www.tuckerlaboratory.org/Tissue%20Engineering*

In stereolithography a UV laser can only reach the surface of the photosensitive material. Photosensitive materials are transparent to infrared and let the light pass through their surface, thus in order to write within the volume of the material, infrared light is used[44,45]. Writing in polymers is done in there are three different configurations; Oil immersion, Dip-in laser lithography, and Air configuration.

In Oil Immersion configuration, exposure occurs through the substrate to focus the laser beam into the photoresist. The immersion oil matches the refractive indexes of the microscope

objective and the substrate and provides the ideal focus point at the interface of substrate and photoresist. However, the spherical aberration occurs when the height of the structure increases and focus point gets deeper.

The configuration where the exposure occurs though the photoresist is called Dip-in laser lithography (DiLL) in which the spherical aberrations are minimum and the height limit for structure can be larger than 2 mm. Fused silica with two different thicknesses is used as a substrate for this configuration and the Dip-In resist's refractive index is 1.52. In order to match the index of the resist and the thin substrate, a thin layer of metal such as gold or Al_2O_3 is needed.

Similar to oil immersion, the laser beam in Air configuration is focused through the substrate. However, the immersion medium is air instead of oil. The height limitation is also an issue in this configuration and is defined by working distance of the microscope objective.

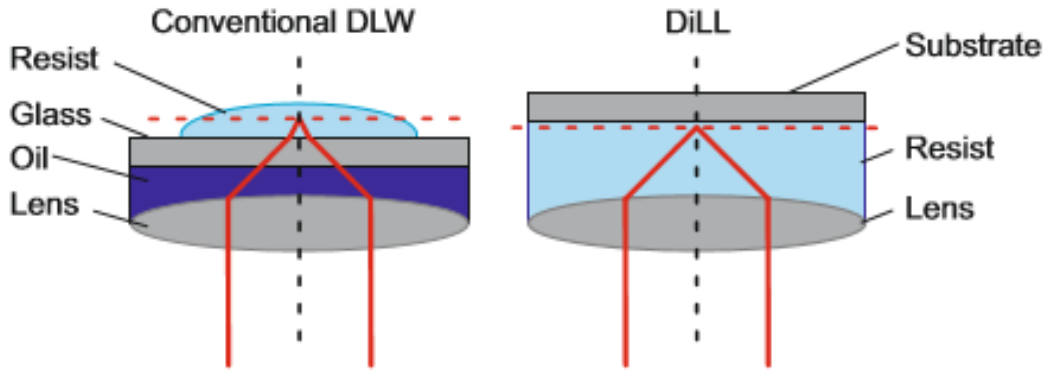

Figure 9. *Oil immersion writing configuration vs Dip-in laser lithography. Source: Nanoscribe manual.*

2.4. Detail of 3D Nanoprinting of CRL

2.4.1 Characterization of the fabrication process

The CRL was fabricated with the Nanoscribe 3D printer (Nanoscribe Photonic Professional (GT)) (Figure 10).

Figure 10. *Nanoscribe Photonic Professional (GT). Source: Nanoscribe manual*

Before writing the lens patterns, four sets of conditions were designed to study the effect of laser power and the writing resolution. A sample pattern with connected pillars was used to investigate these parameters. The low resolution was set to 200 nm and maximum resolution was 400 nm. The minimum power was 15 mW and maximum power was 27.5 mW. Due to the height of the lens, the pattern was written in the DLL mode. The first set of experiments showed that the highest power and lowest resolution works fine for this specific pattern. Further experiments depicted that any power above 27.5 mW is enough to get the proper cross-linked polymer (Figure 11).

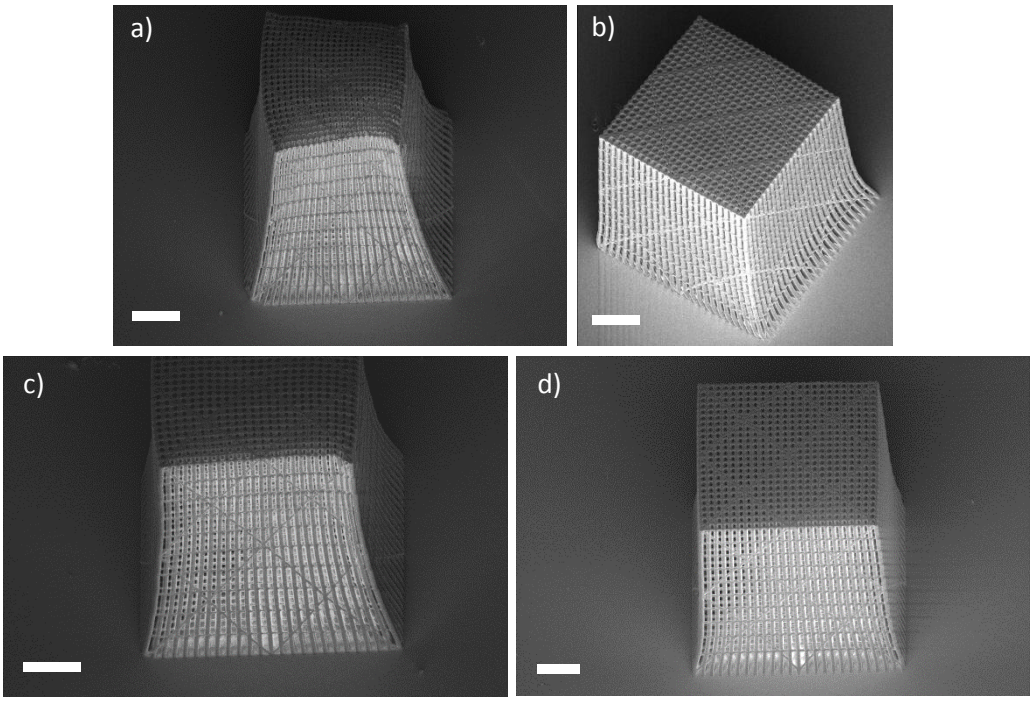

Figure 11. *Charactriczation of the laser power and writing resolution on a sample pattern. a) Low power, low resolution b) Low power, high resolution c) High power, low resolution d) High power, high resolution. All scale bars are 25 μm.*

2.4.2. Cylindrical CRL fabrication

As a first step, a 12 μm aperture cylindrical CRL (Figure 12) was fabricated using a dip-in laser lithography (DiLL) configuration (Figure 13). This technique allows for two-photon polymerization with constant optical aberrations and provides variety of printing options for any desired pattern. In this mode, a droplet of IP-DIP resist was drop-casted on the center of a 700 μm thick, 25 mm square fused silica substrate. The CRL elements were patterned in the resist via layer-by-layer scanning of the laser focal spot at 400 nm resolution. The substrate was then immersed in a propylene glycol methyl ether acetate developer for 15 min, followed by a 15 min bake at 70°C. Other processing conditions such as laser power, layer thickness and hatching

distance were also crucial in making a robust structure without distortion. After characterizing the process with a number of trials, we found that a suitable lens structure could be achieved using a hatching distance and layer thickness of 400 nm and a laser power level of 30 mW, which was 60% of the maximum power of 50 mW. The resulting nano x-ray microscope consists of a 400 μm tall structure containing 3 arrays of elliptic cylindrical lenses.

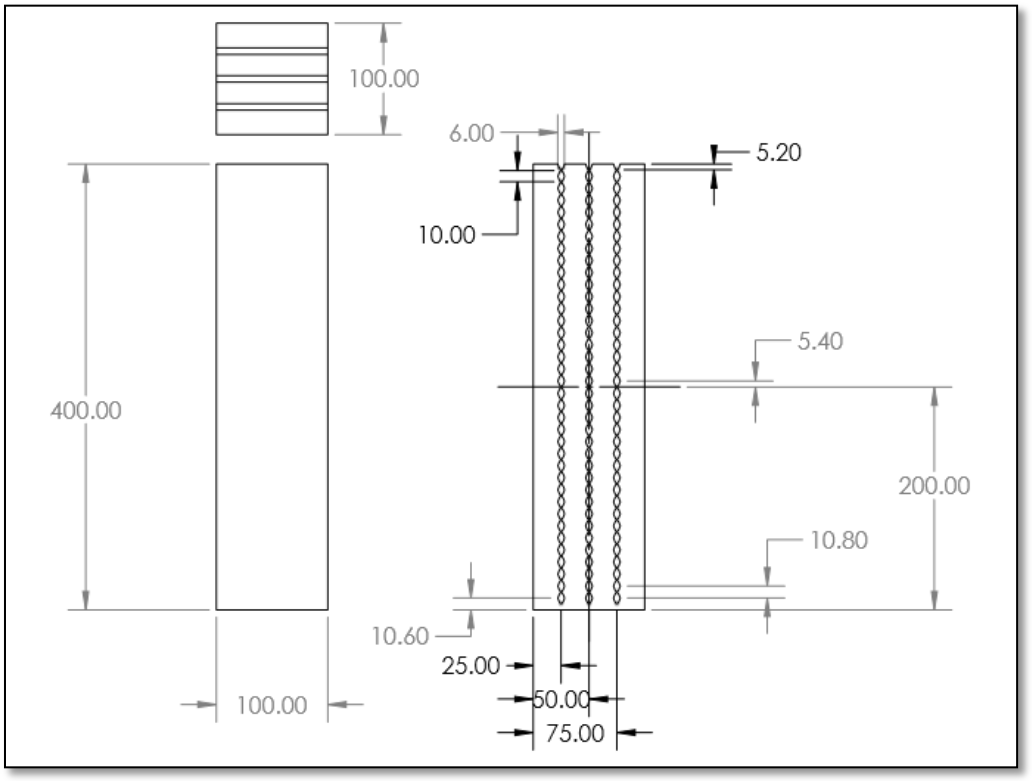

Figure 12. *Detailed dimensions of cylindrical lens arrays in a vertical polymer block. All dimensions are in μm.*

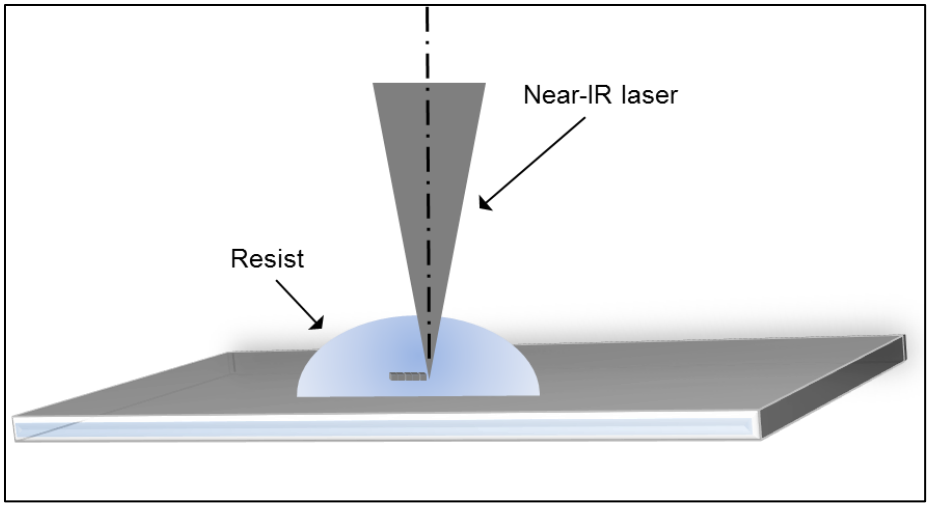

Figure 13. *Illustration of writing the CRL pattern in the polymer resist using the Dip-In Laser Lithography (DiLL) mode of Nanoscribe.*

The cylindrical lens structure consisted of three columns of cylindrical ducts spaced 25 μm apart. Each column included 36.5 horizontal ducts stacked vertically. Cross-section of each duct is 6 μ m wide and 10 μm deep. Vertical spacing between adjacent ducts is 0.8 μm; the one half duct is at the very top and open to the outside for SEM (Figure 14). Due to the fact that the pattern height exceeded the capacity of the piezo range (300 μm), pattern splitting was needed to write up to a height of 400 μm, while the z-drive movement was used to move the objective's position. The structure was split into two blocks to form the structure; and two 300 μm and 100 μm block were assembled by stitching process. Piezo movement updated each layers position and when a level was complete, the z-drive position moved to the beginning of the new block.

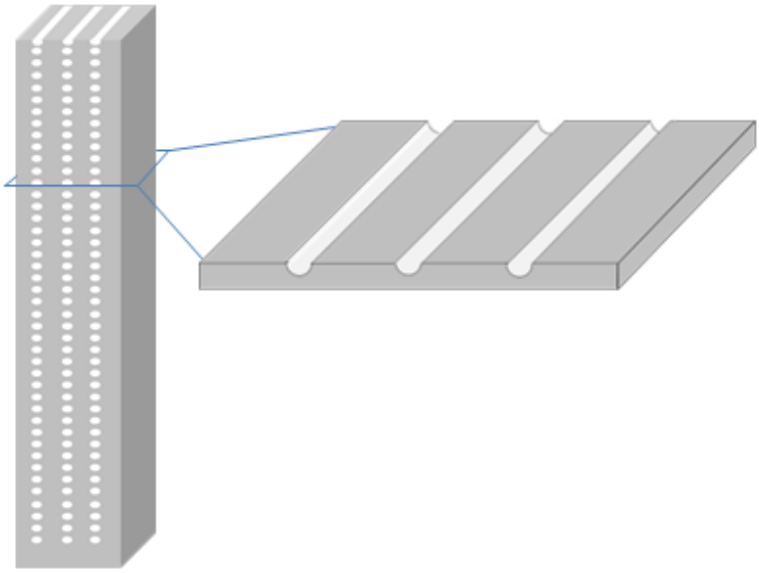

Figure 14. *Schematic of the vertical column of cylindrical CRL.*

The CRL structure was inspected with scanning electron microscopy (SEM) (Figure 15). The size of individual ducts and the curvature of the edge and height were verified. The SEM images were used to eliminate any visible defects on the outer surface of the blocks.

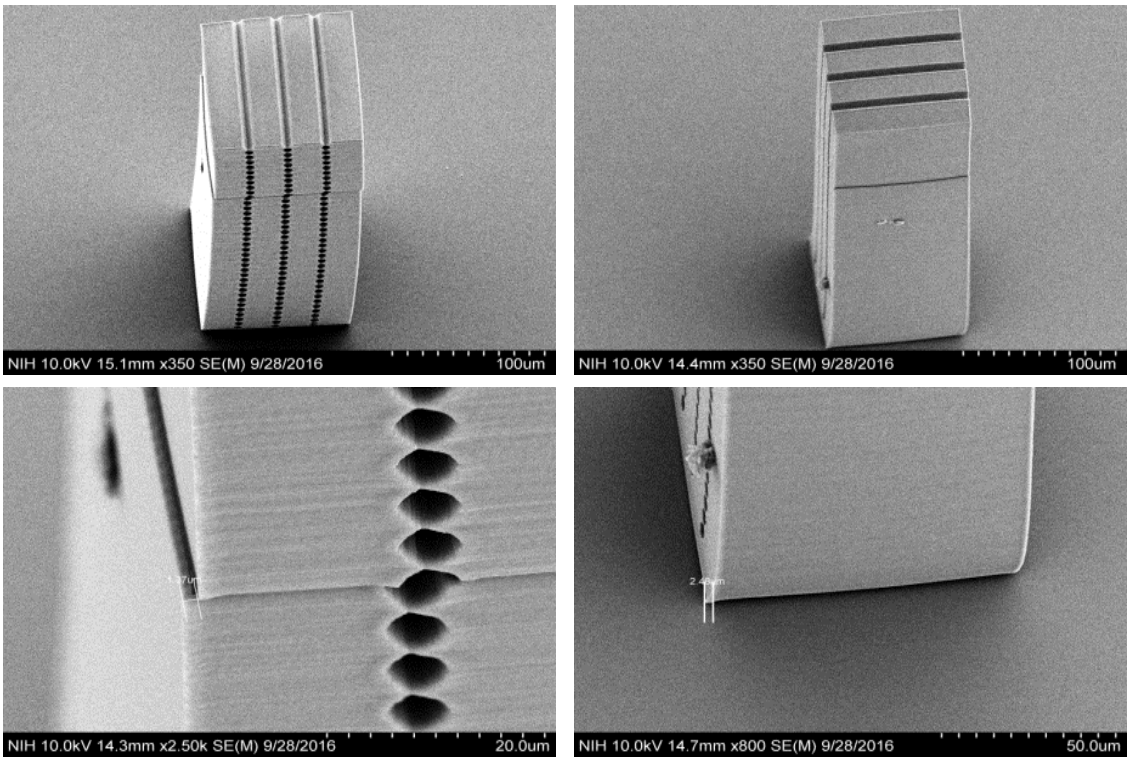

Figure 15. *Scanning electron microscopy images of a block of 400 μm height containing 3 cylindrical CRLs*

2.5. Radiographic inspection

A micro-computed tomography (microCT) scanner is used to analyze the energy of the incident radiation and focusing ability of the lens. Skyscan microCT has an 11 Mp X-ray camera (12-bit cooled CCD fiber-optically coupled to scintillator) with a micropositioning stage, an array size of 4000x2000 pixels at the lowest binning, and a 5 mm source spot size with 20-100 kV source voltage and 10 W source power. Unlike conventional clinical CT scans, where the source and detector move around the patient, in the Skyscan the sample stage rotates around a fixed camera and detector.

The sample was mounted on a custom aluminum holder and placed on top of a micropositioner stage that is connected to the main rotational sample stage (Figure 16). Once the live view was active, the lens was aligned by focusing at ascending magnifications and progressively centering the lens, until the target sub-micron resolution was reached. Once at the target resolution, a Ry scan was performed to determine the best focusing effect for the specific lens. The ideal focusing effect expected was 3 symmetrical bright peaks that rise above the average intensity (baseline intensity) outside of the lens (Figure 17). The alignment of the lens was quantified by the difference between the intensity of the peaks and the baseline outside of the lens.

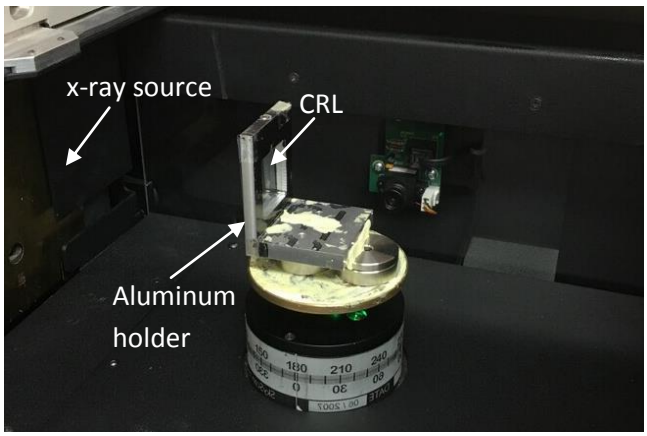

Figure 16. *CRL mounted on a custom aluminum holder in the microCT system for inspection.*

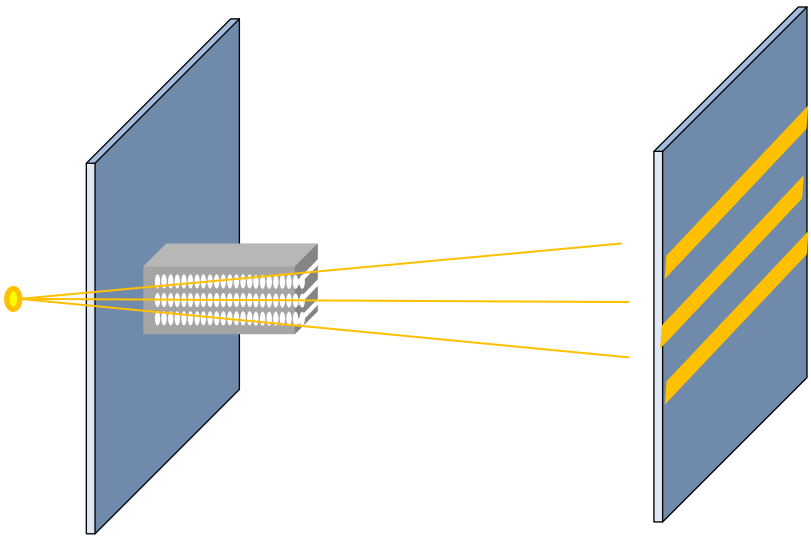

Figure 17. *The focusing effect of the three cylindrical CRLs produce three lines that are brighter than the background average intensity.*

The focusing effect detected in the first round of experiment is shown in (Figure 18). Where the intensity of the cylindrical lenses rise about 15% more than the area outside the lens. The lens image shows that the block's deformation is affecting the focusing elements of the CRL. In the next section the fabrication defects in the lens will be explored.

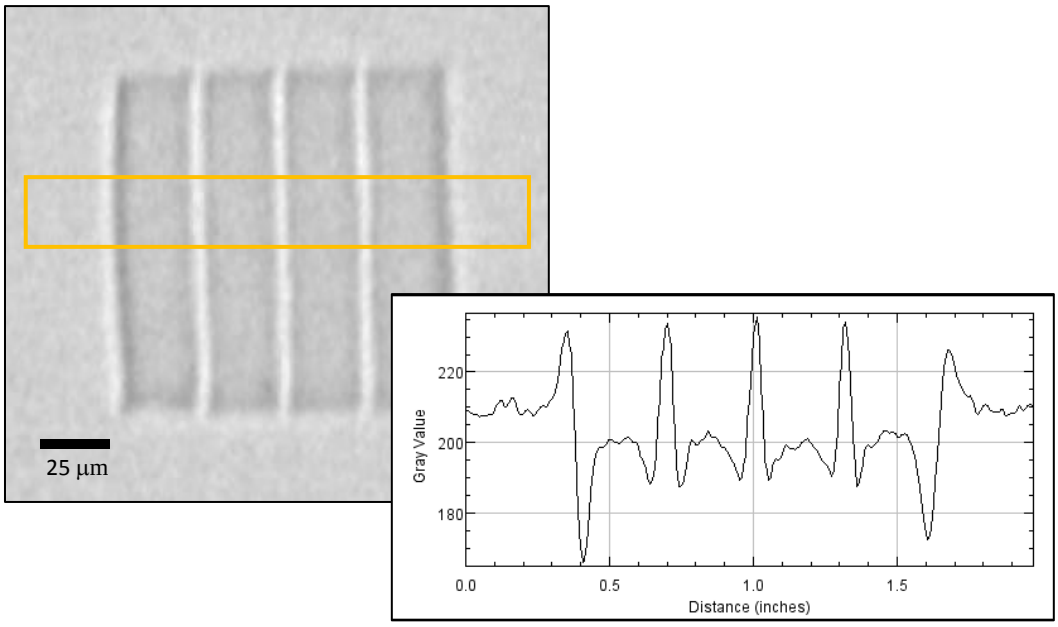

Figure 18. *Focusing effect of the cylindrical CRLs and the intensity profile across the focused lines in the highlighted box.*

2.6. Issues Encountered in Fabrication

2.6.1. Curvature along the height of the vertical column

One of the issues with the fabricated micro lens was the curvature along the height of the structure. However, since the curvature is in a direction that the lenses are still parallel, this will only cause losing some part of the field of view. Splitting the pattern into two 200 μm tall blocks (Figure 19) resulted some improvement in the curvature of the lens pillars; however, the optical results were not significantly different.

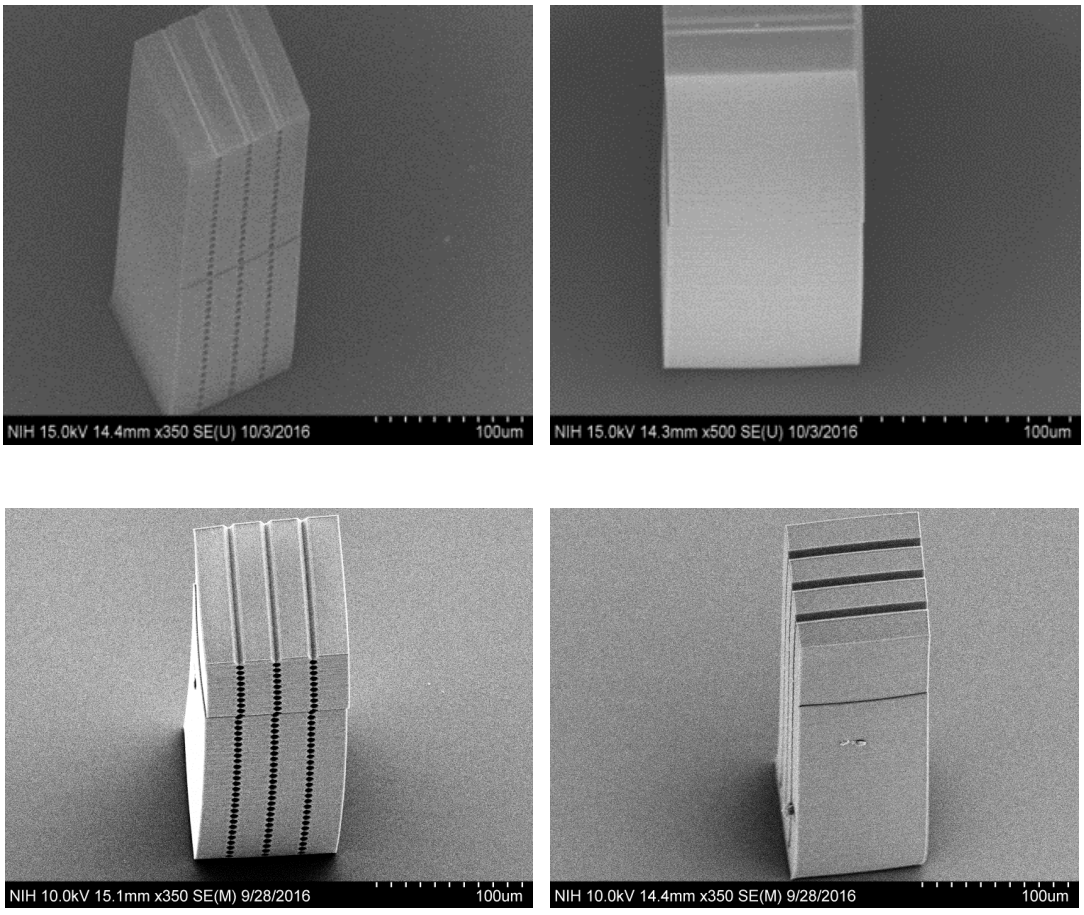

Figure 19. *Curvature along the height of the structure is less with 200-200 μm split point (top two figures) than 300-100 μm split point (bottom two figures).*

2.6.2. Thick versus thin substrate

In order to write in DiLL configuration, there were two options for the substrate; thick substrate (700 μm) and thin substrate (170 μm). For the 170 μm thick cover slip 100 nm Au layer is used to increase the refractive index difference between the substrate and the resist. Since the 700 μm thick substrate would add extra absorption to the x-ray imaging setup, gold coated thin substrate was used to reduce that absorption.

Having a conductive layer at the substrate, the bottom side of the structure faced over heating due to the laser power reflection from the substrate. (Figure 20)

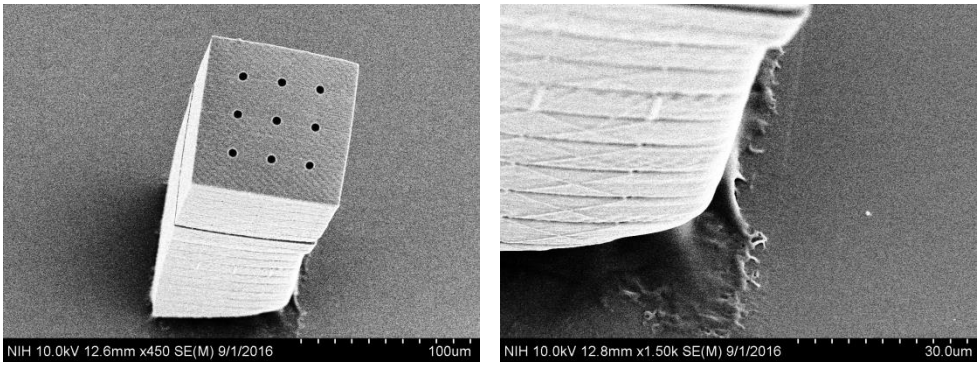

Figure 20. *Heating and detachment of the bottom portion of the structure due to reflection of the laser beam by the Au layer.*

To address this issue, separate sets of power were applied while writing along the height of the structure. For the first 10 μm, power of 30% of the maximum power of 50 mW and for the rest of the height, 50% power was used (Figure 21). The results illustrated that despite the fact that the 15 mW power did not provide enough intensity to break the cross-linked polymers in non-Au

structures; the area adjacent to the metal surface faced more power than 15 mW and had a stable profile.

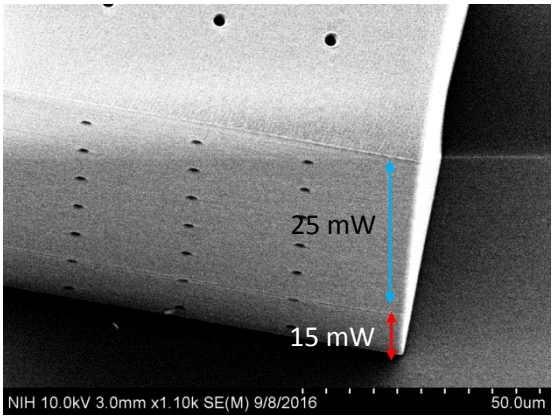

Figure 21. *Effect of splitting power while writing the structure on the metal coated substrate*

2.6.3. Vertical stitching error

As mentioned before, due to the limitation of the Nanoscribe tool, stitching was needed to fabricate a structure with height of 400 μm. During the stitching process, the laser beam deviates from the programmed position. This deviation is called distortion and can cause a misalignment at the beginning of the new block (Figure 22). Distortion along with the lateral displacement error of the stage, are two major reasons for the stitching error. In our experiment, the measured stitching error was about 1 μm in different structures with different split point and applied power.

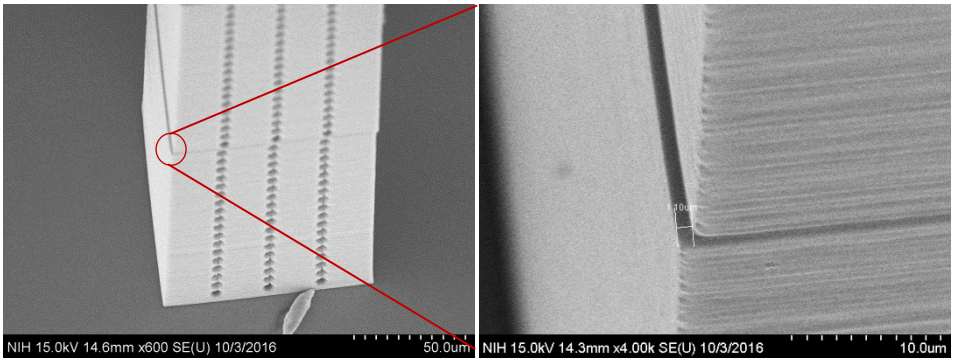

Figure 22. *Misalignment between the vertically stacked blocks due to the stitching error.*

2.7. Designed of a horizontal CRL

Even with minimizing the height curvature, stitching error and the substrate thickness, current structures has a limited height and undesired absorption through the substrate. To address these limitations, a new horizontal design is proposed in which a 16 blocks of cylindrical lens are placed end to end with 5 μm gap. The 5 μm gap between adjacent blocks in the array were added to eliminate the shadowing effect of the laser beam that occurred when writing separate blocks next to each other. The total field of view of CRL will decrease by 18 μm.

Each block consists of three columns of cylindrical duct and each column contains five cylindrical duct stacks horizontally. Cross-section of each duct is 6 μm wide and 9 μm deep (Figure 23). The x-rays pass through the lenses in parallel with the substrate. This design simply eliminates the limitation of the height and stitching error and no absorption will occur due to the substrate thickness (Figure 24).

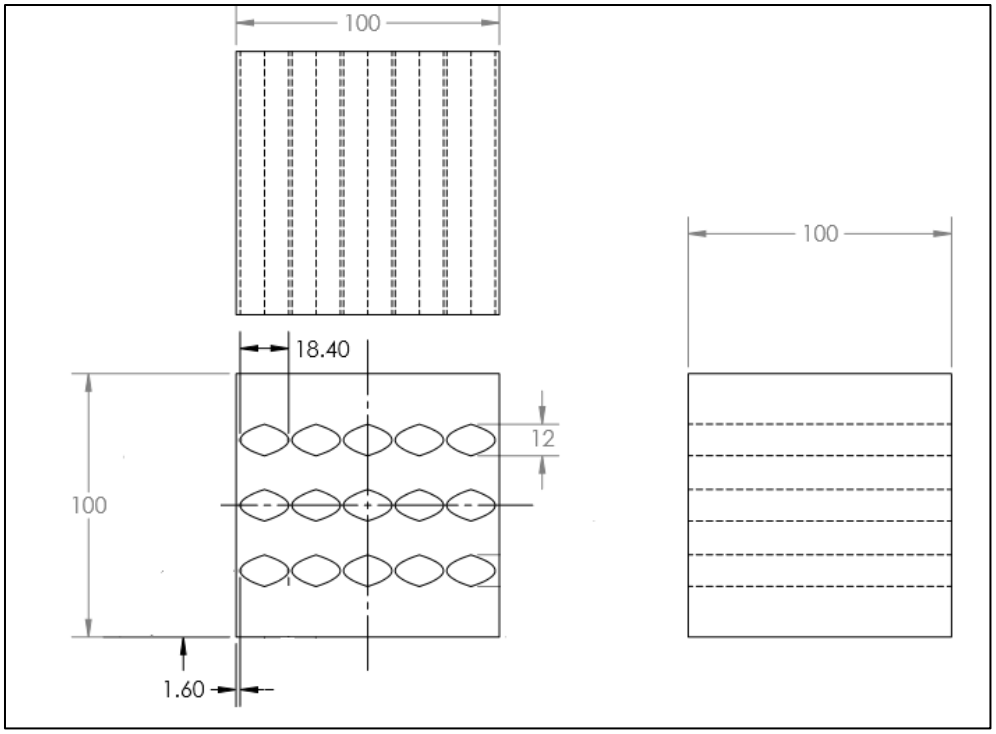

Figure 23. *Detailed dimensions of a polymer block containing three horizontal cylindrical CRLs. All dimensions are in µm.*

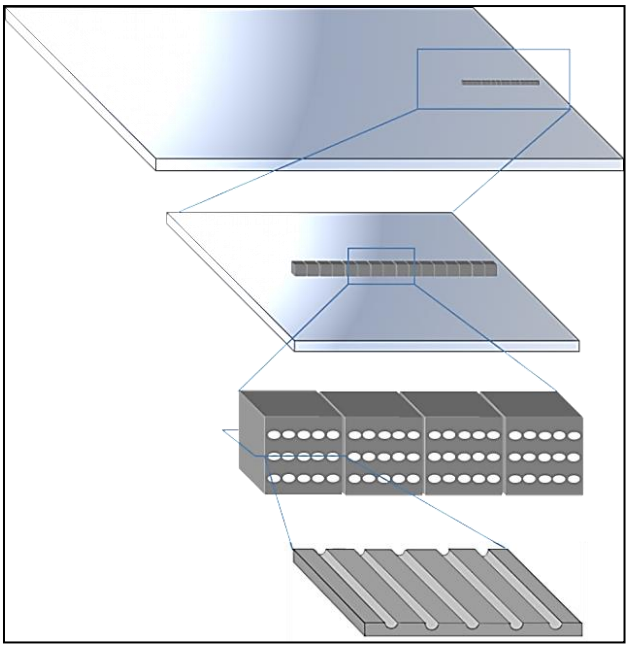

Figure 24. *Schematic of the horizontal cylindrical CRLs.*

DiLL mode configuration of the Nanoscribe was used to print the CRL. A hatching distance and layer thickness of 400 nm and a laser power level of 30 mW was was used in fabrication process to write the structures. The CRL structure was inspected with SEM (Figure 25).

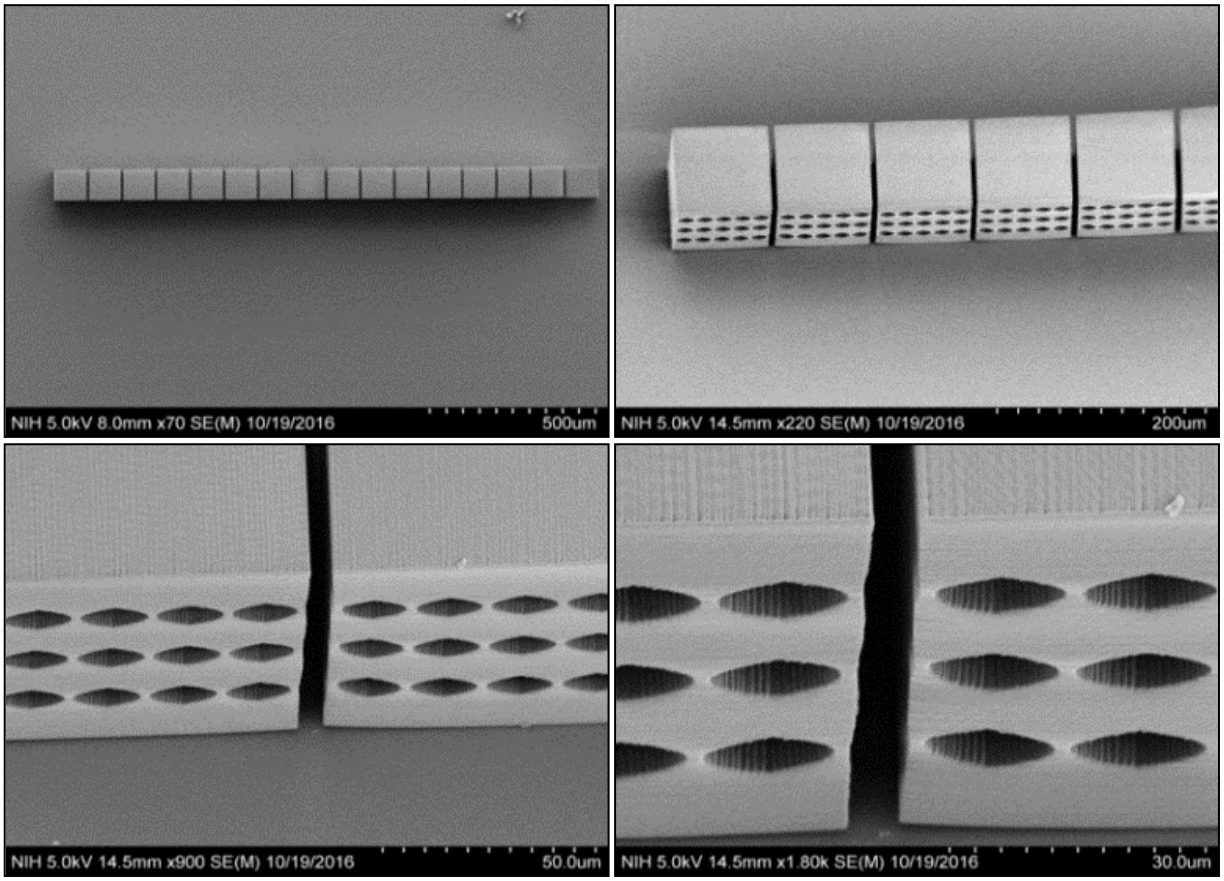

Figure 25. *Scanning electron microscopy images of the horizontal cylindrical CRLs.*

2.8. Radiographic inspection

Figure 26 shows the focusing effect of the horizontal CRLs in Skyscan set up. The source power is operating at 60 keV, 167 μA, and 10 W. It's demonstrating that the intensity of the x-ray beam improved while passing through the lenses due to a better focusing effect that is a result of increasing the number of lenses along with the elimination of the substrate's attenuation. The focusing effect is presented in (Figure 26) with the variance in the intensity of the light. The

maximum intensity is 250 (A.U.) and shows 67 % improvement in focusing effect. There is an intensity jump on the polymer side, which can be because of the edge diffraction of the lenses. However this feature was not detected in the Oxford scan set up. (Will be discussed in section 3.9.)

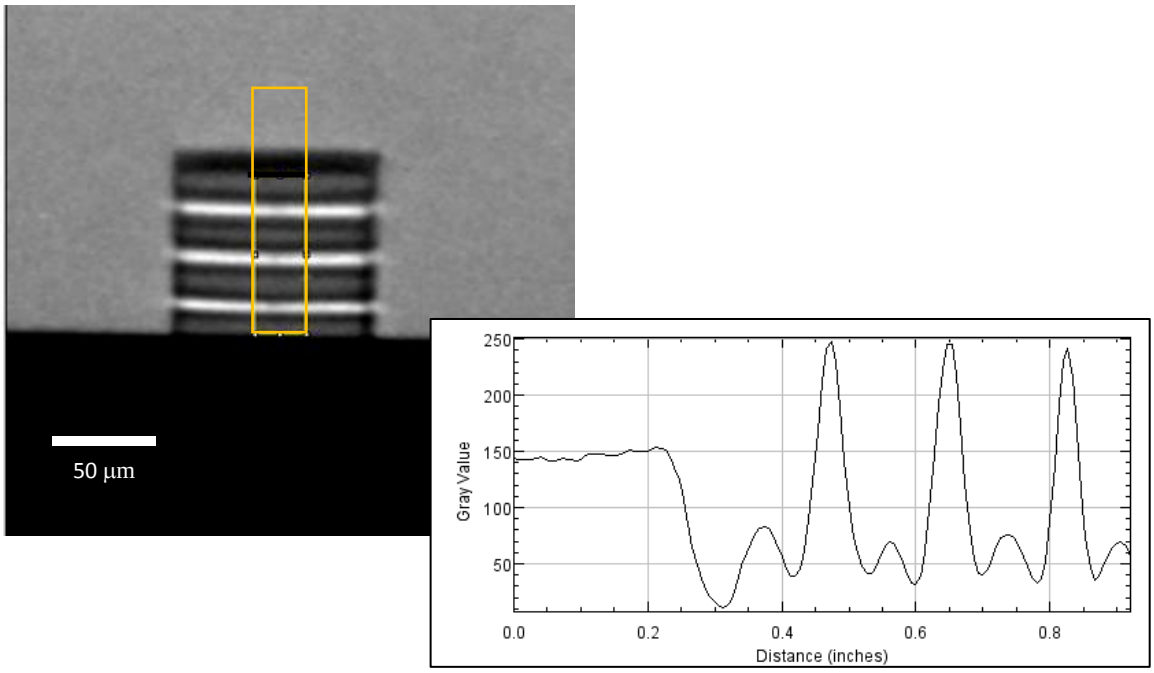

Figure 26. *Focusing effect in the horizontal cylindrical CRLs and the vertical intensity profile across the focused lines in the highlighted box.*

2.8.1. X-ray transmission through the CRL

One of the important parameters of a CRL is the transmission through the lens material. At an x-ray tube voltage of 60 kV and with a 25 µm Rh filter, the transmission through the solid polymer area outside the lenses was a = 85.6%. The transmission through the lens is given by (a-1)/ln(a), which is 92.6%.

2.9. Microscopic imaging test

We used an experimental x-ray microscopy set up as illustrated in Figure 27, using the nano printed x-ray CRLs as the magnifying lens. The imaged sample was a 3.8 µm period gold grating (Microworks, GmbH, Karlsruhe, Germany). The x-ray source is a fixed-anode, tungsten-target micro focus tube operating at 30 kV/10 W (Oxford UltraBright 96004, Oxford Instruments, Oxfordshire, United Kingdom), with an average focal spot size of 13.37 ± 0.35 µm (Figure 28). An indirect flat panel radiography detector with a pixel size of 83 µm (PaxScan 3024M, Varian, CA, USA) was used to image the grating. The geometric distances were L_1 = 10 mm from the source to the sample, $L_2 - L_1$= 20 mm from the sample to the lens, and $L_3 - L_2$ = 1640 mm from the lens to the detector.

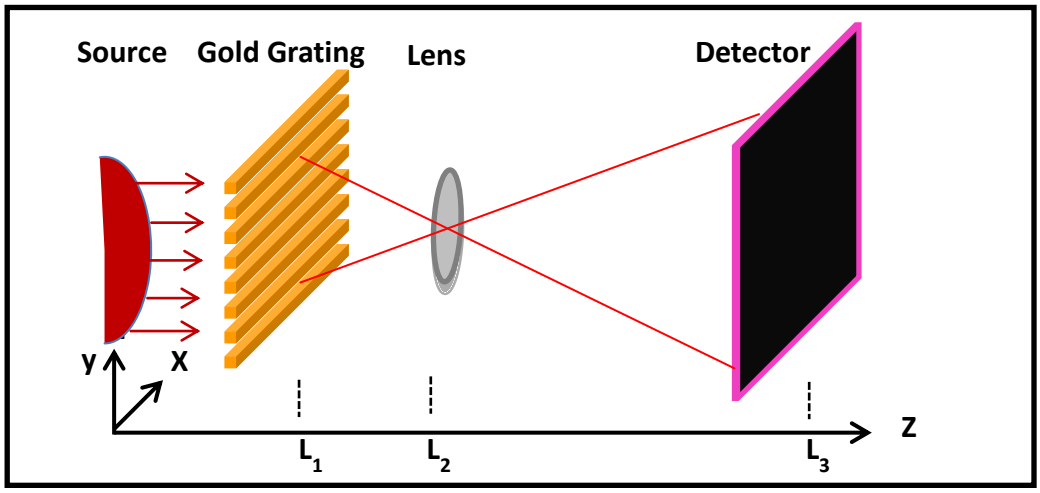

Figure 27. *A transmission grating of 4.8 µm pitch and consisting of gold lines is illuminated by an x-ray tube source. The transmission image is magnified in the vertical direction by a cylindrical CRL.*

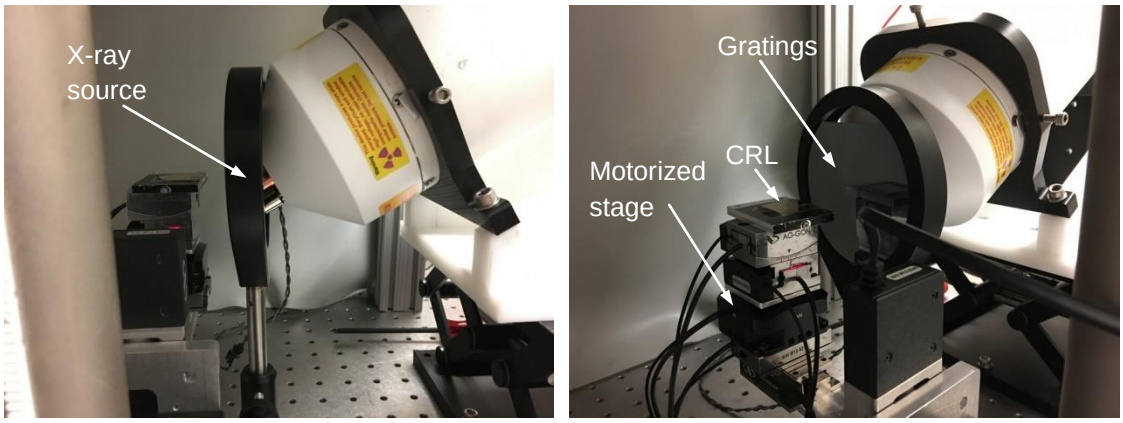

Figure 28. *Photon graphs of x-ray microscopy test setup*

The gratings were magnified by a factor of $(L_3-L_2)/(L_2-L_1)= 82$ (Figure 29). The illuminated field of view of each CRL approached the 25 µm spacing between them. As a result the three groups of grating lines appear to connect with each other. Outside the lens area, direct geometric projection was not able to resolve the grating lines due to the fact that the size of the x-ray tube focal spot is nearly three times the grating period.

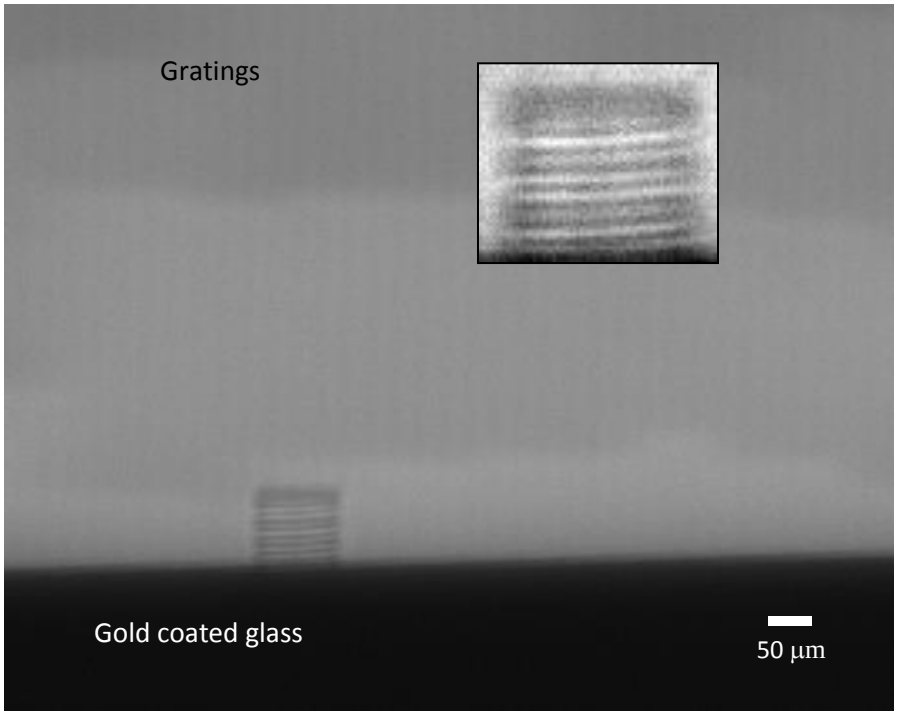

Figure 29. *Vertically magnified image of the 4.8* ***μ****m pitch grating using the cylindrical CRL. The sample-to-lens distance is 19 mm, corresponding to 82x magnification.*

Chapter 3. Bi-Directional Focusing with CRLs

3.1. Introduction

A single set of cylindrical CRL achieves focusing in one direction. As the next step towards imaging applications we explored two solutions to focus x-ray in both directions in the transverse plane. One of the solutions is an in-line arrangement of a pair of cylindrical CRLs with perpendicular lens orientation to focus the beam both vertical and horizontally. The second solution is to adopt the ability of fabricating parabolic surfaces in Nanoscribe printing to fabricate spherically focusing microlenses in one single block.

3.2. Combining a Pair of Perpendicular Cylindrical CRLs

Crossed cylindrical CRLs have been used to generate a micro beam. Both vertical and horizontal parameters of the lens will be used in this configuration. (Figure 30)

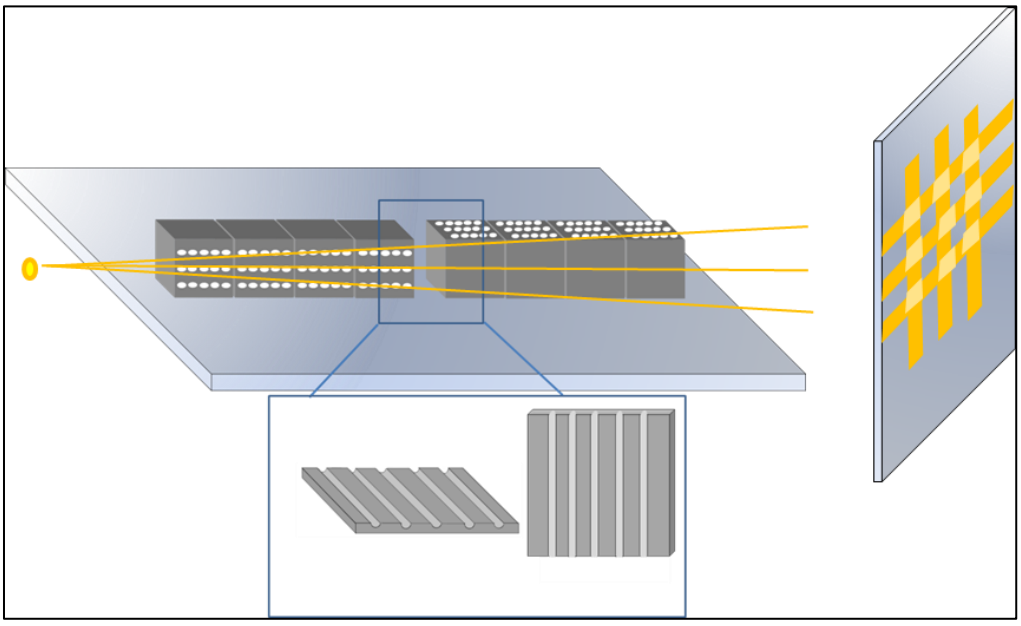

Figure 30. *Schematic of bi-directional cylindrical x-ray focusing with a pair of perpendicular CRLs.*

The resulting nano x-ray microscope consists of two 1.645 mm long horizontal structure with 16 blocks of cylindrical lenses that are placed end to end with 5 μm gap. Each horizontal block consists of three columns of 12 μm wide and 18 μm deep cylindrical duct and each column contains five stacks horizontally. The vertical block is the same structure with 90 degree rotation.

Scanning electron microscopy (SEM) image of the fabricated CRL is shown in Figure 31. The x-ray beam will pass through the lens horizontally in parallel with the substrate. The CRLs were fabricated in DiLL mode configuration with 400 nm layer height and hatching distance and a laser power level of 30 mW, which was 60% of the maximum power of 50 mW. No height curvature and no edge defect were observed in the outer side of the structure.

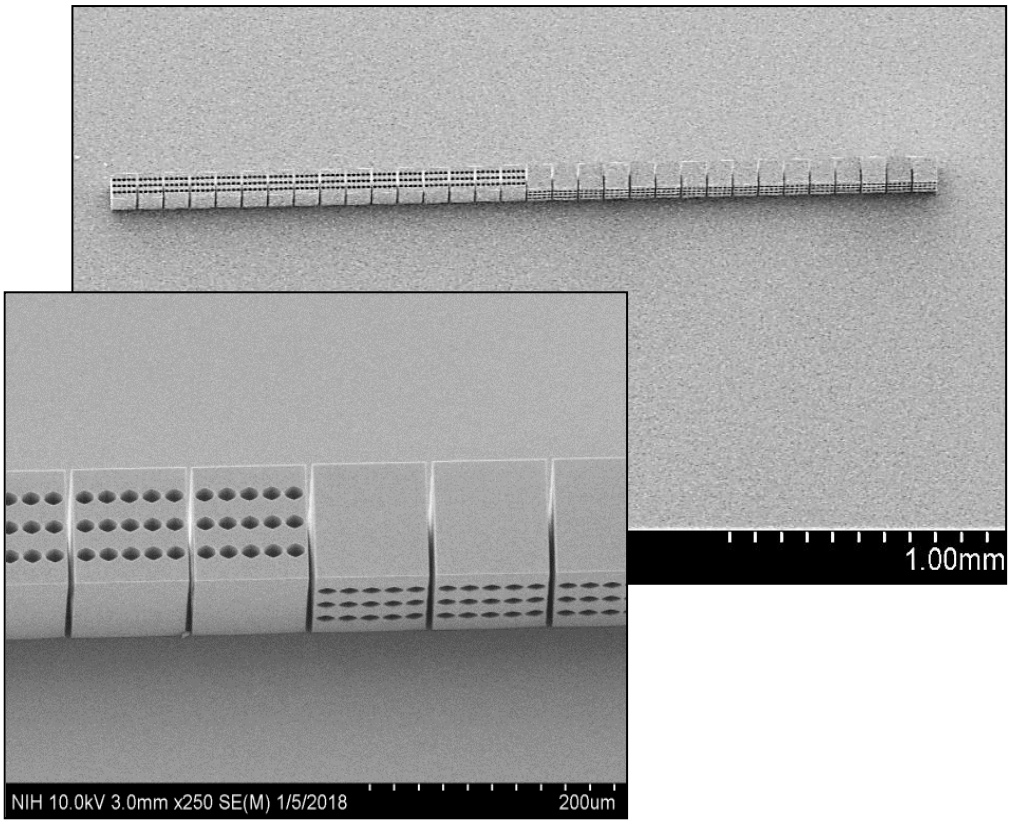

Figure 31. *Scanning electron microscopy images of the pair of perpendicular CRLs.*

Electron beams in scanning electron microscopy can only scan the surface of the structure and are not able to reach beyond the surface of the sample. Therefor the internal structure was inspected with light microscopy that took advantage of the optical transparency of the polymer material. Figure 32 shows transmitted-light bright-field optical microscopy images of the polymer blocks (Accu-Scope 3000-LED series Microscope), where the cylindrical lenses' surfaces were visible.

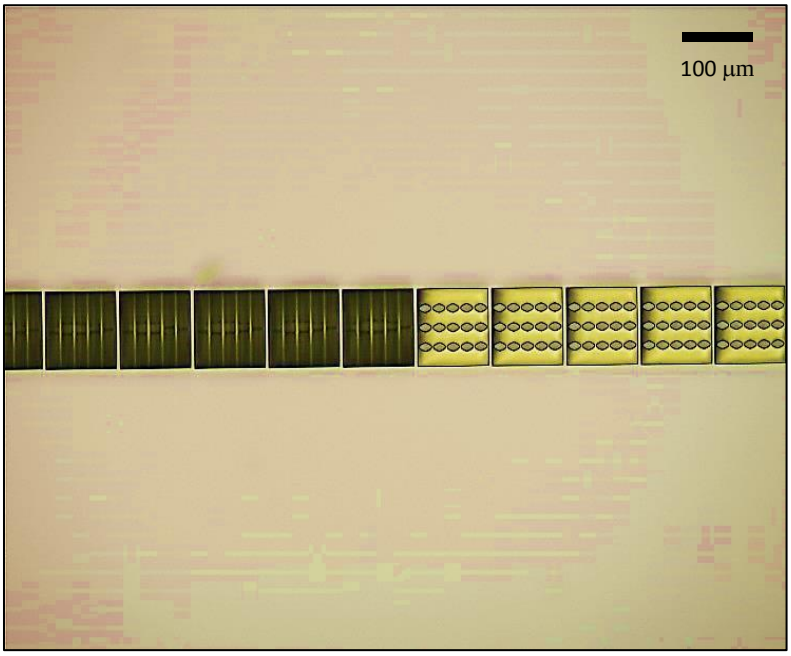

Figure 32. *Microscopy image of the cylindrical perpendicular CRLs*

3.2.1. Radiographic inspection

Given the two dimensional structure of the fabricated polymer CRL it was integrated into to Skyscan microCT to image the focal spots of x-ray sources. Since the imaged sample was the x-ray focal spot itself, no additional illumination was needed. The source was positioned at a variable sample-to-lens distance (SLD) from the CRL, and a flat panel detector was fixed at a sample-to-detector distance (SDD) of 21 mm from the x-ray focal spot. Figure 33 illustrated the focusing effect in the CRL using Skyscan microCT. The ideal focusing effect expected was two

sets of 6 symmetrical bright peaks that are crossing each other and rise above the average intensity (baseline intensity) outside of the lens. The alignment of the lens was quantified by the difference between the intensity of the peaks at the intersection and the baseline outside of the lens. Magnified image of the x-ray source spot with 60 KV source voltage and 10 W source power depicts no focusing effect compare to the area outside the lens.

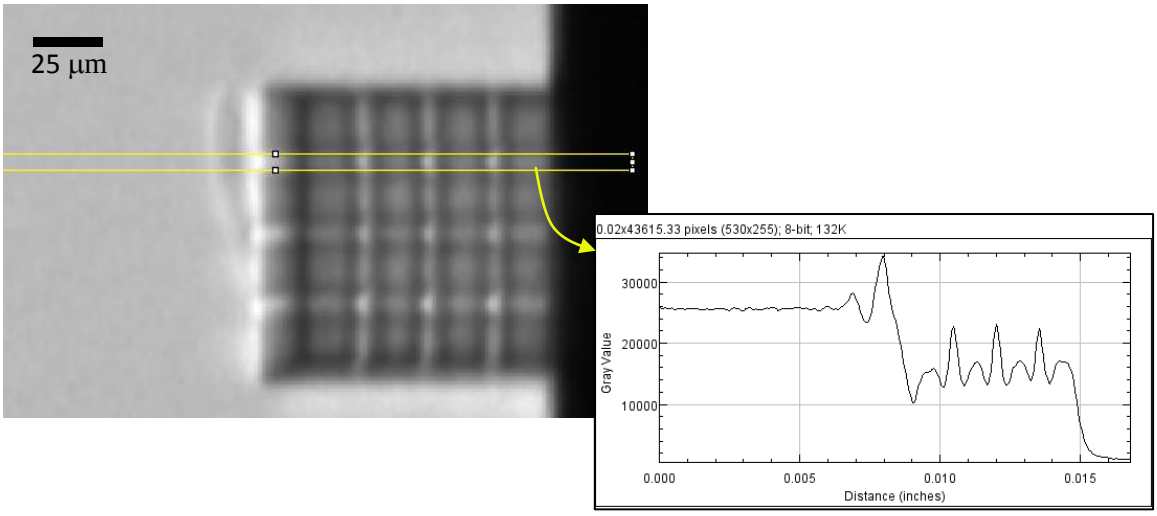

Figure 33. *Focusing effect through two sets of perpendicular cylindrical CRLs. The intensity profile at the intersections of the two sets is show in the plot.*

Since the x-ray source is polychromatic, there are wide ranges of energy spectrums in the beam. The lower energy beams will be absorbed easily while passing through the sample therefore the area around the sample will be brighter and the focusing effect can not be evaluated correctly. A 0.5 mm internal Aluminum filter is used to eliminate the lower energy x-ray spectrum. Figure 34 shows up to 80% increase in the intensity of the incident radiation at the intersection of the horizontal and vertical lines.

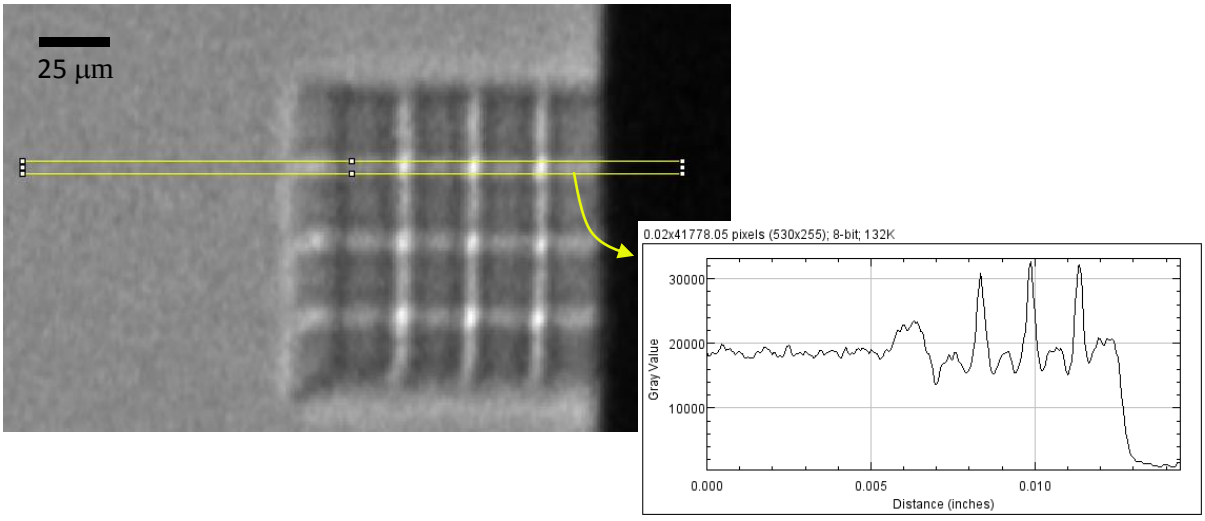

Figure 34. *Focusing effect through the two sets of perpendicular cylindrical CRLs with a 0.5 mm Al filter. At the intersection of the two, an 80% enhancement in the intensity profile is seen in the plot resulting from the bi-directional focusing effect of the CRLs.*

3.3. Spherically focusing CRL

An inline arrangement of two perpendicular CRLs to achieve spherical focusing doubles the total length of the CRL. Although not an issue for focusing a collimated beam into a spot, for microscopy and imaging applications, this design halves the imaging field of view (FOV) if the two CRLs are interleaved, due to the inverse relationship between FOV and the total length of each CRL. The alternative sequential arrangement leads to different magnification factors for the two directions. Such a combination also causes directional asymmetry of the lens point-spread function and lens aberration effects.

The ability of fabricating parabolic bubbles in Nanoscribe printing opens the opportunity to fabricate spherically focusing microlenses in one single block.

3.3.1. Design

The micro bubble lenses are actually two concave lenses put together, each lens having a parabolic shape. If the diameter of the lens is D and the height of the bowl is H, then cartesian coordinate z axis is aligned with the axis of the lens. D is fixed at 6 μm and H at 6 μm, making each bubble 12 μm in length. A vertical string of bubbles forms a compound refractive lens (CRL) in x-ray. Each block contains 9 rows of 5 bubbles, with 25 μm spacing between lenses. The total size of the structure is 100 μm^2 and there is 5 μm gap between each block. To drain the unpolymerized resist, a channel of 1.6 μm diameter runs horizontally through the midpoint of each bubble. SEM images of the fabricated lens are shown in Figure 35.

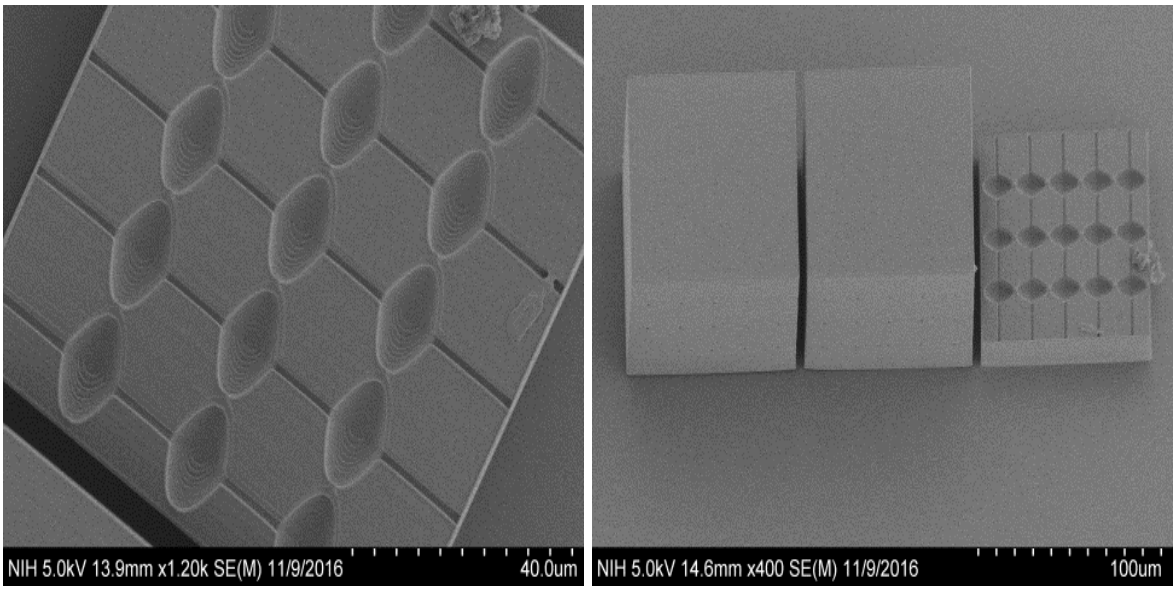

Figure 35. *Scanning electron microcopy images of the parabolic bubble lenses.*

3.3.2. Radiographic inspection

Similar to the crossed cylindrical structure, the fabricated polymer CRL it was integrated into to Skyscan microCT system to image the focal spots of x-ray sources. The source was positioned at

a variable sample-to-lens distance (SLD) from the CRL, and a flat panel detector was fixed at a sample-to-detector distance (SDD) of 282.74 mm from the x-ray focal spot. Figure 36 illustrated the focusing effect in the CRL using Skyscan microCT.

Optic results of the fabricated lenses showed that the bubble lenses are not drained compared to cylinders (Figure 36). The blur image of the bubble and the intensity profile of the lenses indicated that there were still some polymers left inside the structures.

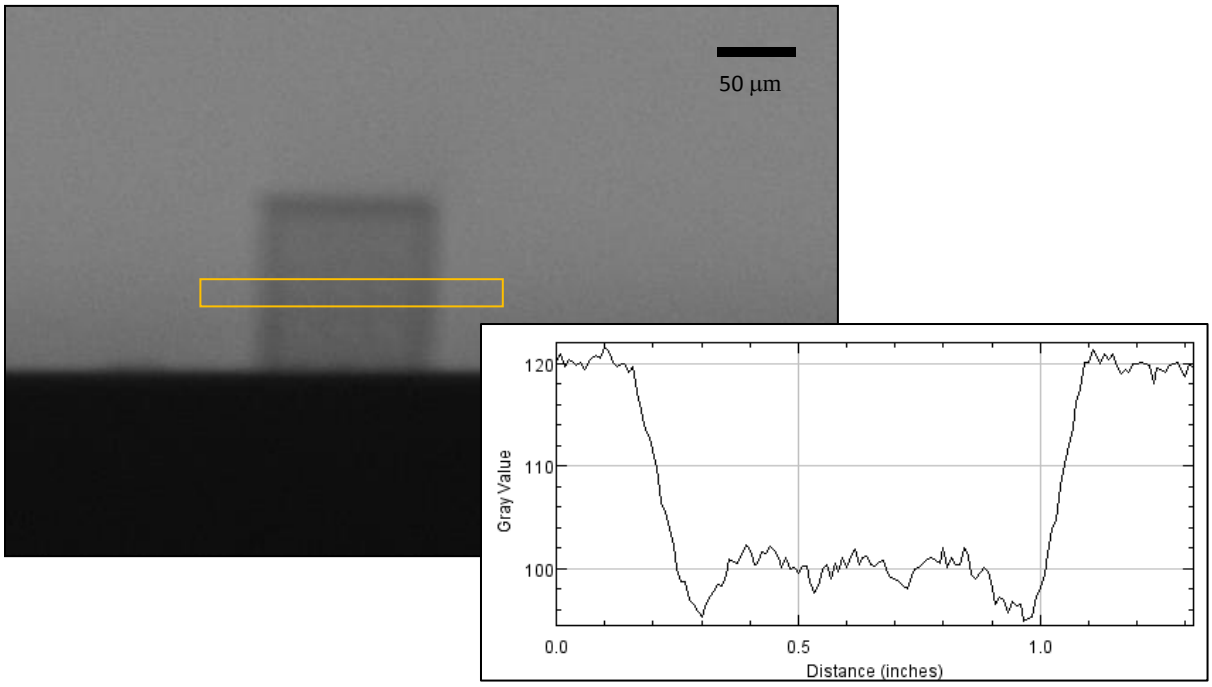

Figure 36. *Minimal focusing effect in the parabolic bubble CRL seen in the intensity profile of the x-ray beam, due to the poor developing process.*

3.3.3. Drainage channel issues

The drainage channels were allocated to deplete the cross-linked polymer during developing process. Closer look at the fabrication process depicted that the drainage channel opening closes before the rest of the channel which will lead to further obstacle for the developing process (Figure 37).

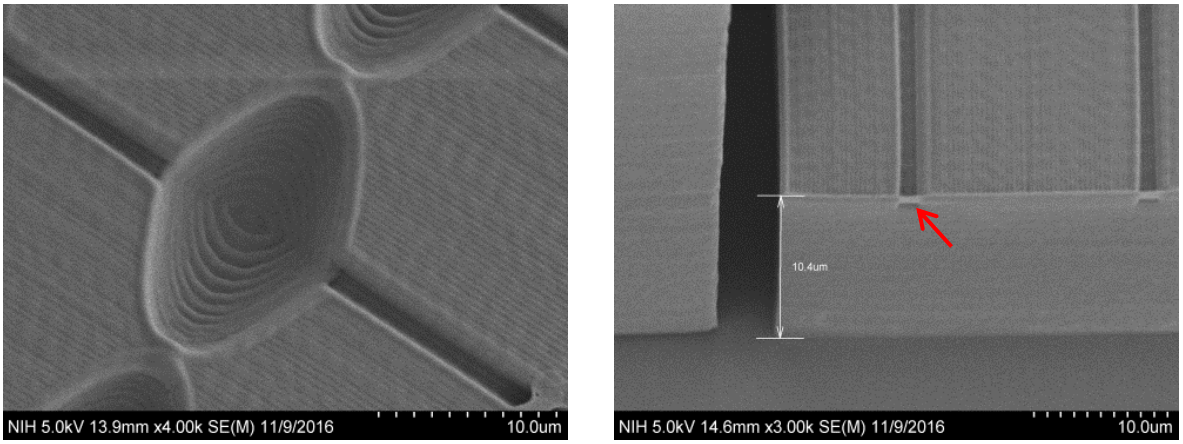

Figure 37. *The drainage channels narrow at the surface of the polymer block.*

3.3.3. Drainage channels with funnel shaped opening

In order to prevent the channel opening to close before the channel drainage, a funnel shape opening was designed for the new sets of experiment. The CRL structure was inspected with SEM (Figure 38). The size of individual blocks and the channel openings were verified.

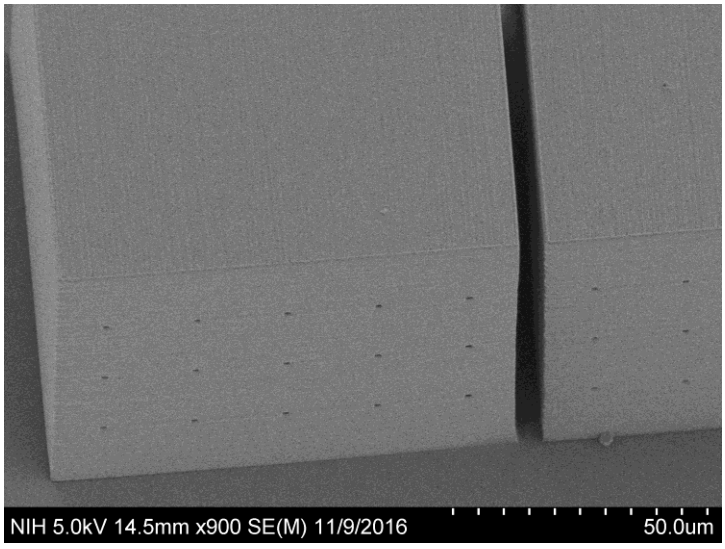

Figure 38*. Scanning electron microcopy images of the exit of the widened drainage channels for the parabolic bubble lenses.*

However SEM is not enough to inspect the internal structure of the lens. The channel details were inspected with light microscopy that took advantage of the optical transparency of the polymer material. The technique that was utilized to inspect the lens internal structure of the lens was 2-photon fluorescence imaging using a 2-photon microscope (SP8, Leica microsystems) with a water immersion 1.1 NA 25x apochromat objective (CFI75 APO 25x W MP, Nikon) (Figure 39). The sample was immersed in water, two-photon excitation was generated with an ultrafast laser (Mai tai, Spectra Physics) at 800 nm and the fluorescence emission was recorded in the 414-535 nm range with a non-descanned hybrid detector. The excitation light was blocked before detection with a 680 nm short-pass filter (Semrock). This technique allowed depth-resolved z-sectioning of the structure and cross-sectional images of the polymer blocks.

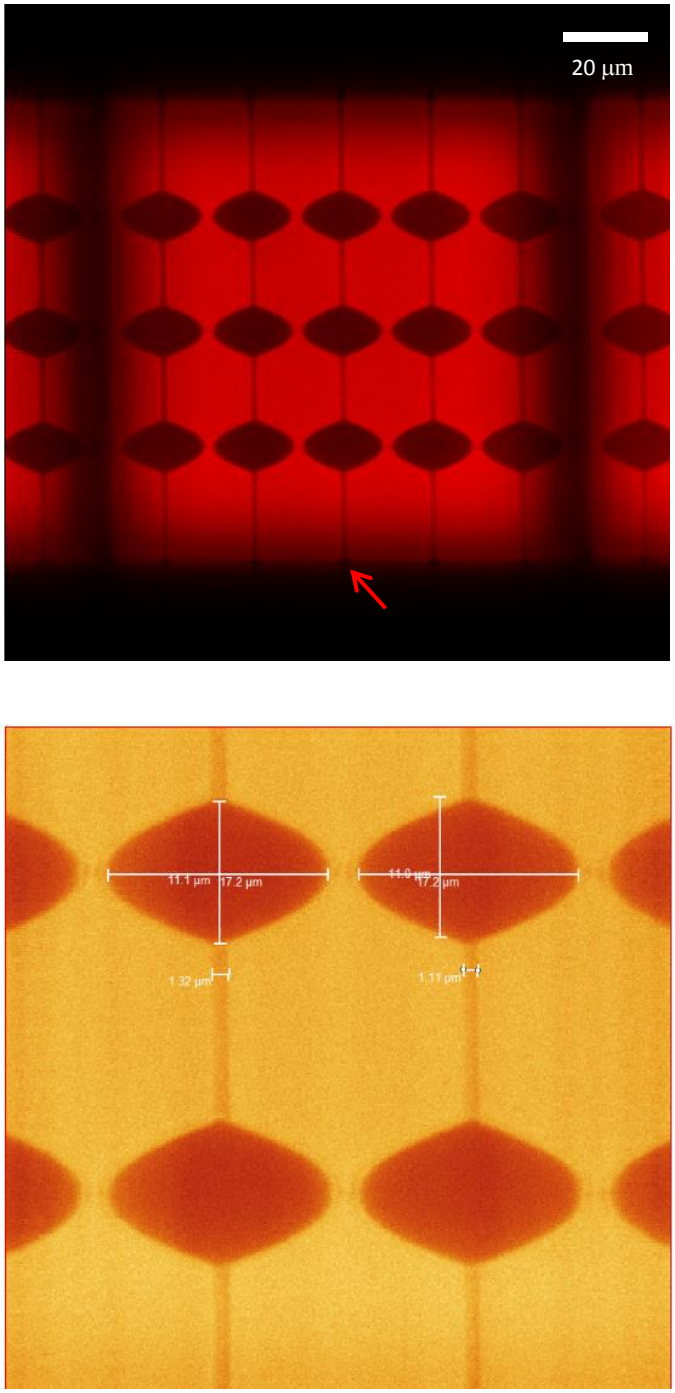

Figure 39. *Two-photon confocal fluorescence microscopy images of the parabolic bubble refractive lenses with wider openings for the drainage channels indicated by the red arrow in the top panel.*

3.3.3. Radiographic inspection

The fabricated polymer CRL it was integrated into to Skyscan microCT to image the focal spots of x-ray sources (Figure 40). Optical results showed a weak focusing effect through the bubbles. The intensity was 12% above the polymer area that is considered as blocked area and was 78% below the area around the lens.

This result contradicts with the image taken with confocal microscopy, where the bubbles were observed in the image. One possibility for the lens shape contrast in the confocal image can be due to the change in the number of carbon-carbon double bonds after polymerization. In the process of polymerization, carbon-carbon bonds are depleted to create radicalized monomers with carbon-carbon single bonds. The concentration of the carbon-carbon double bond will lead to a different contrast among the polymerized and unpolymerized resin in the confocal images of the structure. Moreover, the polymerized structure is solid and has higher density of C-H bonds, which will also cause difference in the intensity of the polymerized section.

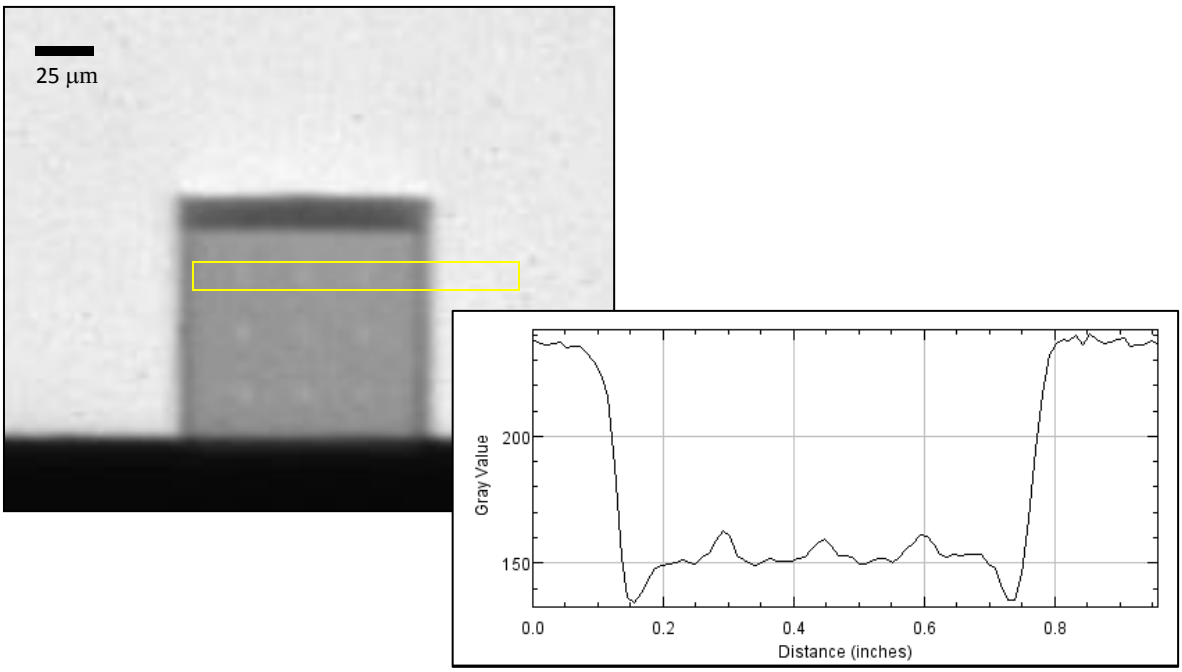

Figure 40. *Weak focusing effect by the CRLs consisting of parabolic bubble refractive lenses with wider openings of drainage channels, as seen in the intensity profile across the yellow box in the image.*

3.3. Improved design of elongated concave lenses with open parabolic surfaces

In order to eliminate the drainage channel problem, a new design is proposed that contains two elongated half bubbles that open to the side surfaces of each polymer block (Figure 41). In this design, each block consists of a 3x3 array of a pair of outward facing parabolic surfaces that form the surfaces of a bi-concave lense. Each parabolic surface has a diameter of 12 μm at its opening, and 48 μm length. No drainage channel is needed since they are self draining. The confocal image of the new design is shown in Figure 42.

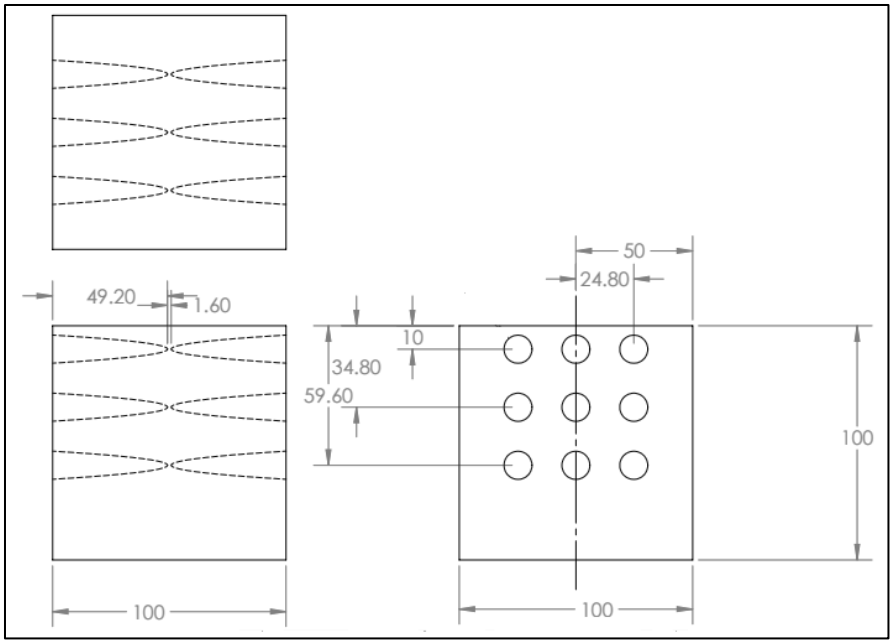

Figure 41. *Detailed dimensions of elongated bi-concave lenses.*

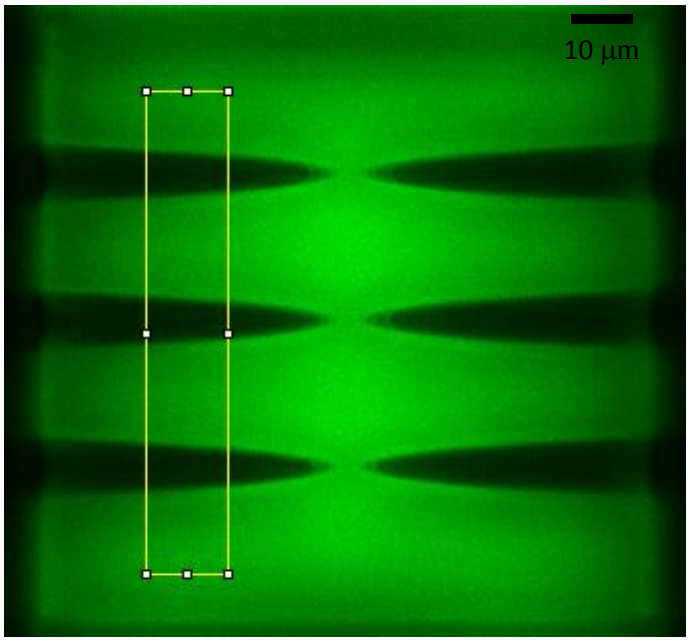

Figure 42. *Two-photon confocal fluorescence microscopy image of the fabricated elongated bi-concave lenses*

3.3.1. Radiographic inspection

The radiographic inspection of the CRLs was tested in Skyscan microCT with the setting of 60 KV/10 W to inspect the focusing effect of the CRLs (Figure 43). The result showed up to 42 % focusing above the polymer area in the lens. This means that the elongated bi-concave lenses without drainage channels focus the light 20% more than the bubble lenses with drainage channels.

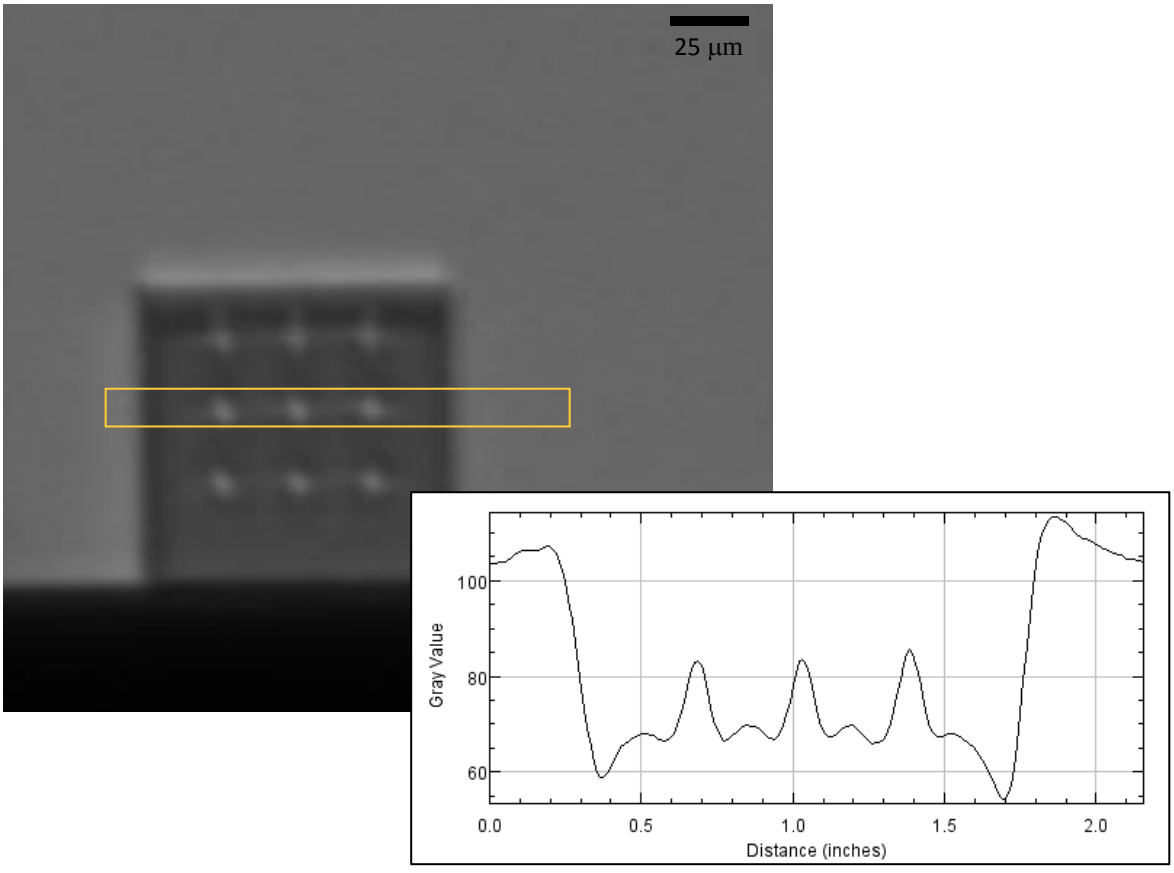

Figure 43. *The focusing effect of 50% more than the baseline within the area of the lens at 60 kV and the intensity profile in the highlighted box.*

3.5. Spherically focusing CRL consisting of 16 elongated concave lenses

In order to reduce the error of the slope near the edge of the lens and also assurance regarding the drainage of the bubbles, the depth of the lenses is cut into half. The new concave parabolic CRL consists of 16 in-line blocks with 5 µm gaps. Each block is 100 µm tall by 100 µm wide by 50 µm long, and contains an array of 3x3 parabolic indents at both the front and back surfaces. Each parabolic indent has a depth *l* of 24 µm and an opening diameter *D* of 12 µm (Figure 44). This design again provided an array of 3x3 replicates of CRL columns, giving 3x3 replicate images in imaging experiments to allow measurements of variability among them.

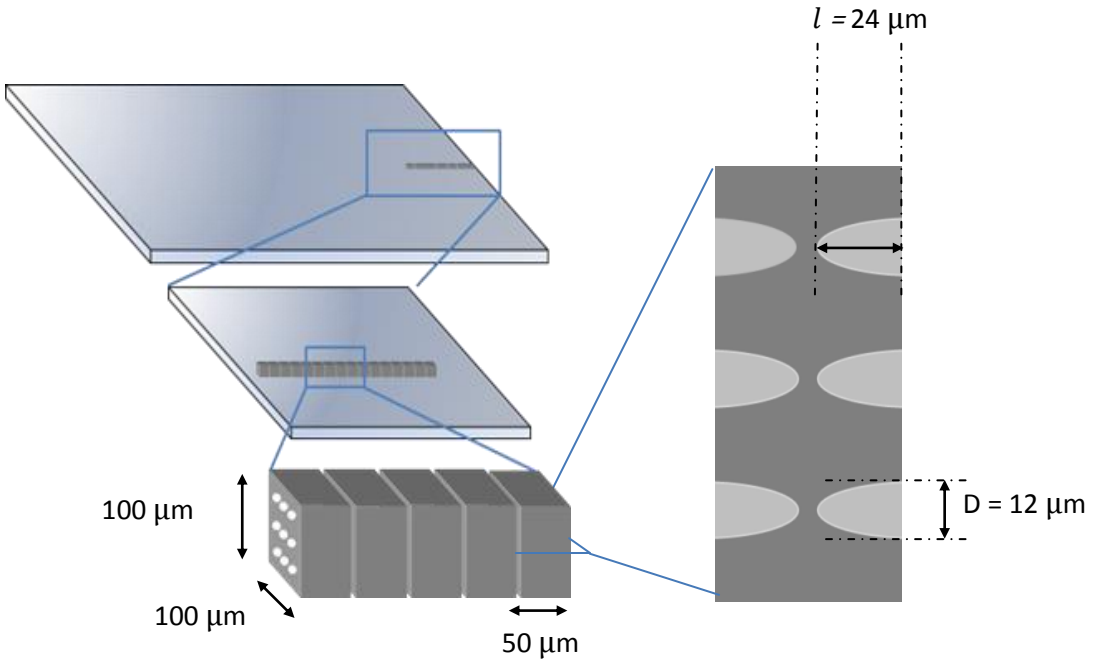

Figure 44. *Schematic of the Spherically Focusing CRL. The CRL consists of 16 in-line blocks with 7 µm gaps between them. Each block is 100 µm tall by 100 µm wide by 50 µm long, and contains an array of 3x3 parabolic indents at both the front and back. Each parabolic surface indent has a depth l of 24 µm and a diameter D of 12 µm. The design provides 3x3 replicate CRL columns, giving 3x3 replicate images in the microscopy set up.*

3.5.1. Fabrication of the improved design

The specific configuration used to print the CRL is the dip-in laser lithography (DiLL) mode of the Nanoscribe system with 400 nm hatching distance and layer thickness and a laser power level of 30 mW, which was 60% of the maximum power of 50 mW. SEM and Microscopy image of the structure (Figure 45) showed that the structures were collapsed after post bake. One reason for this problem could be the "shadowing effect" that occurred when writing separate blocks with 5 μm gap.

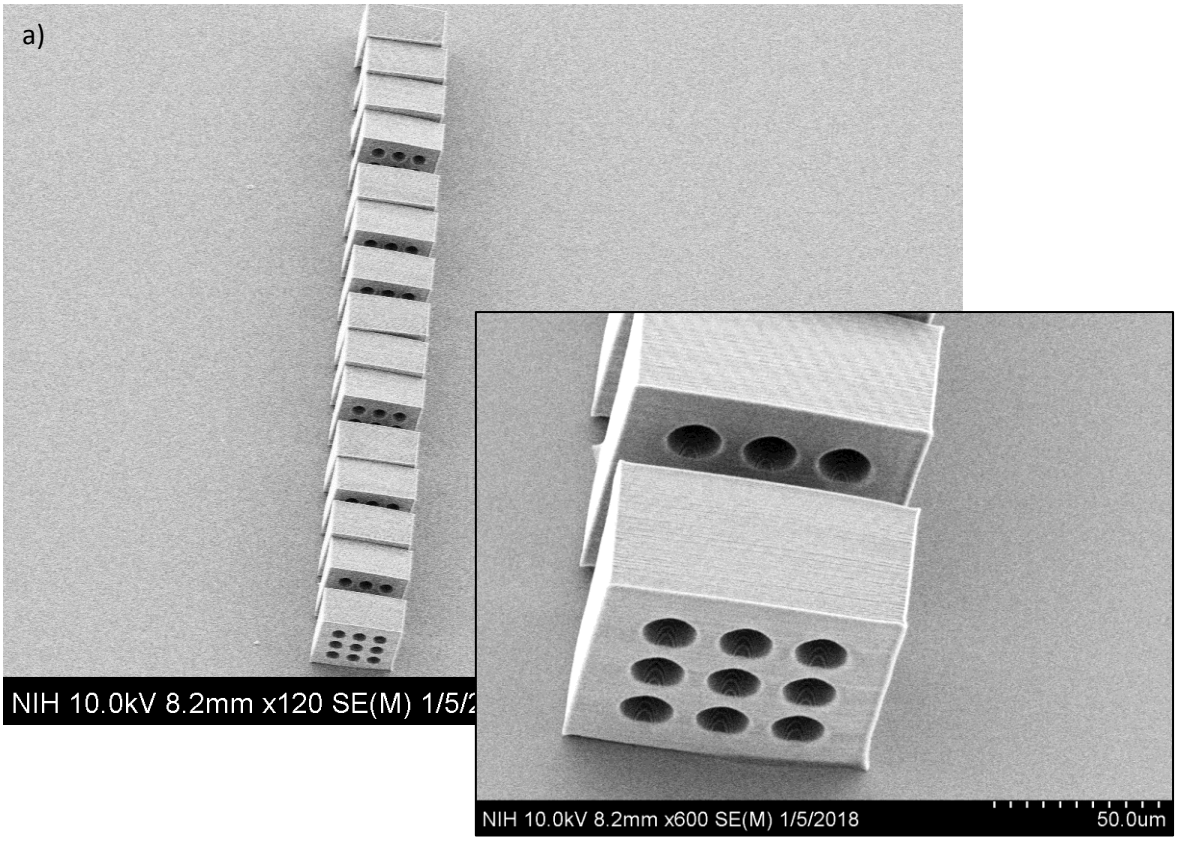

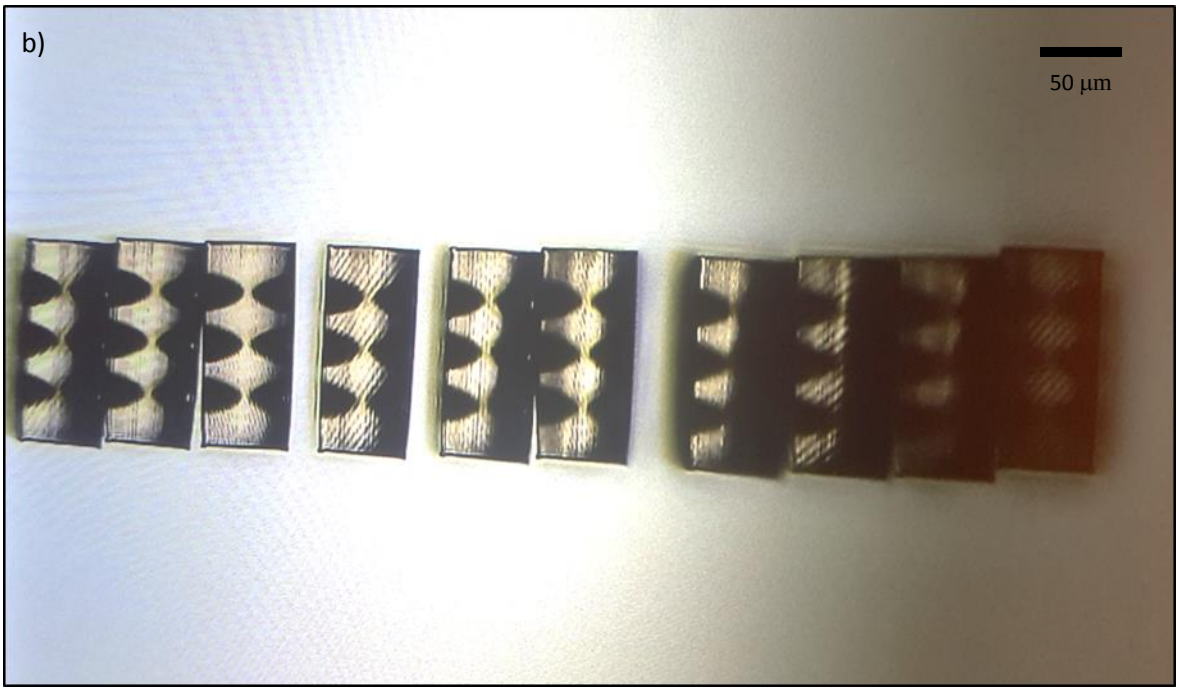

Figure 45*. (a) Scanning electron microcopy images of the elongated concave lenses. (b) A bright-field transmission microscopy image of the collapsed structure.*

3.5.2. Nanoprinting laser writing direction

The instability in the structure decreased with increasing the gap between blocks up to 7 μm. However, our experiments showed that the writing direction will also matter in the final stability of the structure. The results showed that the piezo writing direction affects the stability of the structure. The coordinate system and writing direction of the stage and piezo are shown in the Figure 46. It is a right handed coordinate system and the stage and piezo's movement are left handed.

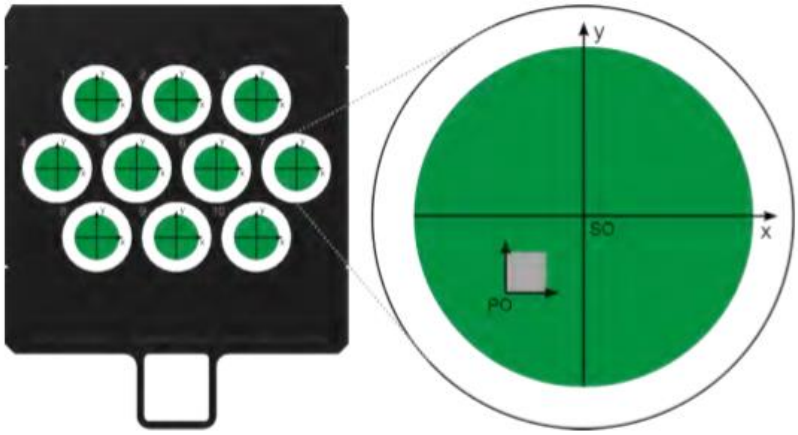

Figure 46. *Stage and piezo coordinate system. Source: Nanoscribe manual*

It's been shown that writing in piezo Y hatching direction would give a fully stable structure, compared to half collapsed blocks written in X hatching direction (Figure 47). The dark area on the right side of the CRL blocks in Figure 47a depicts that the structure is deformed.

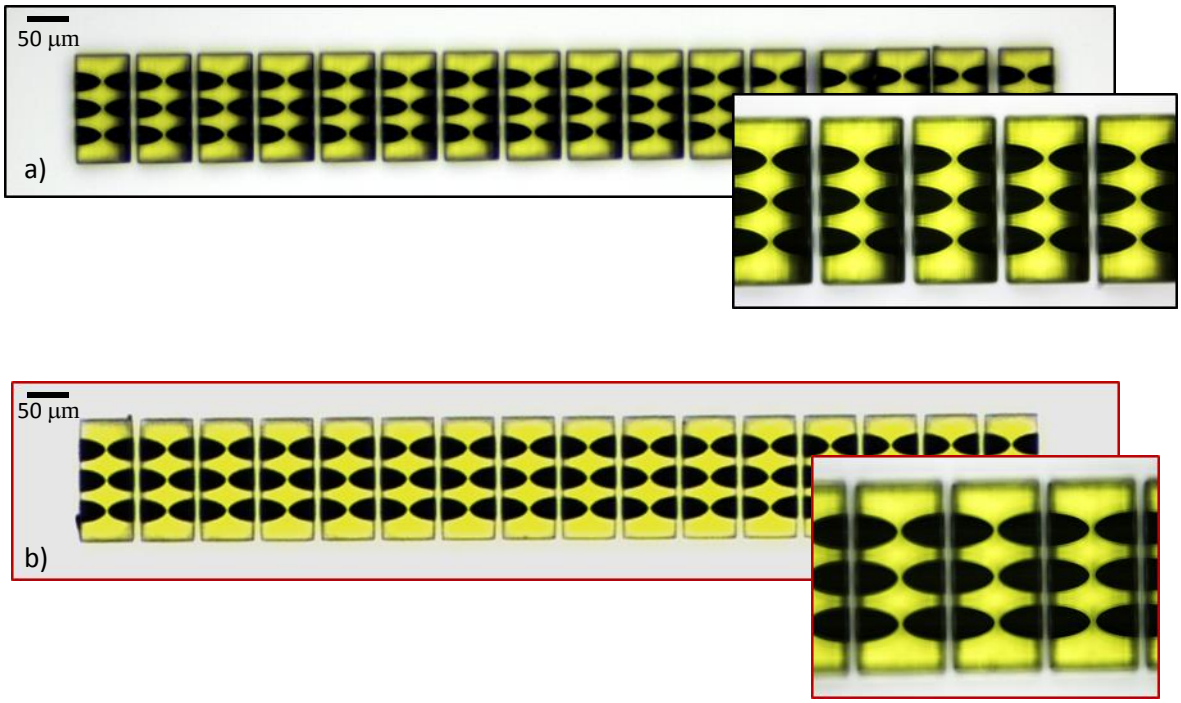

Figure 47. *Microscopy image of the concave CRLs printed in Piezo writing in a) "X" direction, and b) "Y" direction*

3.5.3. Scanning electron microscopy of the improved design

The SEM image also confirms that the lenses written in Y direction have no defects (Figure 48). The x-ray beam will pass through the lens horizontally in parallel with the substrate.

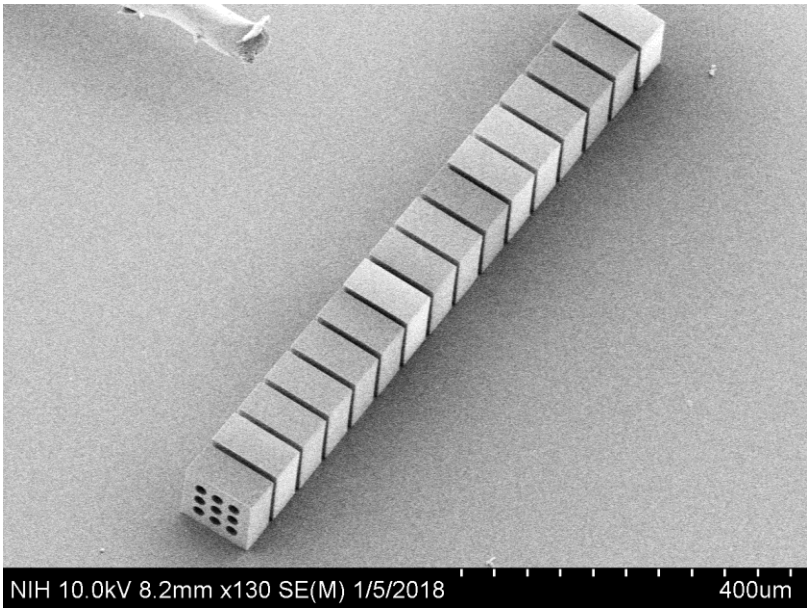

Figure 48. *Scanning electron microcopy images of the 16-block CRLs.*

The second technique that was utilized to inspect the lens internal structure was 2-photon fluorescence imaging using a 2-photon confocal microscope (SP8, Leica microsystems) (Figure 49). The sample was immersed in water, two-photon excitation was generated with an ultrafast laser (Mai tai, Spectra Physics) at 800 nm and the fluorescence emission was recorded in the 414-535 nm range with a non-descanned hybrid detector. The excitation light was blocked before detection with a 680 nm short-pass filter (Semrock). This technique allowed depth-resolved z-sectioning of the structure and cross-sectional images of the polymer blocks. The parabolic concave surfaces of the blocks are visible against the fluorescence signal of the polymer material.

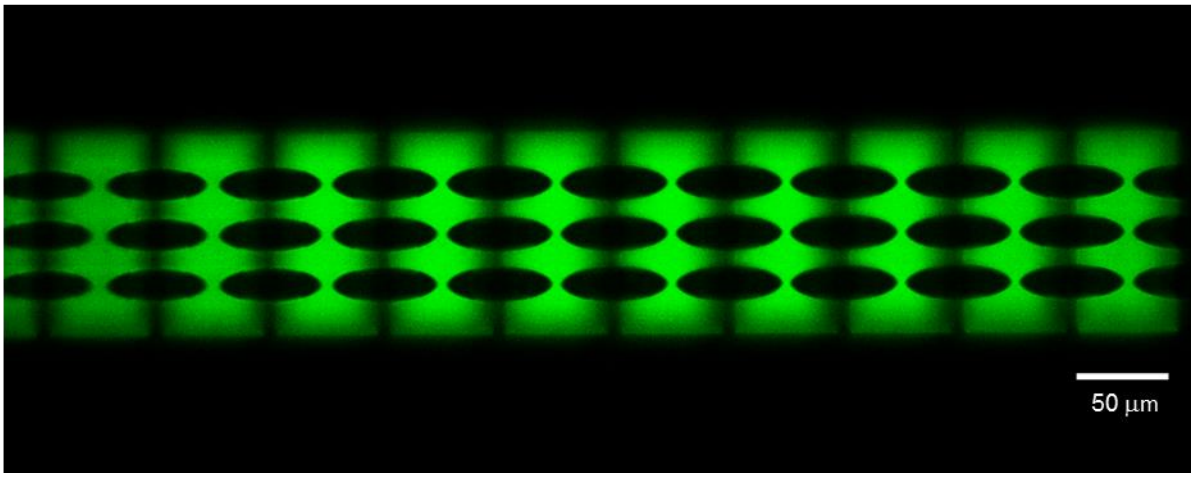

Figure 49. *Two-photon confocal fluorescence microscopy cross-sectional image at the mid-level of the first layer of parabolic concave surfaces in the blocks.*

3.5.4 Radiographic inspection

The focusing effect of the CRLs was inspected by x-ray projection radiography in the Skyscan microCT system. Figure 50 illustrates the result. At the setting of 60KV source voltage and 3W source power, the CRLs showed a focusing effect up to 95% intensity enhancement compared to the surrounding area outside the lenses.

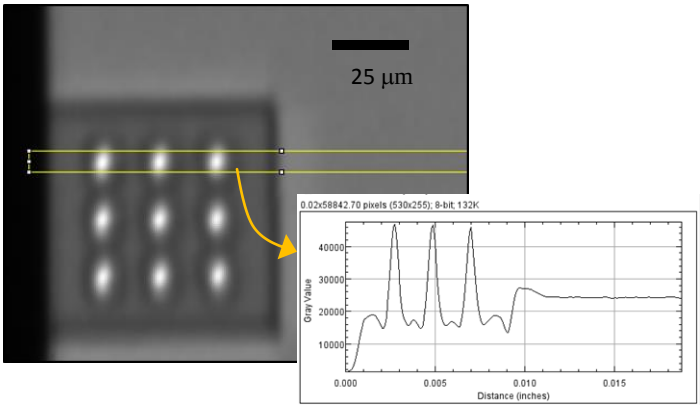

Figure 50. *Focusing effect up to 95% compared to the area outside the lenses at the x-ray tube setting of 60kV/3W.*

3.5.5. Fluorescence microscopy comparison between the first and the improved designs

The results showed that the lenses have been drained completely and no cross-linked polymer was left in the structure. This gives a good opportunity to compare the images taken by the two-photon microscopy in order to observe the cross-sectional images of the polymer blocks.

It has been shown that even if the bubble lens were not drained, the lens shape contrast was visible in the microscopy image. However, the gray level value of the lenses is about 80% of the not cross-linked polymer. This value drops to 6% in the concave bubble lens, where it's been clear that the lenses are fully drained (Figure 51).

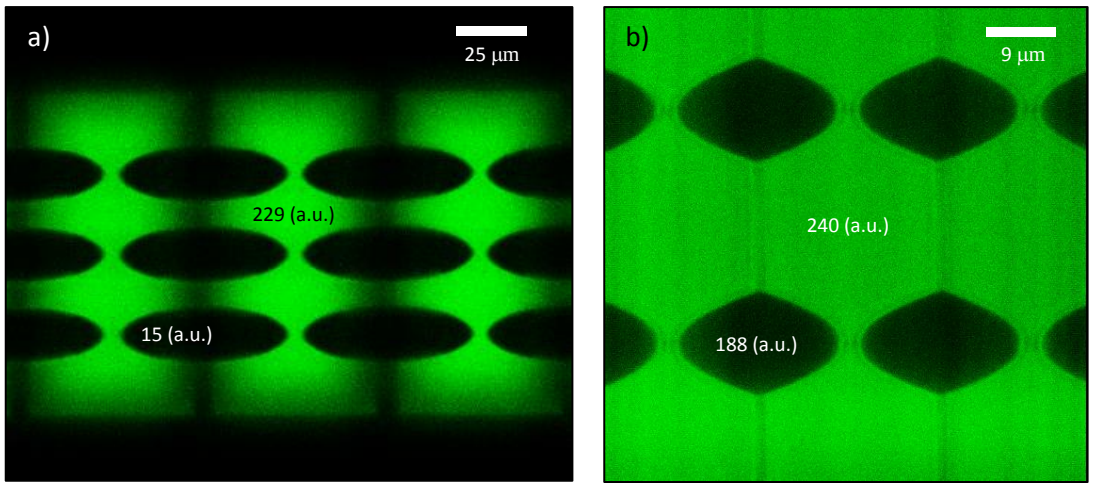

Figure 51. *Comparing the fluorescence levels in the structures of the two designs under two-photon confocal microscopy. (a) The improved design of elongated bi-concave lenses shows 94% drop in fluorescence in the parabolic indents comparing to the polymer background, implying complete drainage. (b) The first design of fully-enclosed parabolic bubbles shows a 20% drop of fluorescence in the bubbles implying a lack of drainage.*

3.5.6. Estimation of the effective aperture of the CRLs

In order to analyze the transition of the flux through the lens and the polymer, the aperture size of the lens at different kVs has been studied. A theoretical derivation that employs data from the microCT for such mea scan images in presented here. It assumes that the polymer in the lens does not absorb x-rays. However, practically this assumption is not true therefore aperture area variation with kV is expected.

Total flux through operator is:

$$F = \int_{A'} S_{(x',y')} \frac{a}{SLD^2}$$

Where $S_{(x',y')}$ is the source brightness, a, is the aperture size and SLD is source to lens distance.

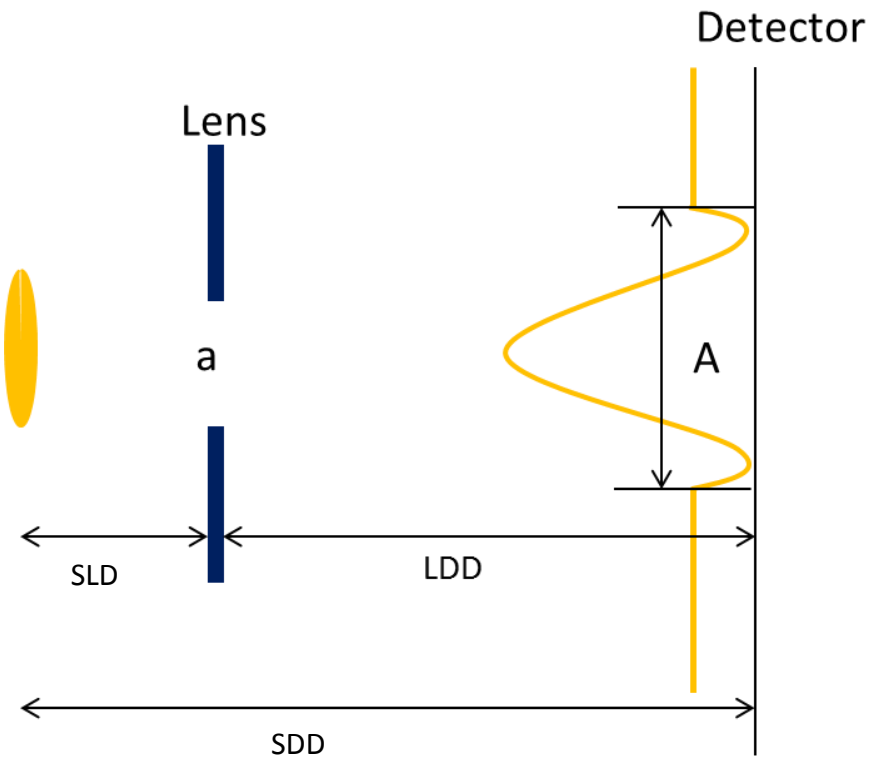

Figure 52. *Schematic of the total flux passing through the aperture.*

Total flux through aperture if it is covered by polymer is

$$F_p = \int_{A'} S_{(x',y')} \frac{a}{SLD^2} . t_p = F . t_p$$

$$F - F_p = F\,(1 - t_p) = \int_A \left(I_{(x,y)} - I_p\right)$$

Where t_p is transmission through polymer, I_p is the background polymer area intensity, $I_{(x,y)}$ is the image intensity, P is the pixel area on the detector; and FDD is the focus to detector distance.

Also, the background blank area intensity, I_{out} , can be written as

$$I_{out} = \int_{A'} S_{(x',y')} \frac{P}{SDD^2}$$

$$\int_{A'} S_{(x',y')} = I_{out} \frac{SDD^2}{P}$$

To estimate the aperture area a, assuming $\frac{I_p}{I_{out}} = t_p$

$$F = \frac{\int_A \left(I_{(x,y)} - I_p\right)}{(1 - t_p)} = \frac{\int_A \left(I_{(x,y)} - I_p\right)}{\left(1 - \frac{I_p}{I_{out}}\right)}$$

Using the expression of F, the aperture size is

$$a = F \frac{SLD^2}{\int_{A'} S_{(x',y')}} = F \frac{SLD^2}{I_{out} \frac{SDD^2}{P}}$$

$$a = P \left(\frac{SLD}{SDD}\right)^2 \frac{\int_A \left(I_{(x,y)} - I_p\right)}{(I_{out} - I_p)}$$

Results from estimated aperture size of the Skyscan microCT x-ray source with respect to the tube kV setting are summarized in Figure 53. The estimated aperture value over the tube voltage from 40 KV to 100 KV at the 10 kV increment at sample-to-lens distance (SLD) of 40 mm

which corresponds to a magnification of M= 40 was graphed. It was found that the estimated aperture size was consistent over different tube voltages. The average aperture size is measured to be 176 μm^2 which is correspondent to the lens radius of 7.5 µm. The actual aperture size of the 6 µm radius lens is 113 μm^2. The possible explanation for this observation is in the variability of the manual segmentation of the lens projection areas for the estimation, and possible deviation of the actual size of the lenses from design parameters.

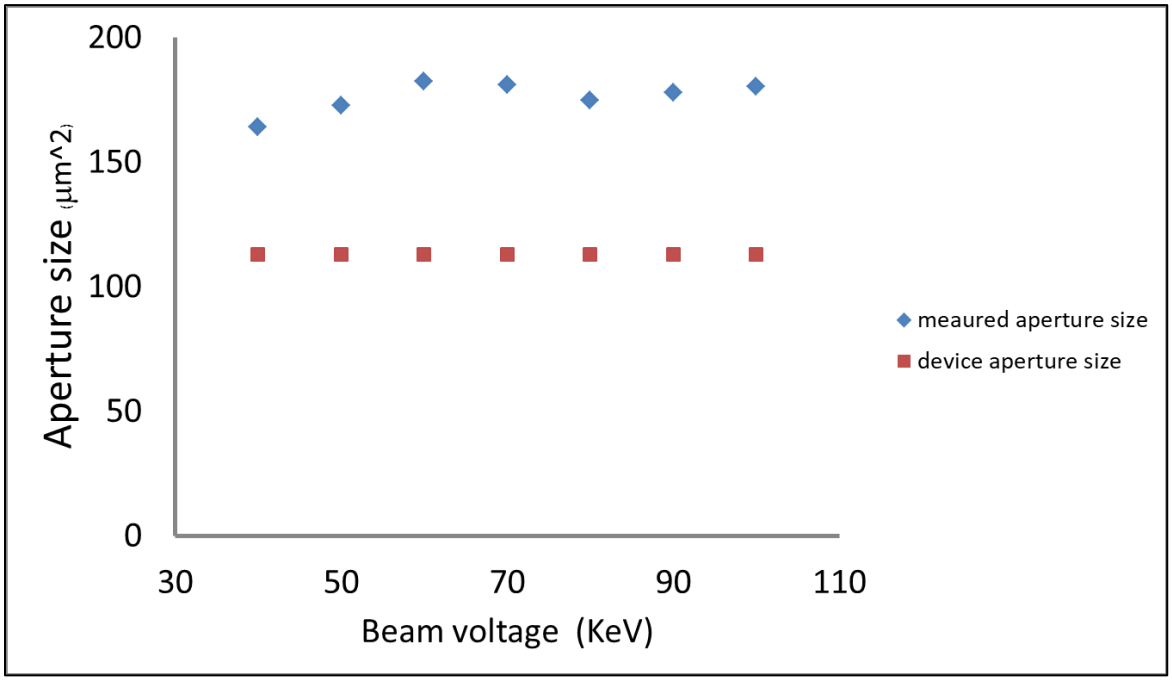

Figure 53*. Estimated aperture size of the Skyscan microCT x-ray source.*

3.5.7. Radiographic inspection with a Thermo Scientific™ Kevex micro focus source

To study the optical properties of the CRL, the focal spot of a microfocus tube was measured. Given the tabletop imaging set up, sample to detector distance (SDD) is fixed and the flat panel detector is placed at 1640 mm distance from the source and the sample to lens distance (SLD) was set at 21 mm. According to the magnification formula, M = (SDD - SLD) / SLD equals to 74.

The experimental x-ray microscopy set up as illustrated in Figure 54a uses the nanoprinted x-ray polymer lens as the magnifying lens. The first imaged sample was an x-ray source which is a fixed-anode, tungsten-target micro focus tube (Thermo Scientific™ Kevex PXS5-928) operating at various peak voltages ranging from 30 to 80 kV and 2.0 W tube power, with an average focal spot size of 5 µm. The geometric distances were 10-57 mm from the sample to the lens (SLD) and 1640 mm from the sample to the detector (SDD). Table top x-ray microscopy setup is shown in Figure 54b. A motorized stage using Newport piezo micro-positioner gives the opportunity to move the lens with sub-micron precision.

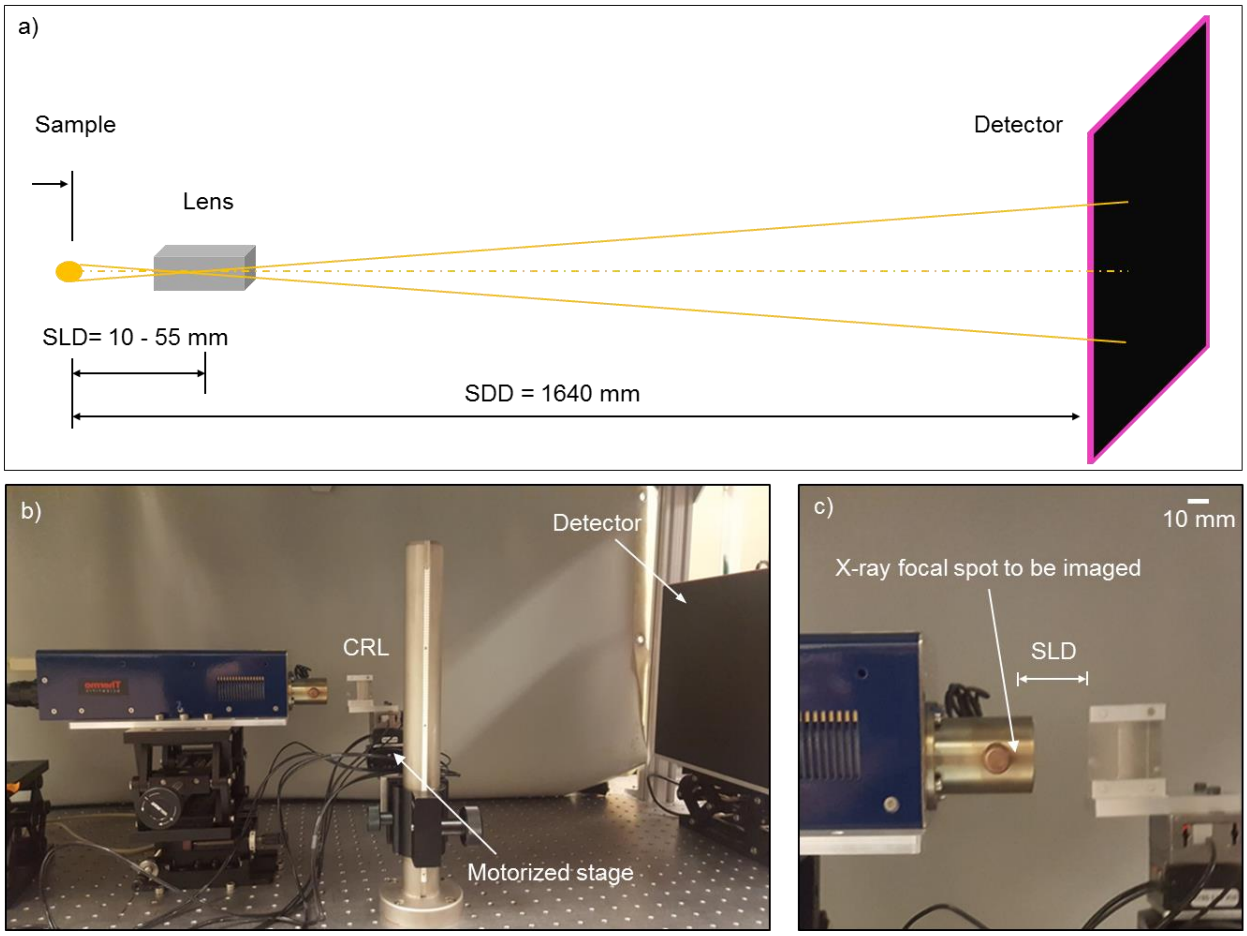

Figure 54. *Imaging the Focal Spots of X-ray Sources. (a) A schematic of the x-ray microscopy setup for imaging the focal spots of x-ray sources. The focal spots are light emitting samples and do not need*

additional illumination. The CRL is mounted on a motorized stage with all 6 degrees of movement and rotation, allowing the sample-to-lens distance (SLD) to be varied between 10 mm and 55 mm, and alignment of the lens axis with the beam. The sample-to-detector distance (SDD) is fixed. Geometric magnification is given by the ratio (SDD-SLD)/SLD, which ranged between 166 and 28.9. (b) In this photograph of an imaging experiment, the focal spot of a tungsten-target micro-focus source was being imaged. The silica substrate of the CRL was mounted vertically on the motorized stage. The detector was moved closer to the CRL from its working position to fit into the photograph. (c) A closer view of the x-ray tube window and the silica substrate of the CRL illustrate the SLD.

3.5.8 Magnified image of the focal spot of the x-ray tube

Figure 55 shows the magnified images of the 5 μm size focal spot at a high level of (~159) magnification. All images were taken with 6 second exposures. Because the polymer structure had a 3x3 array of parallel CRL columns, it could provide up to 9 duplicate images of the focal spot in each shot. The average and standard deviation among the duplicate images were measured. To evaluate the focal spot size, the intensity distribution of a spot image was integrated in the y and x directions to provide x and y profiles of the spot. Gaussian distribution of the gray-level values of each pixel in both X and Y direction was used to measure the FWHM of the lenses. These were fitted to Gaussian functions to yield the full-width-half-max FWHMx and FWHMy sizes and the focal spot position (x, y). The rotationally invariant average focal spot size was calculated as FWHM = $(FWHMx^2+FWHMy^2)^{1/2}$. At each SLD the actual spot size of the lens was calculated using the following equation:

$$\text{Source spot size} = \frac{(\text{FWHM (pixel)} * \text{Det}_p)}{M} \qquad (3)$$

Where Detp is the detector pixel size and M is the magnification.

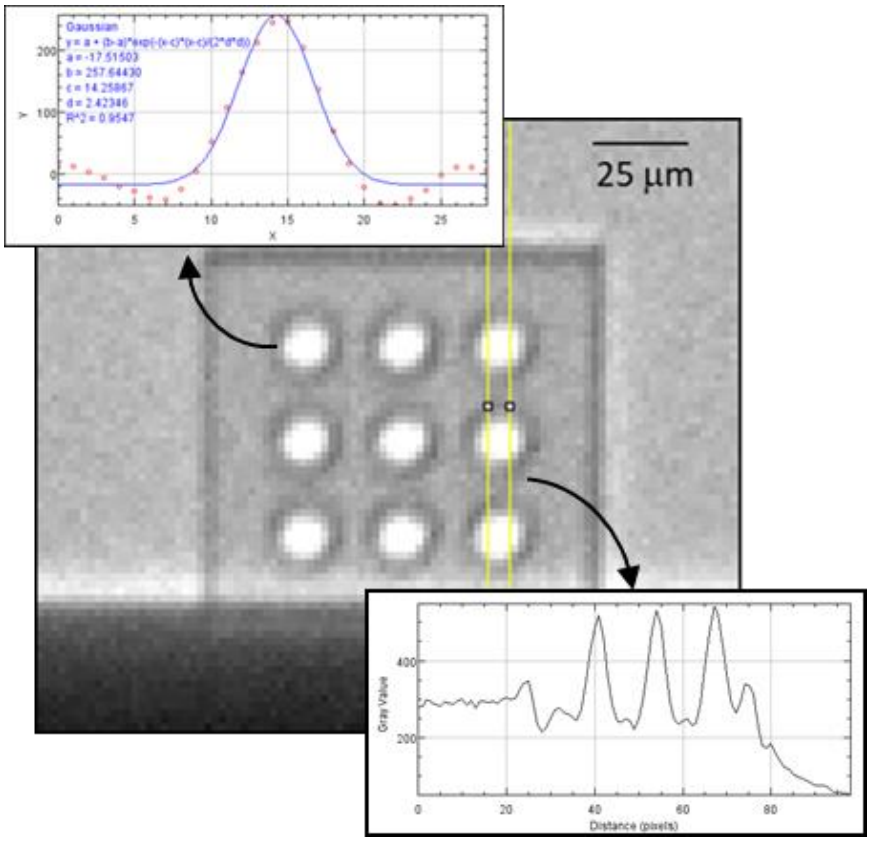

Figure 55*. Microscopy image of the 5* ***µ****m focal spot of the Thermo Scientific Kevex x-ray source*

3.5.9. Alignment of x-ray beam with CRL axis

In order to study the focusing properties of the lens, the magnified image of the lens was studied at different SLDs. To secure the fine alignment through the scan and minimizing the alignment variability, the lens was aligned on one single beam at closest and farthest SLDs. The alignment was done so that the center of the middle lenses maintained it position on the detector at the minimum and maximum SLDs (Figure 56). Therefore it can be claimed that the lens alignment at all locations between these two SLDs are within the acceptable range.

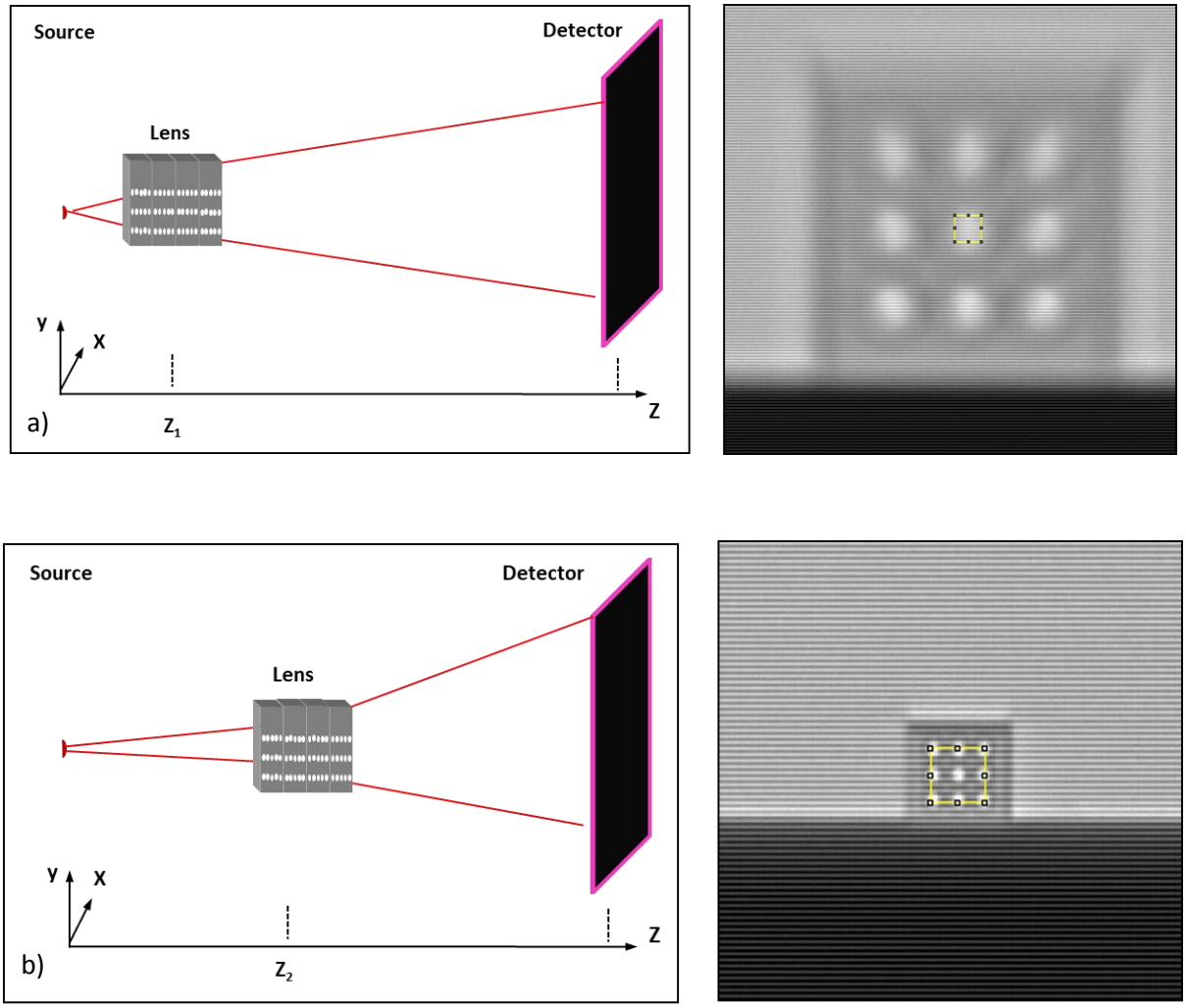

***Figure** 56. Fine alignment at a) SLD= 10.22 mm b) SLD= 55.22 mm. To illustrate the different magnification level, the reference yellow square has the same size and location on the detector for both images.*

Measuring the FWHM from the Gaussian fit of the lenses' gray value the average focal spot sizes of the x-ray tube at 60 KV for SLD = 10.22 mm and SLD = 57.22 mm was 8.97 µm and 3.46 µm respectively. At SLD = 22.22 mm which corresponds to the magnification of ~74, the spot size was 7.5 µm (Figure 57).

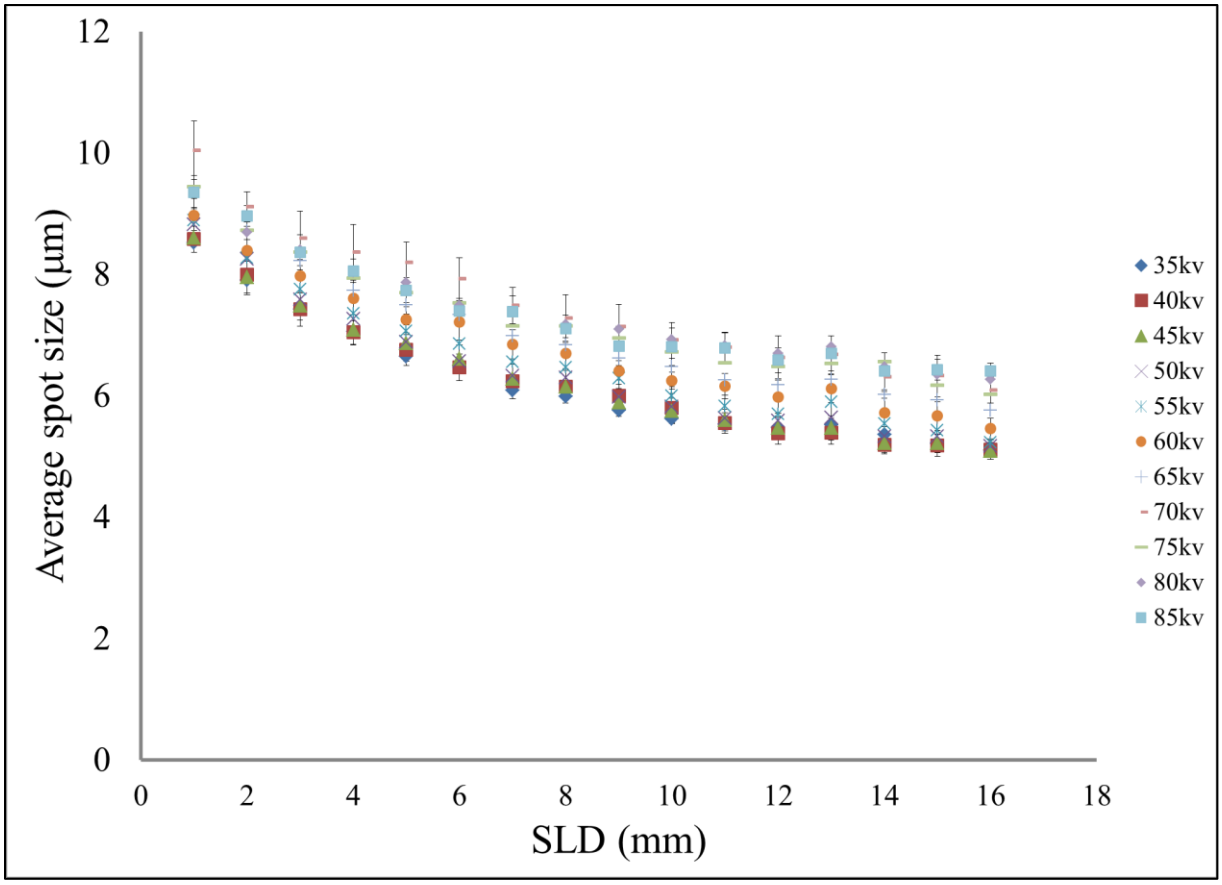

Figure 57. *Average focal spot sizes of the x-ray tube at voltages ranging from 35 to 85 kV and 6.0 W tube power.*

The results show that the focusing quality of the lens reduces significantly and the lens loses its focusing ability at short SLDs. Based on the focusing optic equations the number of lenses to focus the beam at SLD = 21 mm needs to be N = 32. In the next section, concave CRL with 32 lenses designed for focal spot = 21 mm is presented.

3.6. Third design of spherically focusing CRL with 32 elongated concave lenses

The final design consists of 32 in-line blocks with 7 µm gaps. Each block is 100 µm tall by 100 µm wide by 50 µm long, and contains an array of 3x3 parabolic indents at both the front and

back. Each parabolic surface indent has a depth l of 24 μm and a radius R of 6 μm. This design provided 3x3 replicate CRL columns, giving 3x3 replicate images in the microscopy set up to allow measurements of variability among them. Based on the refractive index of the photosensitive polymer material, the focal length at 22 keV according to Eq. (1) is 21.5 mm.

3.6.1. Fabrication

The lenses were fabricated in Nanoscribe writing in both X and Y orientation. The optical microscopy images showed that the lenses written in Y hatching direction collapsed and the ones written in X hatching direction had better stability (Figure 58).

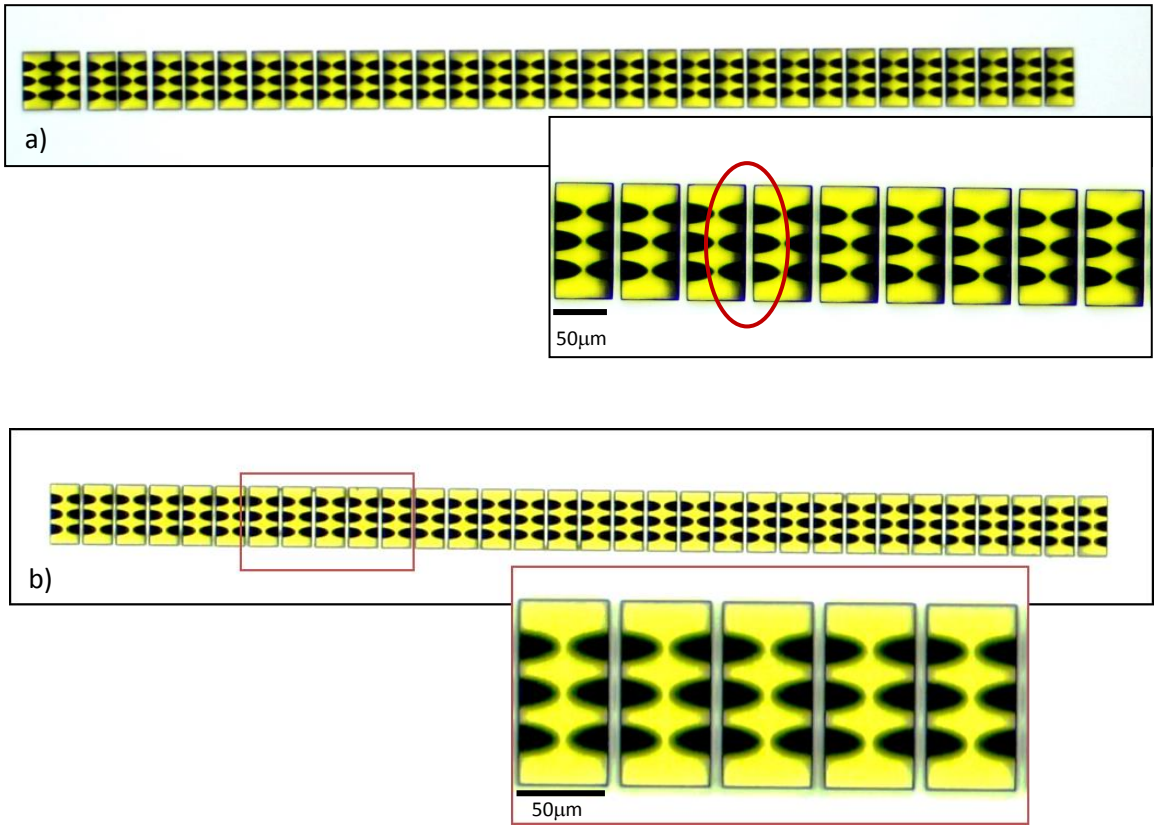

Figure 58. *Transmission microscopy image of the 32 blocks of concave refractive lenses. a) The shadow on the side of the lens depicts a structural damage in the lenses written in Y direction b) No defects found in lenses written X direction*

3.6.2. Scanning electron microscopy inspection of the CRL

The SEM image also confirms that the lenses written in x direction have no defects (Figure 59).

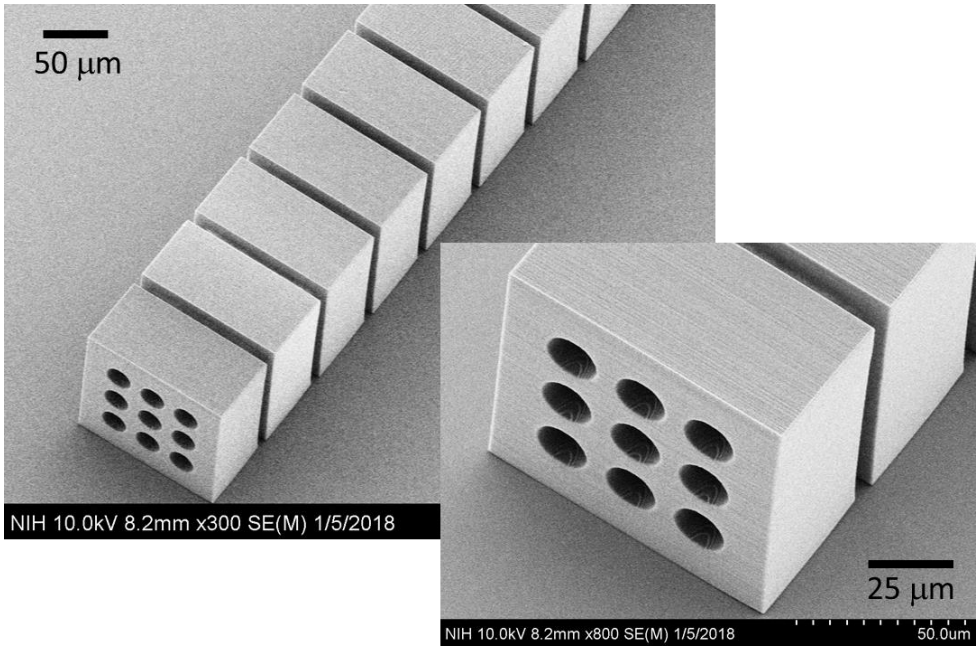

Figure 59. *Scanning electron microscopy (SEM) image of the fabricated CRL.*

3.6.3. Application of the CRL in microscopic imaging of x-ray tube focal spots

Two types of micro-focus x-ray sources were evaluated to determine the geometric magnification factor, given by M = (SDD-SLD)/SLD. The first source was a fixed-anode, tungsten-target micro focus tube (Thermo Scientific™ Kevex PXS5-928) with a vendor-specified nominal focal spot size of 4 µm at 2W power. Similar to 16 blocks lens, with this source, we tested the influence of two parameters on the measured focal spot size: the SLD was varied from 9.8 mm to 57.8 mm at 3 mm increments by moving the CRL along the beam, and the

x-ray tube voltage was varied between 25kV and 85kV. The second source was a fixed-anode, tungsten-target micro focus tube (Oxford UltraBright 96000 Series) with a vendor-specified minimum focal spot size of 13 μm. In this source, we tested two sets of parameters. First we tested the stability of the focal spot size and focal spot position at 45 kV tube voltage and 6 W power setting over a period of 15 minutes and second the stability of the focal spot at various powers from 3 to 57 W. The SLD was fixed at 21.8 mm, which was the focal distance for 22 keV photons that satisfied the relationship 1/SLD + 1/(SDD-SLD) = 1/*f*. The corresponding magnification factor M = 73.2. Both x-ray sources had 0.254 mm Be windows, and an additional 0.25 mm Al sheet was placed on the detector to eliminate low energy photons.

All images were taken with 6 second exposures. Nine duplicate images of the focal spot in each shot are provided. The average and standard deviation among the duplicate images were measured. One or two rows of the duplicate images were obscured by the shadow of the large silica substrate when the SLD was small, resulting in between 3 to 9 usable duplicates in each shot.

3.6.3. X-ray focal spot analysis of the Thermo Scientific Kevex x-ray source

The first micro-focus x-ray source (Thermo Scientific Kevex) was studied at a range of tube kV settings and a range of sample-to-lens distances (SLDs) in the imaging setup. Results with respect to the SLD parameter are summarized in Figure 60for the tube setting of 45 kV- 2 W power. Images taken at SLDs of 9.8 mm (magnification factor M = 166), 21.8 mm (M = 74), and 53.8 mm (M = 28.9) are shown in Figure 60a-c. It was found that as the SLD decreased, the silica substrate shadowed more of the CRLs. At the other end with large SLDs, the images appeared pixelated due to the lower magnifications and larger areas imaged by each detector pixel (Figure 60). Since the polymer material between the CRLs was essentially transparent to x-rays, there

was background intensity between the focal spot images, with each spot surround by a dark halo that represented the projected area of an individual CRL column. The measured horizontal profiles of the spot images outlined in Figure 60a-c are plotted in Figure 60d, together with their respective Gaussian fits. Figure 6e is a plot of the average measured focal spot size and standard deviation over the scanned range of SLDs. It was found that at 45 kV and 2 W power, the measured spot size decreased from 6.8 ±0.14 µm at the smallest SLD to 3.0 ±0.12 µm at the large SLD. At the SLD of 21.8 mm, which was the focal distance for 22 keV photons, the measured spot size was 5.17 ±0.01 µm.

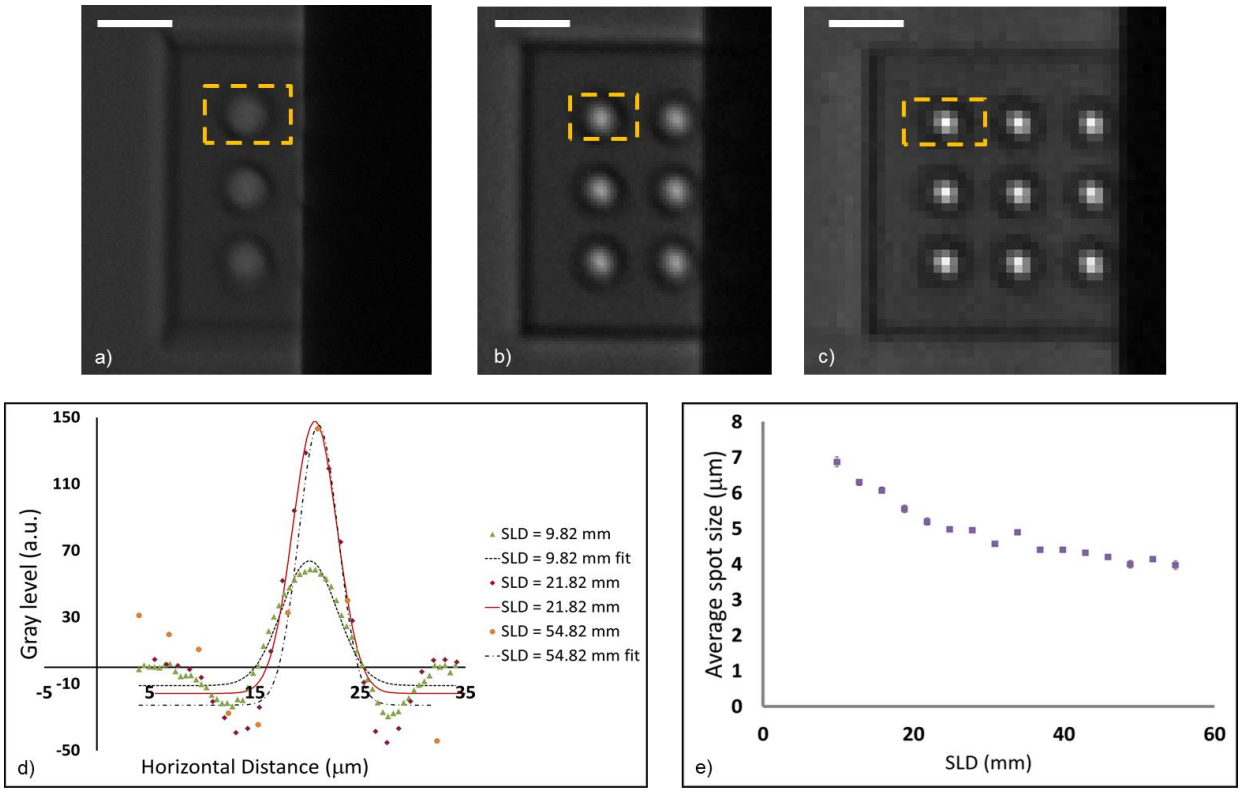

Figure 60. *Results from the First X-ray Source (Thermo Scientific Kevex) with Respect to the SLD Parameter at the Source Setting of 45 kV- 2 W Power. (a) – (c) Images taken at SLDs of 9.8 mm (magnification factor M = 166), 21.8 mm (M = 74), and 53.8 mm (M = 28.9), all displayed to the same scale represented by the 25 µm scalebars. As the SLD decreased, the silica substrate on the right*

shadowed more of the CRLs. The pixelated appearance at low magnification (c) is due to the larger area imaged by each detector pixel. (d) The measured x profiles of the spot images outlined by the yellow dotted lines in Fig. 60a-c are plotted, together with their respective Gaussian fits. (60e) A plot of the average measured focal spot size and standard deviation over the scanned range of SLDs. The standard deviations were < 0.14 µm for all measurements.

Results from the first micro-focus x-ray source with respect to the tube kV setting are summarized in Figure 61. At each SLD, the average measured focal spot size over from 25 KV to 85 KV at the 10 kV increment was graphed. It was found that the measured focal spot size was consistently the smallest at 45 kV tube voltage for all SLDs. The interpretation of this minimum is addressed in Discussion.

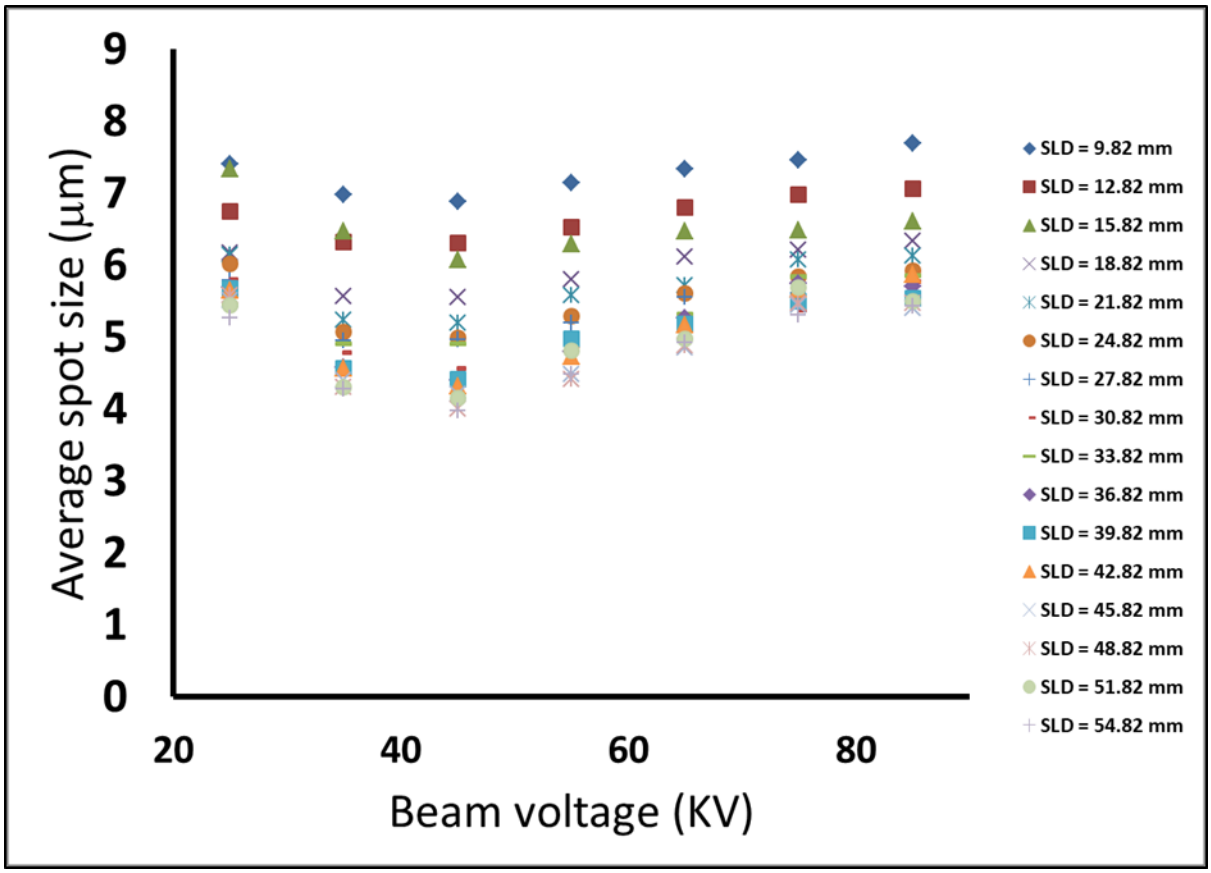

Figure 61. *Measured Average Focal Spot Size of the First X-ray Source (Thermo Scientific Kevex) as a Function of the Tube kV setting for All SLDs. The measured focal spot size was consistently the smallest at 45 kV tube voltage for all SLDs. The standard deviations of the measurements were all less than 0.22 μm.*

Several questions emerge from the presented experimental data. The measured focal spot size of the first x-ray source at 45 kV decreased gradually with increasing SLD, even beyond the designed focal distance (Figure 60). We speculate two possible reasons for the trend. One is that at large SLDs/low magnification, each detector pixel covers a larger area of the focal spot, leading to increasing under-sampling of the spot profile (Figure 60c) and possible systematic under-estimation of the width of the underlying profile. Another possible reason was that the higher parts of the x-ray spectrum (> 22keV) continually come into focus with increasing SLD.

The measured spot was the smallest at 45 kV at all SLD values. There are two possible explanations for this observation. One is that the x-rays were over-focused at < 45 kV and under-focused at > 45 kV, while another is that the x-ray focal spot size was actually voltage dependent. Considering the fact that the minimum was consistent for all SLDs, the data dispute the first explanation, and are more consistent with an actual voltage dependence of the focal spot size.

The field of view (FOV) of the CRL for high magnification microscopy, where the SLD is approximately equal to the focal length, is estimated to be 2R*f/L. The FOV was 145 μm for the CRL design explored here. Given the inverse relation of the FOV to the total length L of the CRL, the ability of the nano-printing system to pack the lens blocks tightly reduced the total length L and helped enhance the FOV. Adding 7 mm gap between CRL blocks will reduce the FOV of the ideal design by 20 μm, which is a tradeoff between the focusing effect and the FOV.

3.6.4. X-ray focal spot analysis of Oxford Ultrabright x-ray Source

Imaging of the second micro-focus x-ray source focused on the stability of the size and position of the focal spot when operating at 45 kV and 6 W power. Results of the focal spot size measurements are summarized in Figure 62. Figure 62 includes an example shot containing 9 duplicate images of the focal spot from the 3x3 array of CRL columns. It also shows the line profile of the spot intensity in the x direction, and the Gaussian fit of the profile to quantify its FWHM and peak position. The average spot size of the 9 duplicate images as a function of time was plotted with a linear regression line of $R_2 = 0.89$. The measured spot size fluctuated by 0.1 μm at each time point and expanded gradually by 5.5% over the 15 minute period, from 9.44 μm to 9.96 μm.

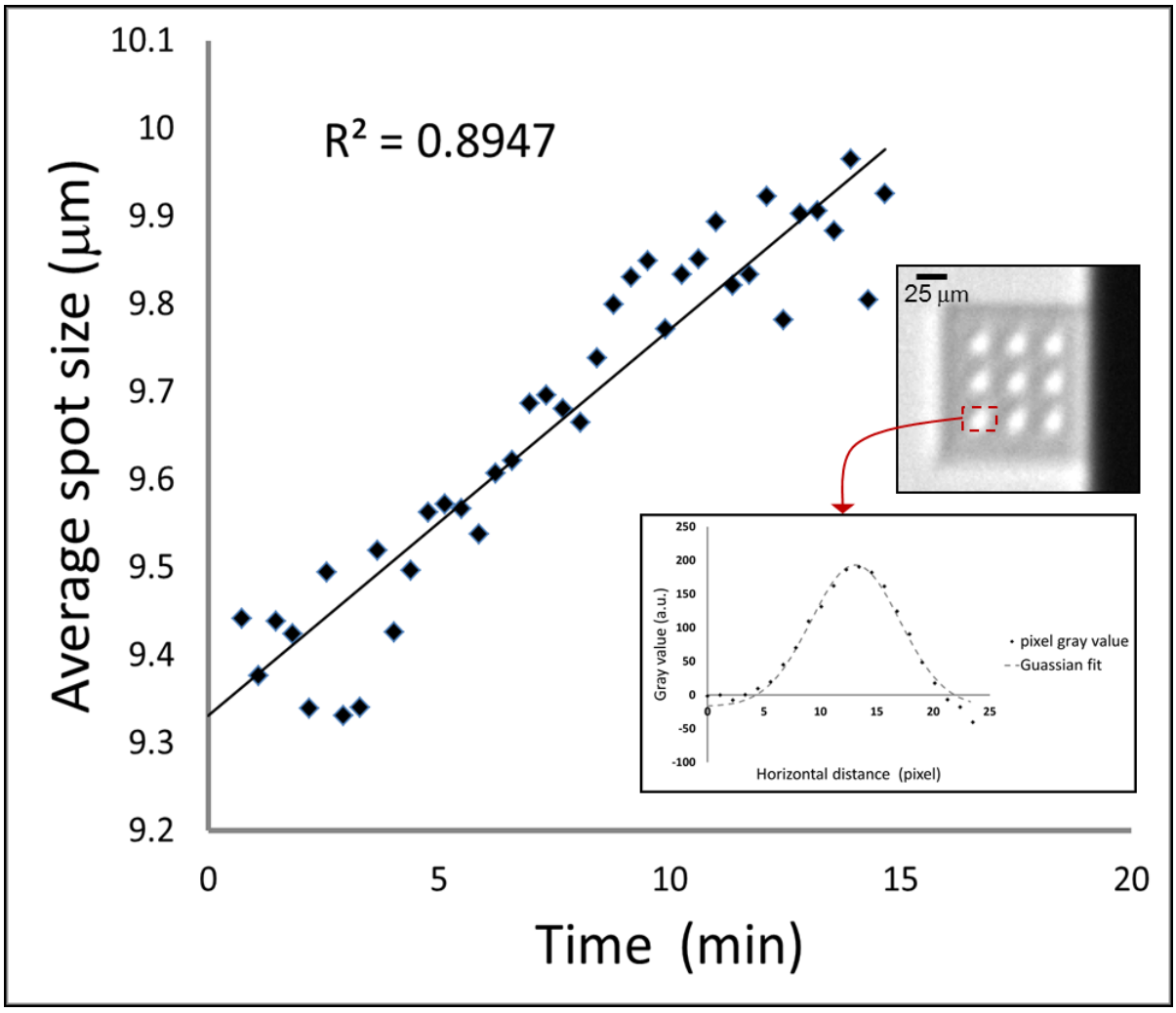

Figure 62. *Average Focal Spot Size Over Time for the Second X-ray Source Operating at 45kV/6W. The upper inset is an example shot of 6 second exposure which contained 9 duplicate images of the focal spot from the 3x3 array of CRL columns. The lower inset is the x intensity profile of a spot and its Gaussian fit. The main plot is the average FWHM of the 9 duplicate spot images as a function of time. The average spot size fluctuated by 0.1 μm at each time point and expanded by 5.5% over the 15 minute duration.*

Data revealing drift of the focal spot position are graphed in Figure 63. Since the image taken at each time point contained 9 duplicate images of the focal spot, the peak positions of the 9 spots were individually determined with Gaussian fits, and relative displacements of the peak positions from the first shot were averaged over the 9 duplicates. The average x and y displacements over

time are plotted in Figure 63. It illustrates that the focal spot moved unidirectionally in the horizontal direction by 0.6 µm. In the vertical direction, however, the focal spot initially moved down for 0.5 µm in a 2 minute period, then reversed direction and moved up 1.6 µm over the remaining 13 minutes.

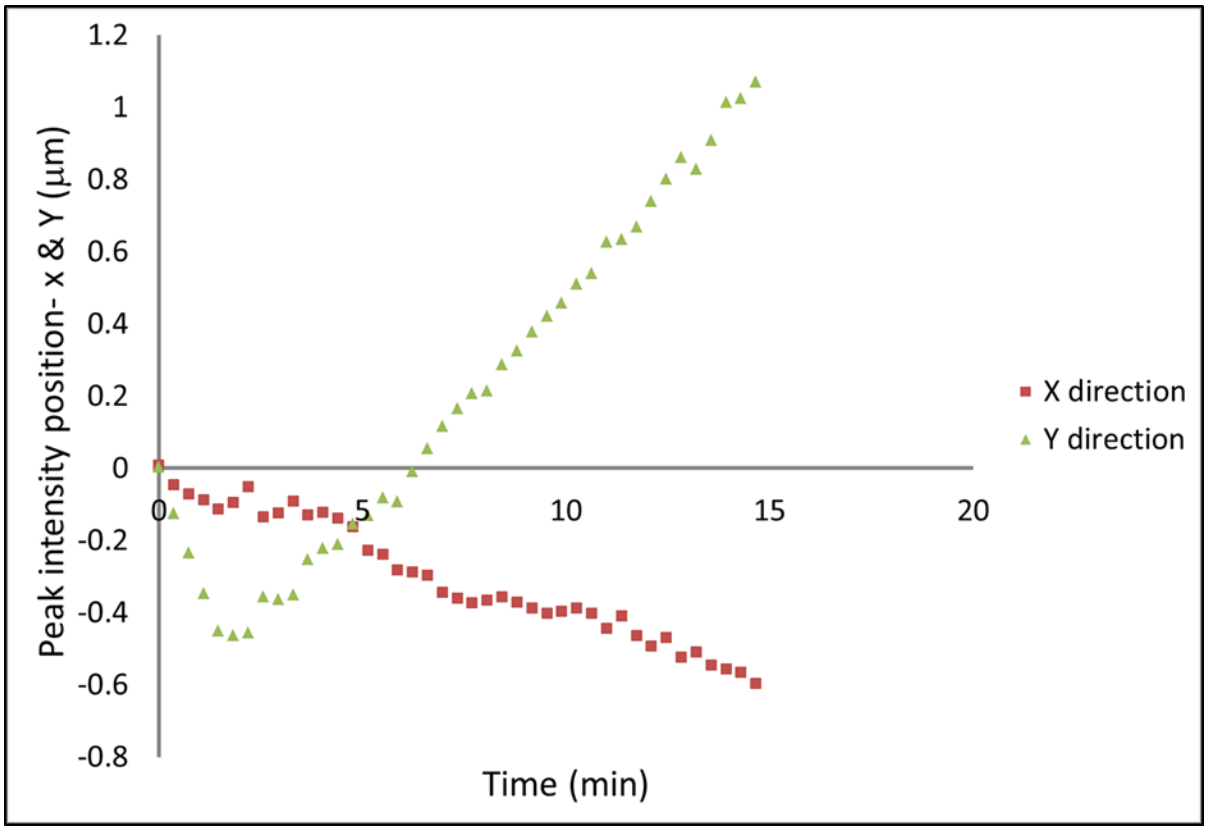

Figure 63. *Drift of the Focal Spot Position of the Second X-ray Source Over a Period of 15 minutes in x and y Directions. Each measurement is the average of the 9 duplicate images of the focal spot from the 3x3 array of CRL columns. The standard deviations of the measurements were < 0.1 µm.*

3.6.5. Power dependence of the focal spot of the Oxford Ultrabright source

Figure 64 shows average spot size of the x-ray tube along with the magnified image of the ~10 µm size focal spot of the 9 individual lenses for magnification of ~80 at 45 KV. The average spot size of the x-ray tube at 45 KV for SP (source power) = 3 W and SP = 57 W was 9.73 µm and

9.24 µm respectively. However, the contrast of the low power image is 43% and 2.67% for the high power scan.

It indicates that the tube was able to maintain its spot size through a wide range of power settings. However, at the source power starting from 30 W, the standard deviation increased significantly up to 20% and the precision of the experiment decreased, which means that the lens images became blurry with low contrast compare to the images at the source power < 30 W.

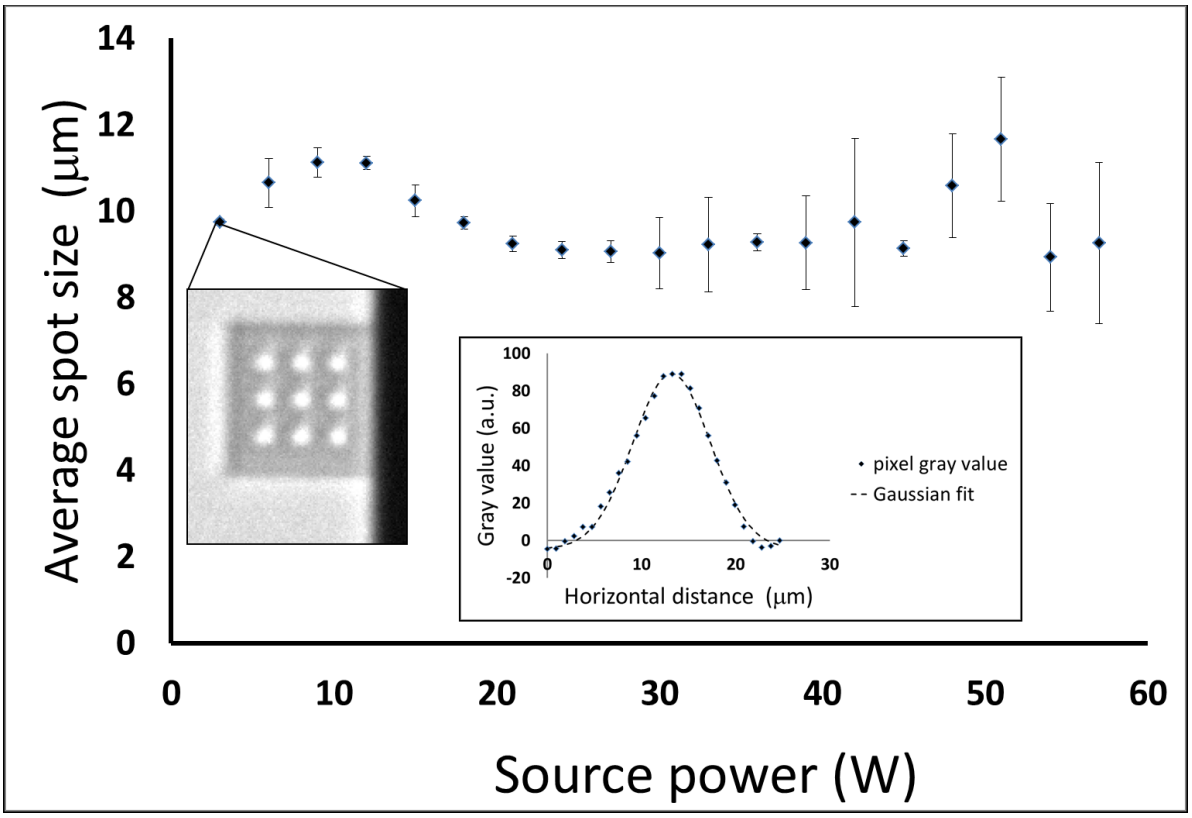

Figure 64. *The tube was able to maintain its spot size through the power scan, however the precision of the measurement decreased by increase in power above 30 W.*

The trend of the contrast is shown in Figure 65. It illustrates that the contrast drop occurs when power is increased. At source power > 30 W, the contrast drops below 15%. The result indicates a particular x-ray emission pattern by the x-ray tube at higher power outputs: in addition to

emission from the focal spot, there is a rising proportion of background x-ray emission in the surrounding area that is larger than the 25 µm spacing between the CRL columns. The background emission leads elevated background intensity in the image and decreased contrast of the focal spot. This is also the cause of the significant edge burring in the images taken at higher power levels.

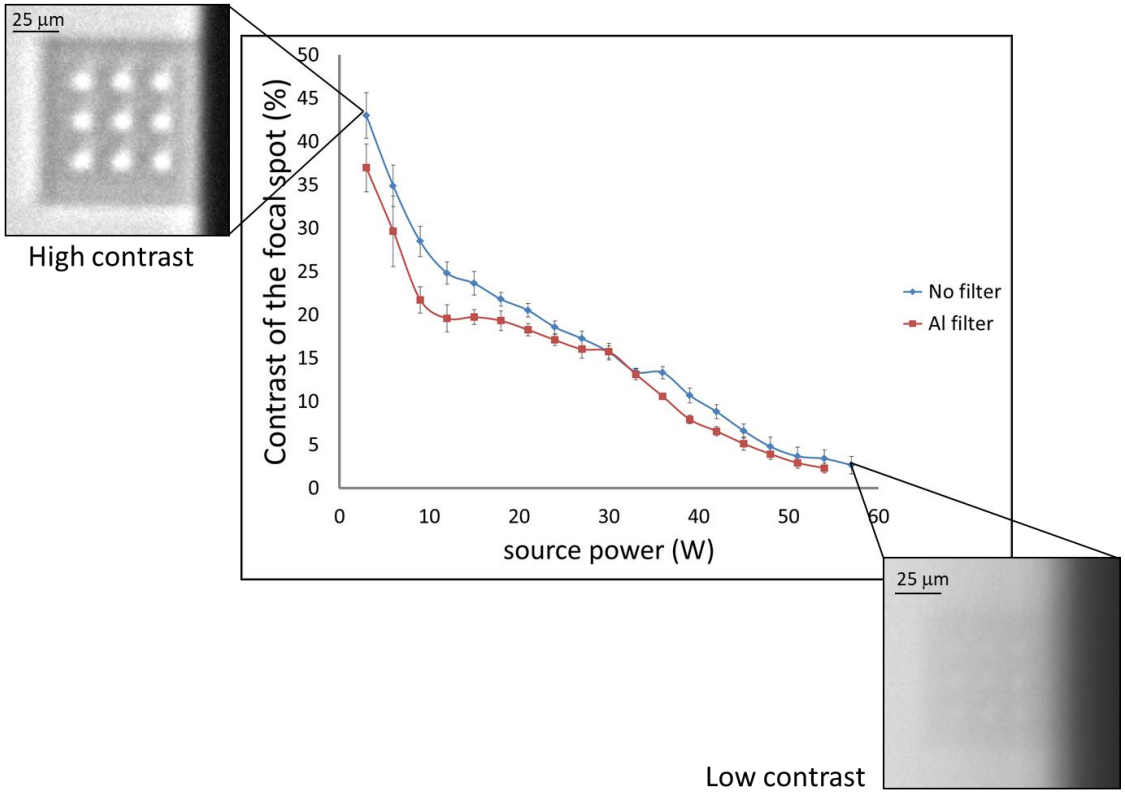

Figure 65. *The contrast of the focal spot decreases with increasing power output of the source.*

3.7. Imaging gold wires in a mesh

We used an experimental x-ray microscopy set up as illustrated in Figure 66 using the nano printed x-ray polymer lens as the magnifying lens. The imaged sample was a 200 µm period mesh of gold wires mounted on an Al holder. The x-ray source is a fixed-anode, tungsten-target micro focus tube (Oxford UltraBright) operating at 45 kV/ 3W. An indirect flat panel

radiography detector with a pixel size of 83 µm (PaxScan 3024M, Varian, CA, USA) was used to image the grating. The geometric distances were L_1 = 20 mm from the source to the sample, $L_2 - L_1$= 21 mm from the sample to the lens, and $L_3 - L_2$ = 1640 mm from the lens to the detector.

Due to the small size of the x-ray tube focal spot, only an area of about 7x7 µm is illuminated within the field of view of a CRL. Consequently, only an edge of a wire becomes visible when it enters that area of a CRL.

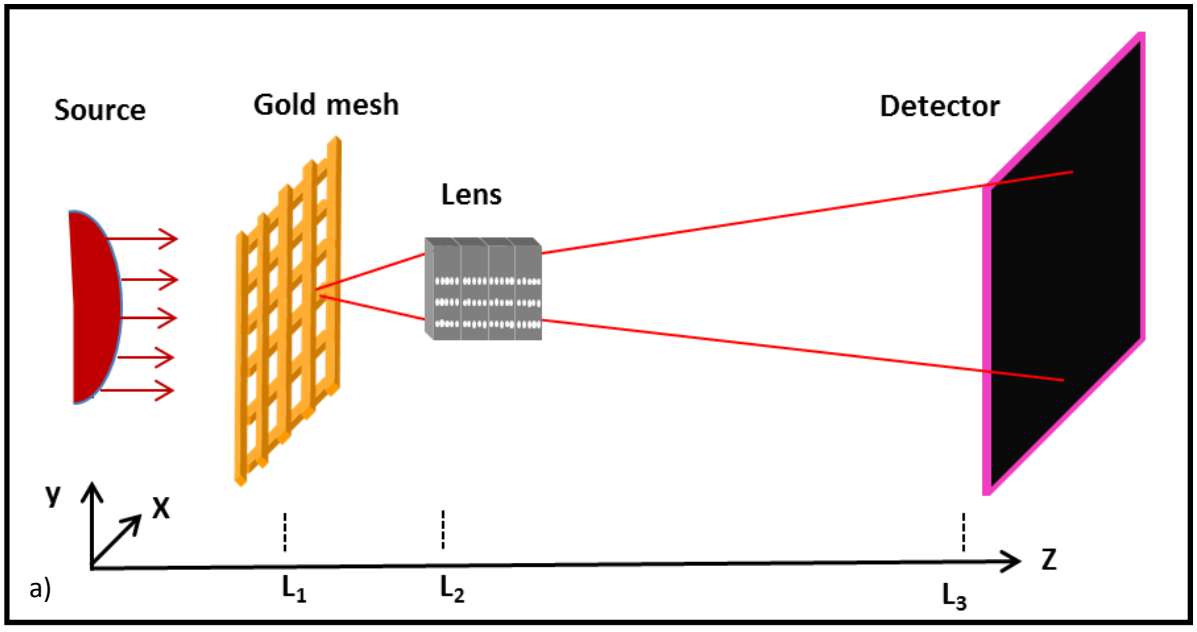

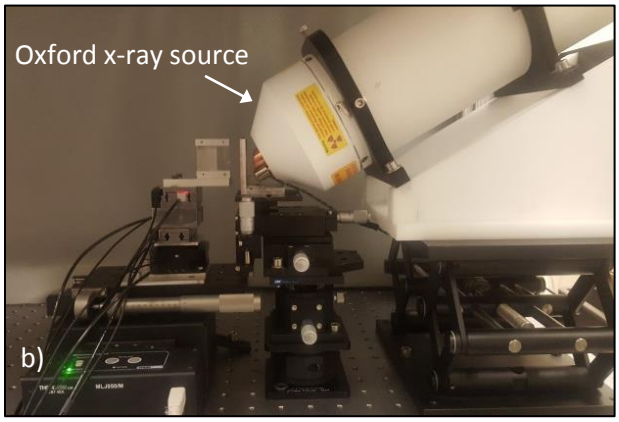

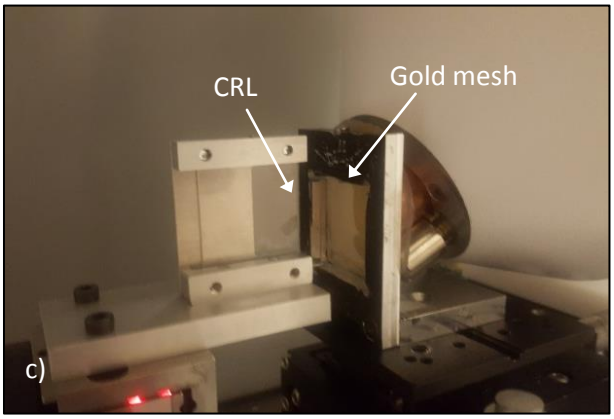

Figure 66. *Setup of the imaging experiment of a 200 µm-period mesh of gold wires. (a) The wire mesh is illuminated by an x-ray tube. The transmission image through the mesh is magnified by each of the 9 parallel CRLs. (b) In this photograph of the imaging setup, the silica substrate of the CRL was mounted vertically on the motorized stage. (c) A closer view of the gold mesh mounted on a holder and the silica substrate.*

The results showed that the CRL provides a magnified view of the edges of the gold wires as they passing through the illuminated areas. Figure 67a shows that the wire edges are highly blurred outside the CRLs. One horizontal wire edge falls within the view of the top row of CRLs and appears sharp due to the 80x magnification. Figure 67b to 72g shows a horizontal wire edge being captured by different rows of CRLs as the mesh was moved downward over a distance of about 50 µm.

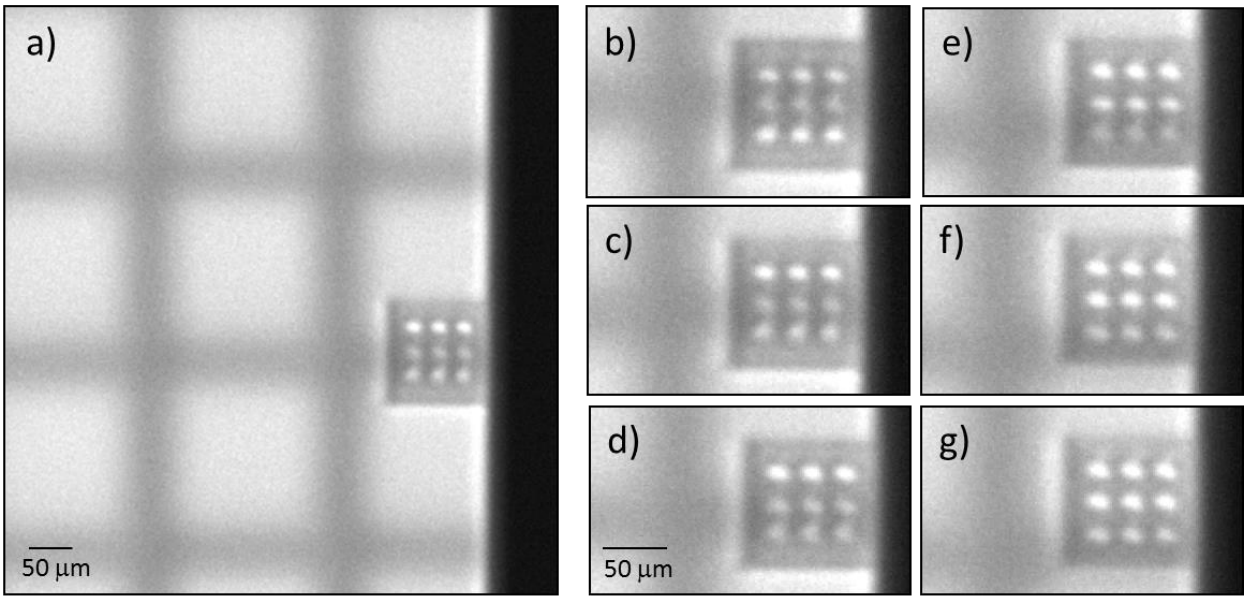

Figure 67*. Magnified views of a horizontal edge of a gold wire as it passes through the views of the three rows of CRLs. a) The edge falls in the view of the top row of 3 CRLs. b) to g) the edge moves downward from the views of the top row to the views of the bottom row of the CRLs.*

3.8. Conclusion

Through iterative design and protocol optimization, this work demonstrates that 3D printing at sub-micrometer resolution using two-photon photopolymerization can produce miniature compound refractive lenses for hard x-rays. The fabricated CRL has the smallest size and shortest focal length that has been reported in the literature for operation with photons in the range of 10s of keV. The CRL was also able to maintain focusing over a range of x-ray tube voltages from 25 kV to 85 kV, and enabled benchtop imaging and analysis of the focal spots of tungsten-anode x-ray tubes at 74x magnification. The standard method for direct imaging of x-ray tube focal spots is by pinhole cameras, where the size of the pinhole is also the image resolution if diffraction effect is negligible. Therefore, to obtain the same pixel resolution as in this study, the pinhole would require a diameter of approximately 1.1 μm, resulting in a flux through the pinhole that is two orders of magnitude lower than the flux through the current CRL. Correspondingly, the exposure time to obtain the same level of image intensity would be about 100 times greater than the present CRL, or 10 min long. Therefore, the CRL provides the ability to measure focal spot drifts on the time scale of seconds, which would otherwise appear as an artefactual spot elongation in an exposure of minutes.

Chapter 4. Nanoscale gratings

4.1. Introduction

High quality x-ray gratings are essential components in compact phase contrast imaging systems. One of the major factors in grating interferometry is that the grating period is required to be comparable to the transverse coherence of the x-ray beam, in order to produce wave interference effects. The transverse coherence at a point in the beam is the x-ray wavelength divided by the angular spread of the incoming x-rays that pass through that point. Without using absorption gratings, the transverse coherence lengths of the common X-ray tubes are in the range of 1 μm or less within a 0.5 m distance. Therefore, nano scale phase gratings are needed. Moreover, a phase grating needs to produce a sufficient phase modulation in the beam in order to split the beam. In an example of gold-filled silicon gratings of 0.5 μm period, to produce a π-phase shift for 25-100 keV x-rays in a binary grating which leads to the maximum diffraction efficiency, a gold height between 5.8-23.4 μm is required. Defining the grating aspect ratio as the ratio between the trench depth and half period of the grating, this implies that an aspect ratio in the range of 23-93 is necessary.[7]

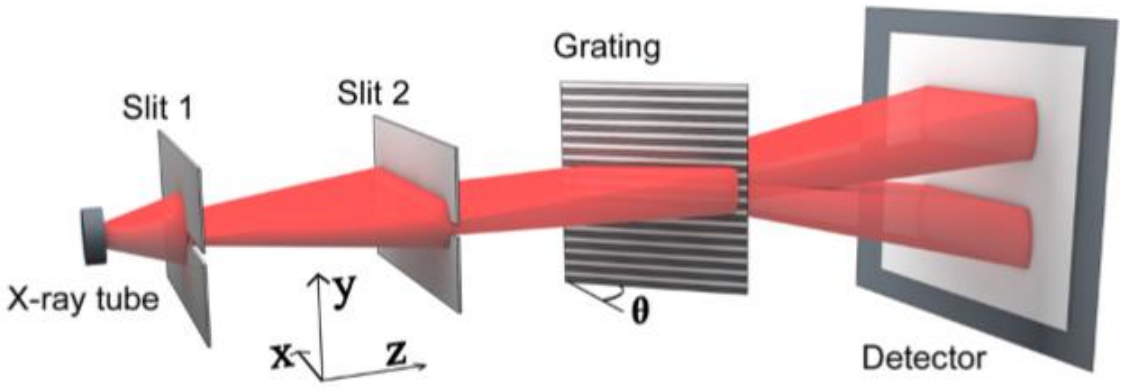

Figure 68. *The x-ray diffraction setup. The x-ray cone beam is collimated by two slits and diffracted by the grating and captured on an X-ray detector*[46].

4.2. Introduction to silicon grating fabrication methods

The fabrication process is challenging, since the process is a combination of fabricating silicon or polymer gratings with small periods and high aspect ratios and filling the trenches with high atomic number metals. Different fabrication methods have been extensively investigated for the realization of high aspect ratio Si gratings utilizing wet and two dry processes.

4.2.1. Wet etch processes

Anisotropic wet etch with KOH with the <110> wafers and metal assisted chemical etch are two main techniques for the wet process.

4.2.1.1 Anisotropic etch with KOH:

Wet etch process with KOH solution obtains the high aspect ratio Si trench based on the difference between the Si etch rate in different Si planes. The difference between density of Si and bonding energy of planes defines their oxidation and etch rate. Since both oxidation and etch rates occur simultaneously while Si is in deep KOH solution, the final aspect ratio is strongly dependent to the difference between the oxidation and etch rate of the particular plane. It's been shown that an aspect ratio of hundred to one can be achieved on {110} surface, while that amount is significantly lower in {111} plane. That happens because of high oxidation rate of {111} plane in KOH solution[47,48,49].

Even though using wet etch process can give aspect ratio as high as 600, this technique is strongly dependent to the fabrication mask and has limited surface area due to Si's slanted planes[47,50].

4.2.1.2 Metal assisted chemical etch (MACE)

In a Metal assisted chemical etch (MACE) process, a substrate (typically Si) is covered by a noble metal and is exposed to an etchant consisting of HF and oxidation agent. It was first introduced in 1997[51], that parts of Si wafer that was covered by Al, got etched faster in the solution of HF, HNO_3 and H_2O. Bohn-Li[52] pushed this technique to a higher level using noble metal such as Au, Pt in the solution of HF, H_2O_2 and Ethanol. Metal acts as a catalyst and increase the hole injection into the Si and drastically increase the porous formation time[53]. Using this process high aspect ratio Si structures were produced, however despite the aspect ratio of 66 for 200 nm pitch grating structures, this process is extremely dependent to the geometry and morphology of the pattern and the support structure in the metal mask[54].

4.2.2 Dry etch processes

Several dry etch processes based on deep reactive-ion etching (DRIE) are capable of fabricating deep and high aspect ratio features in single crystal silicon, with the most prominent technologies being the cryogenic and Bosch DRIE process. The cryogenic DRIE (deep reactive ion etching) process utilizes SF_6 and O_2 gas to generate a passivation layer of SiO_xF_y to protect the sidewall from unwanted lateral etching. The process is performed at low temperature, typically around −110 °C (163K), which slows down the chemical reaction and leads to highly vertical sidewalls. However, proper study on the masking material is needed to minimize the undercut.[48]. It's been shown that Sio_2 and Cr hard masks create significant undercuts that limits the aspect ratio. The only mask that can withstand the cryogenic process is Cr-on-photoresist that despite the complicated fabrication process, still creates noticeable undercut[55]. Similar to the cryogenic process, the Bosch process consists of two process steps, namely side wall passivation and Si etching. On each cycle, a passivation layer of C_4F_8 is first deposited to protect the sidewall from

ion interactions, allowing SF_6 ions to bombard the substrate and etch the substrate anisotropically during the etch step (Figure 69). The Bosch process ensures a highly directional etch. However, intrinsic scallops on the sidewall are one of the common issues in this process due to the sequential passivate/etch cycles. These scallops can be minimized by optimizing the etch parameters, particularly the relative times for the passivation and etching steps.[56]

The Bosch process has been utilized to etch 200 nm-pitch gratings to 4 and 6 μm in depth (aspect ratio of 40 and 60), but with supporting structures to the grating walls that reduce the efficiency of the gratings[50,57].

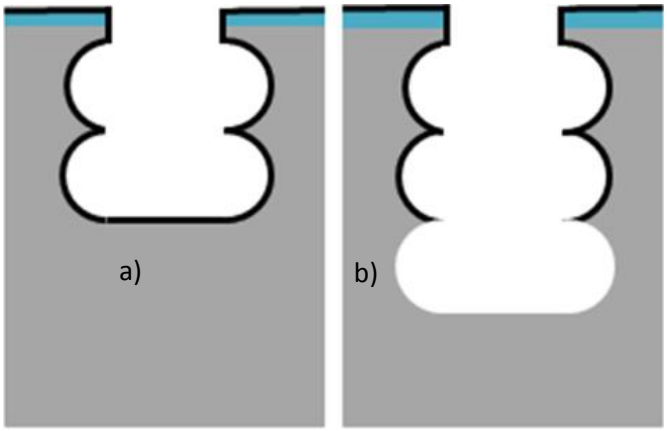

Figure 69. *Bosch DRIE schematic. a) Passivation of the sidewall with C_4F_8 deposition b) Anisotropic Si etch with SF_6.*

4.3. Fabrication of high-aspect ratio silicon gratings

In comparison with the isolated narrow lines or trenches, one of the major difficulties of the DRIE fabrication process is to maintain the mechanical stability of the narrow wall/trench structure of the gratings. The undercut or negative taper can damage the walls so that the charging effect leads to the general collapse in the arrayed walls. Therefore, carefully tuned and

optimized parameters are necessary to control the etch speed, selectivity, and the grating's profile.

This section describes the development of a Bosch process capable of producing 400 nm period gratings of near 10 μm trench depths, reaching a maximum aspect ratio of 50:1.

4.3.1 Fabrication procedure

The deep silicon etching was performed using Bosch process with silicon dioxide as mask material. The fabrication process is briefly described below. A 300 nm thick silicon dioxide layer was first grown on a silicon wafer using wet oxidation. Then a 30 nm chromium layer was coated via electron beam evaporation. The grating pattern was transferred from a master template to the wafer using nanoimprint lithography. The residue of the nanoimprint resist in the grating trenches was removed by oxygen plasma. Masked by resist, chromium was etched via ion milling. Taking advantage of the high selectivity over chromium, the silicon dioxide layer was reactive ion etched through using a CHF_3/O_2 recipe. The residual chromium was finally stripped in chrome etchant to form the silicon dioxide grating mask. With the protection of silicon dioxide, high aspect ratio silicon etch was carried out with a Bosch process at 5 °C, where each cycle consists of one C_4F_8 passivation step for 1.6 sec and two SF_6 etch steps for 1 sec each. An etching depth of 10 μm was achieved after 150 cycles of etching, corresponding to an aspect ratio of 50 (Figure 70).

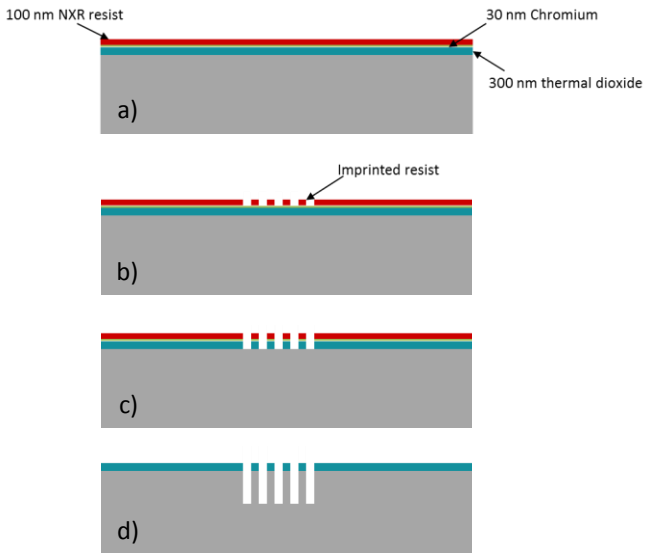

Figure 70. *Schematic of the fabrication process for 400 nm period hard X-ray phase gratings a) Grow thermal oxide layer on silicon wafer, deposit a thin layer of Cr and spin coat NXR resist b) Pattern resist using Nanoimprint c) Pattern silicon dioxide using Plasma etch d) Pattern silicon dioxide using Plasma etch.*

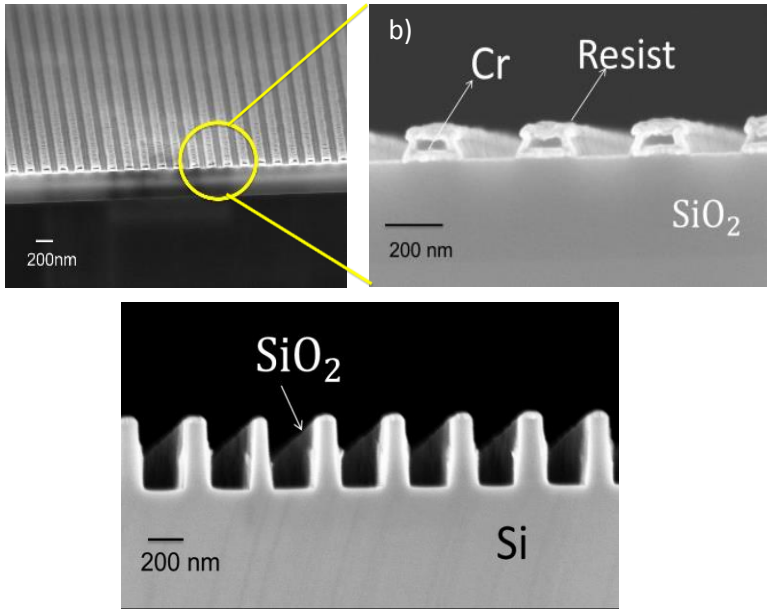

Figure 71. *Illustration of the fabrication processes for 400 nm period SiO_2 a) Patterning Cr mask using ion milling technique. c) Pattern Silicon dioxide using Plasma etch.*

The Bosch process was carried out on an inductively coupled plasma (ICP) etching system, SPTS (Omega c2L Rapier Deep Silicon Etcher) (Figure 72). The 7cm x 1cm samples were cleaved into 1 cm × 1 cm squares to investigate the etching parameters. After determining the proper parameter, a 1cm x 3cm was tested and showed a similar etch rate. In order to guarantee the reliable heat dissipation, pump oil was used to bond the sample to the silicon wafer. The etching results were characterized by scanning electron microscopy imaging.

Figure 72. *An inductively coupled plasma (ICP) etching system, SPTS Omega c2L Rapier Deep Silicon Etcher.*

The process has been done with two major approaches; Increasing the frequency to reduce the scallops and protecting the passivation layer with lowest notching possible using pressure, temperature and time ratio adjustment.

Moreover, the ratio between etch and deposition step had to be studied. The etch process was conducted using a three-pulsed recipes with a different pressure in depassivation and Si etch step.

Experiment started with the baseline recipe. The Bosch process started at 10 °C for 180 cycles. Each cycle consists of one C_4F_8 passivation step with chamber pressure of 40 mTorr and gas pressure of 325 sccm for 1 sec and two SF_6 etch steps with chamber pressure of 23 mTorr and 29 mTorr and gas pressure of 375 sccm and 375 sccm for 1.5 sec and 1.9 sec. An etching depth of 6.8 μm was achieved. However, gratings collapsed when the loop cycles increased to 270, showing that the passivation layer was not enough (Figure 73).

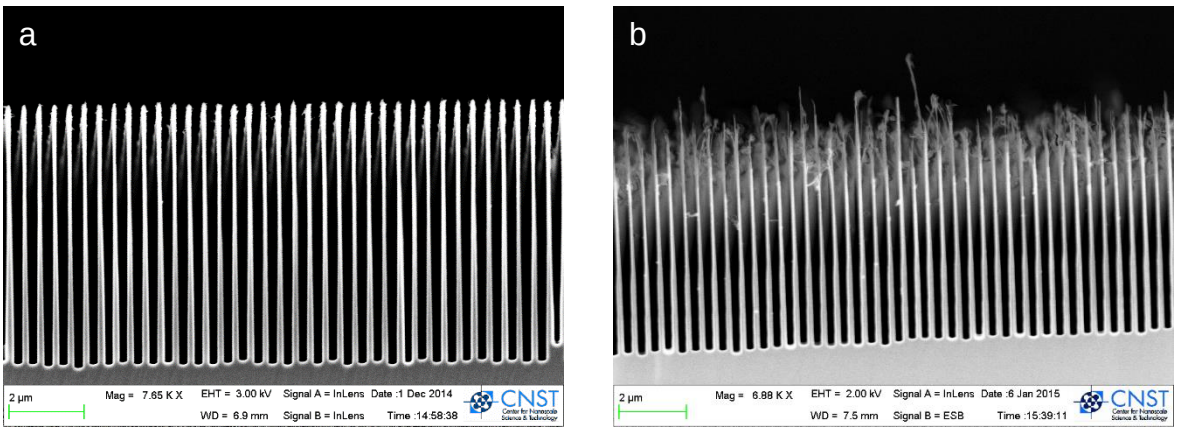

Figure 73. *High aspect ratio Si grating with baseline Bosch process recipe a) 180 loops b) 270 loops*

To address this problem, the passivation time was increased to improve the fluorocarbon film thickness. Meanwhile, the etch step was also needed to be tuned down to become less aggressive. The etch step slowed down by increasing the chamber pressure and decreasing the etch time in Si etch step while the pressure in depassivation step was kept intact. Increasing the pressure will lead to a higher mean free path of the plasma ion and lower etch rate. The etch result showed that the etch step was still too aggressive so that fluorocarbon layer couldn't resist and the gratings

completely collapsed (Figure 74b). The next step was to increase the passivation time, however it could be observed this amount of passivation time could not protect the walls. The undercut generated in the aggressive depassivation step provides room for isotropic etch and lead to the failure in the Si etch step. The Si was etched down to 10 μm, but the grating walls were damaged due to the poor protection of the sidewalls ((Figure 74c). By reducing the passivation time by 0.2 sec, the optimum recipe was achieved and the profile survived 150 cycles down to 10 μm. ((Figure 74d)

A brief summary of the recipes that were studied in this study are shown in table 2.

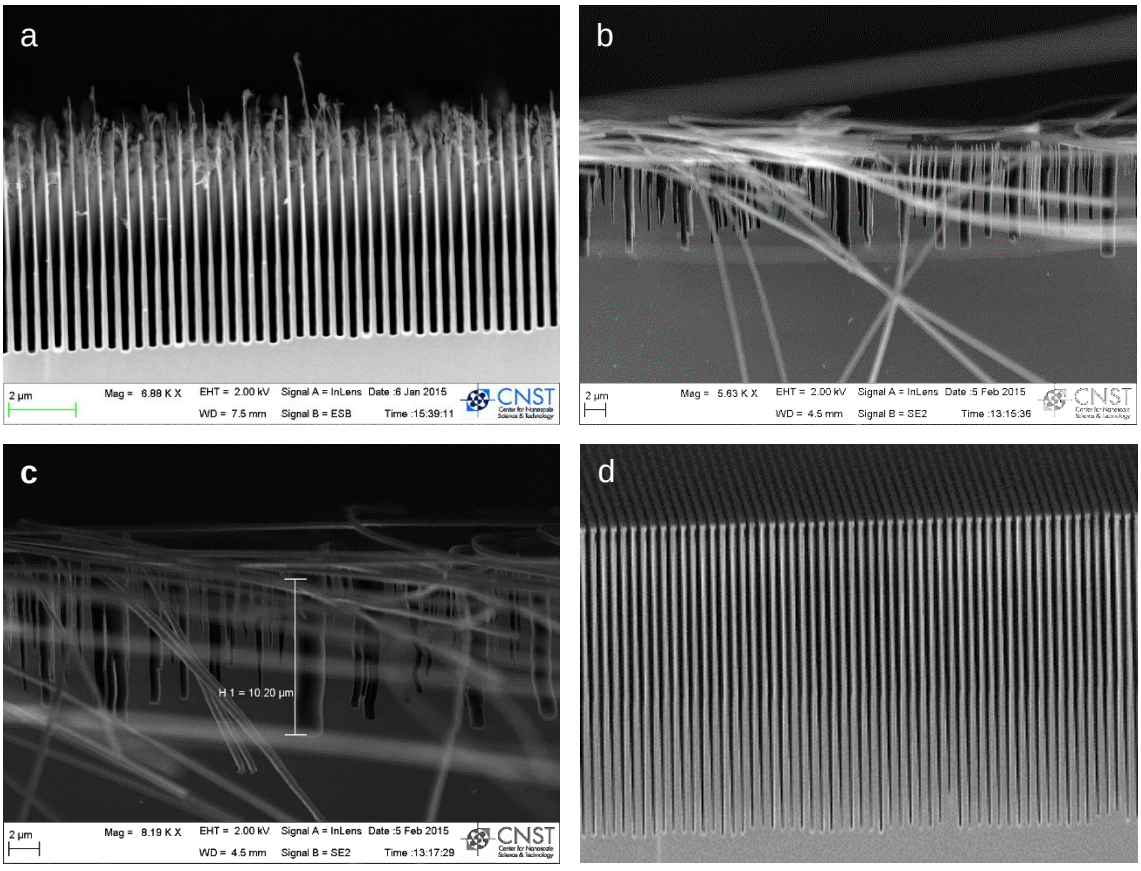

Figure 74. *With the protection of silicon dioxide, high aspect ratio silicon etch was carried out with a Bosch process at 5 °C, where each cycle consists of C_4F_8 passivation step and SF_6 etch step with a*

specific time each. The ratio and duration of etch and passivation time (E/D) have a noticeable influence on the etch profile. Lowering the E/D and tuning the deposition and etch time, provided the desired profile. The effect of low passivation time, causes the grating walls to get etched during the etch steps. a) E/D=3.4, low passivation time, b) E/D=2.2, low passivation time, c) E/D=1.375, high etch time, d) E/D=1.25 desired recipe.

4.3.2 Optimization of the fabrication parameters

Increasing the frequency will reduce the scallops at the sidewall. Trend of the time in the process, showed that the general etch vs deposition time ratio was reduced gradually toward the end of the process. That was one of the major factors considered during the characterization, to improve the profile and reduce the sidewall roughness.

Table 2. Summary of the selected Bosch process recipe

Loop #	Temp	Deposition		etch 1		etch 2		Ratio	Etch depth (um)	Profile
		Pressure (mtorr)	time	pressure (mtorr)	time	pressure (mtorr)	time	(etch/Dep time)		
180	10	40	1	23	1.2	29	1.2	2.4	6.8	Good
180	10	40	1	75	1.5	23	1.9	3.4	6.8	Good
270	10	40	1	75	1.5	23	1.9	3.4	-	Collapsed
180	10	40	1	75	1.2	23	1	2.2	6.8	Bad
270	10	40	1	75	1.2	23	1	2.2	-	Collapsed
90	5	45	1.4	25	1.2	40	1	1.57	-	Collapsed
90	5	45	1.6	25	1.2	45	1	1.375	-	Collapsed
90	5	45	1.6	25	1	40	1	1.25	6.159	Good
115	5	45	1.6	25	1	40	1	1.25	7.164	Good
135	5	45	1.6	25	1	40	1	1.25	8.282	Good
150	5	45	1.6	25	1	40	1	1.25	10.27	Good (etch stopped)
175	5	45	1.6	25	1	40	1	1.25	10.27	

Temperature was another parameter that had a significant effect on the etch profile. Reducing temperature results in an increase in the film deposition rate. Increasing the passivation layer prevented the further undercut in the etch step. In this experiment, temperature was reduced from 10 to 5 °C. Table 2 describes the value of the gas pressure and the source power. Source power was constant in all recipes and as mentioned above the only step that the gas pressure was

changed was to decrease the etch rate in the Si etch process. C_4F_8 pressure was kept constant during the experiment and its value was 325 sccm. SF_6 pressure was constant in depassvation step and its value was 375 sccm. However the SF_6 pressure at the Si etch step dropped to 340 sccm.

Table 3. Gas pressure and source power value

Gas	**Deposition**	**Etch1**	**Etch2**
C_4F_8 (sccm)	325	1	1
SF_6 (sccm)	1	375	340
Power source (W)	2500	2700	2700

4.3.3. Maximum etch depth

A robust repeatable process that provides the deepest trench in <200 nm size scale and the lowest undercut in stable narrow walls has been achieved by increasing the frequency and a precise study on the process parameters. However, the etch process stops at 10 μm depth, which is due to the positively tapered profile of the sidewall at the bottom of the trench. High deposition pressure and the polymer accumulation of the sidewall lead to a positively tapered profile[56]. Going beyond this depth is an area for the future studies Figure 75.

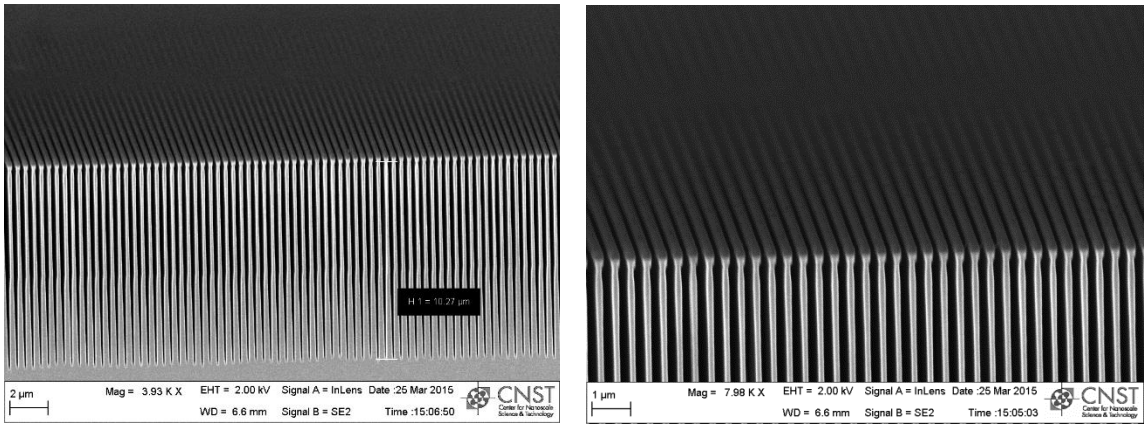

Figure 75. *Cross-sectional scanning electron microscopy images of etched silicon grating of 400 nm period with aspect ratio of 50 and the maximum etch depth of 10 µm.*

4.3. Electrodeposition of gold

Due to the high density and high refractive index of gold, it is widely used in optical components for x-ray imaging, such as phase gratings and zone plates.[58,59] Filling high aspect ratio trenches with conformal gold by electrodeposition is common for x-ray phase grating applications[60,61]. Successful filling of 200 nm period gratings with an aspect ratio of 30[62] and 400 nm gratings with an aspect ratio of 35 has been reported.[63] Here we push the limit up to the aspect ratio of 50 over the large area (1 cm x 7 cm) grating. The challenging issue regarding the large area grating is that when the metal fills the trench the surface area changes drastically with respect to the empty trenches, therefore overplating can happen in the fraction of minutes and close monitoring is needed to stop the plating when the gold fills the trench.

A conductive seed layer is needed on the grating surface, prior to plating. Having a thin layer of platinum, electrodeposition occurs when the electron transfers from the grating substrate to split the $Au(CN)^{2-}$ ionic complex and release the solid gold to be coated on the substrate. It's done in

Auruna 556 electrolyte solution at a temperature of 50 °C and a direct current density of 0.0175 mA/cm^2.

In this experiment, the conformal electroplating of a high aspect ratio grating was investigated while pulsed voltage was applied to the surface with pre-determined duty cycle and length. Scanning electron microscopy (SEM) and x-ray studies was used to investigate the quality of the plated samples (Figure 76).

The conformal plating starts from the platinum plated by the ALD. The bottom fills up conformally, but before the trench fills up properly, the top opening closes and the plating tends to be stopped. The reason is the scallops on the sidewall that was created during the Bosch process. On the top side of the trench, the scallops are deeper since they had been exposed to the more number of passivation and etch steps. Therefore the same thickness of platinum cannot fill the trench before the opening closes. Also the scallops can create undercut underneath the mask and make it negatively tapered (Figure 76 b-c).

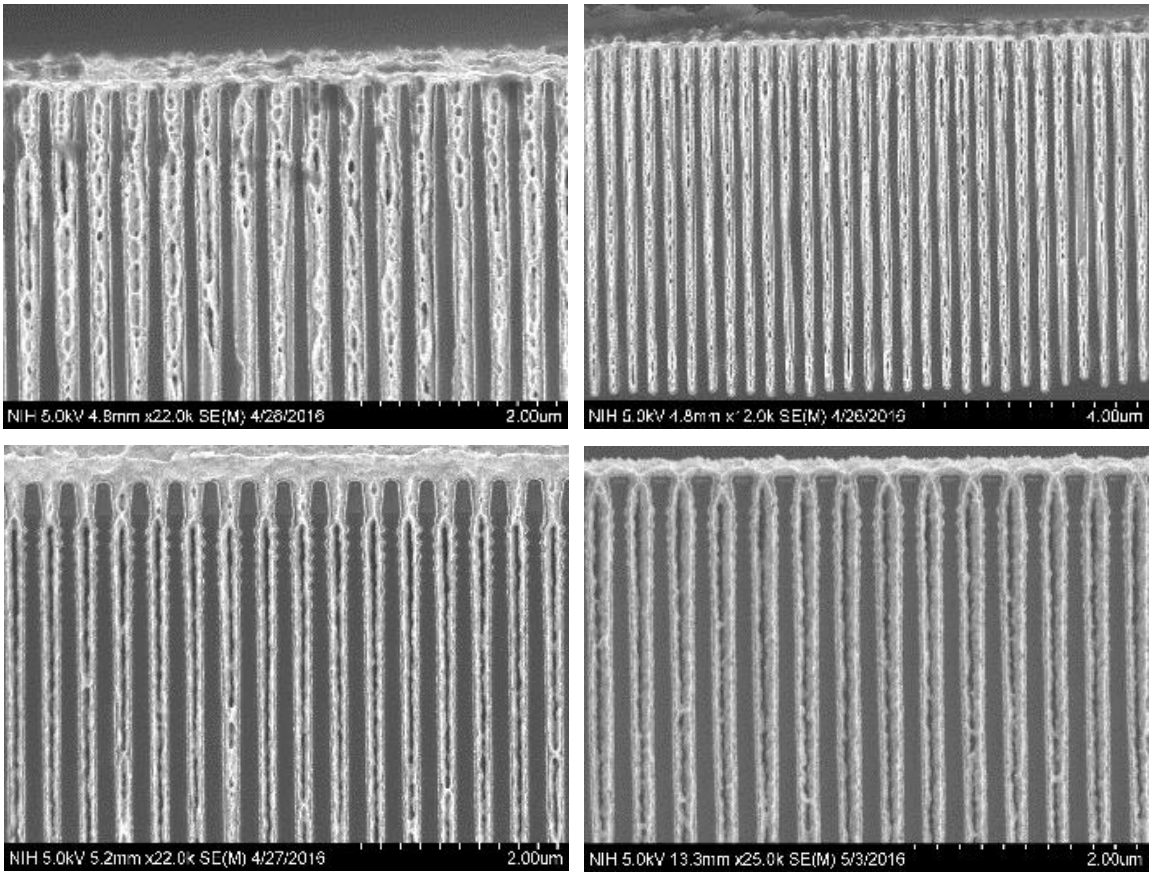

Figure 76. *Cross-sectional scanning electron microscopy images of a) electroplated silicon grating of 400 nm period and 6.8 μm depth b) opening positively tapered c) semi plated 7.2 μm deep grating due to the undercut caused by the Bosch process d) semi plated 6.8 μm deep grating.*

Finally, in order to reduce the absorption and attenuation of the Si, the gratings are backside-thinned to 170 μm.

4.4. X-ray inspection of gratings

Diffraction analysis of the phase gratings was performed in a tabletop x-ray diffraction set up. The x-ray source is Oxford UB 960004 operating at several peak voltages ranging from 30 to 70 kV. In order to observe separate diffraction orders, a tungsten slit with 20 μm width was placed

0.66 m from the source to limit the height of the beam. The grating was placed at 8.5 cm from the slit with the x-ray camera located 0.83 m from the grating opposite the source.

Three Gaussian peaks that represent the ± 1 diffraction and zeroth un-diffracted orders are shown in Figure 77. The broad spectrum of the x-ray tube and the angular divergence of the x-ray beam define the width of the diffraction peaks.

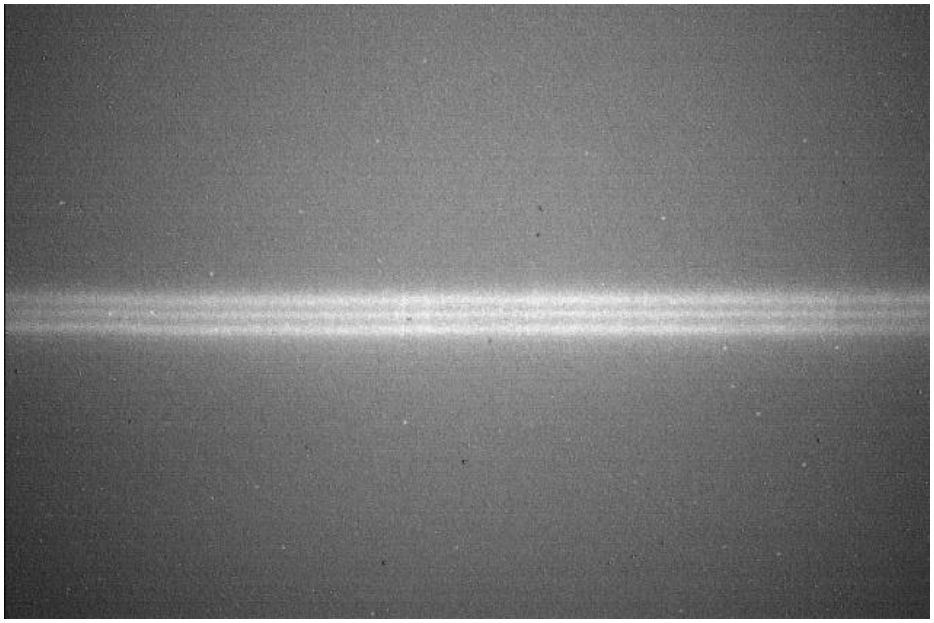

Figure 77. *Grating diffraction bands*

The normalized diffraction profiles at different x-ray tube voltage settings are plotted in Figure 78. The spectrum of the x-ray beam shifts to lower photon energies with lower voltage settings, which leads to a greater phase modulation and more energy being diffracted into the +/-1 orders. The diffraction angle, given by the ratio of wavelength over the grating period, increases with lower photon energies.

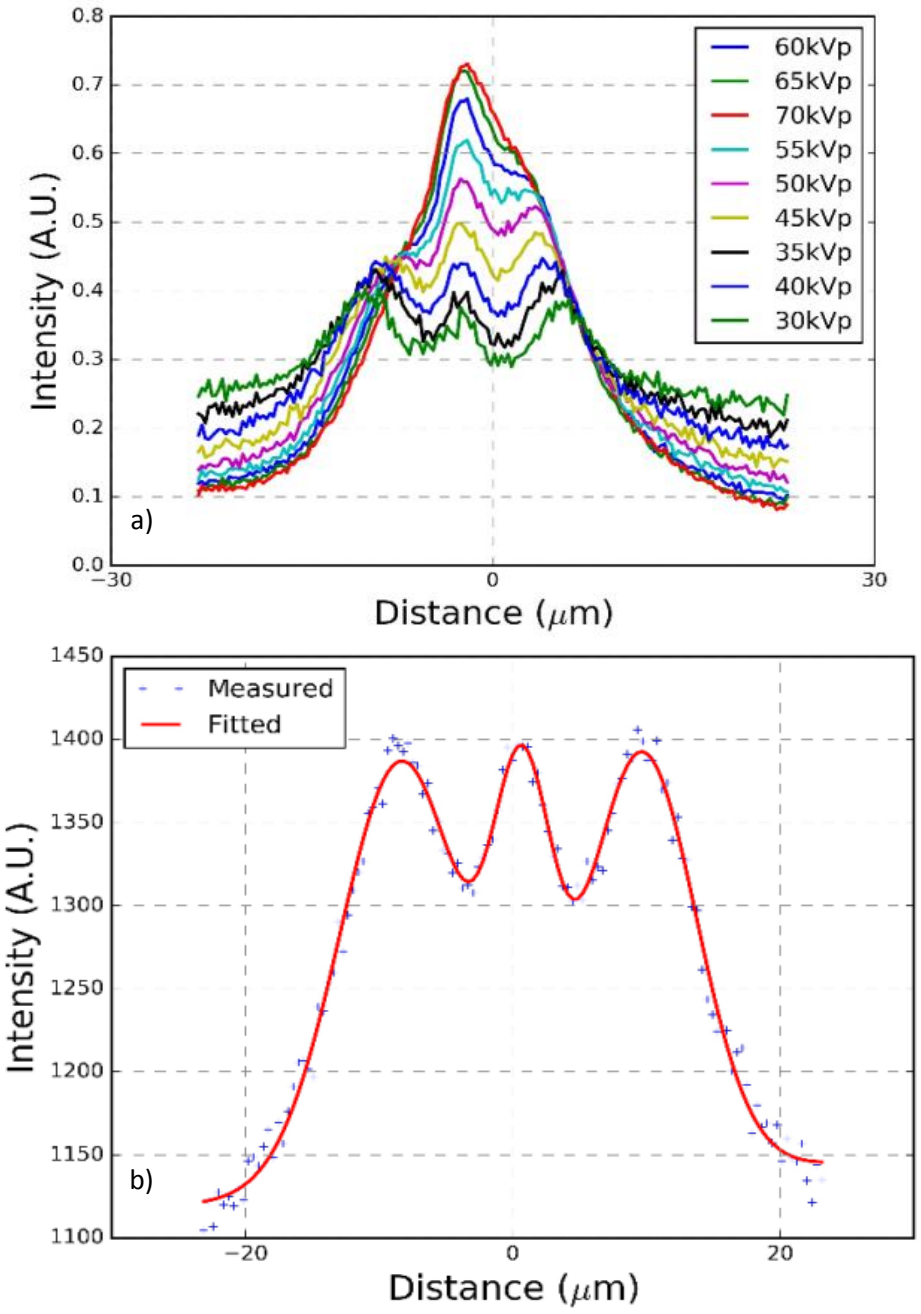

Figure 78. *X-ray diffraction test of a 400 nm period silicon-gold phase grating. a) Diffraction intensity at a range of x-ray tube kV settings. b) Gaussian peak fitting of the diffraction profile at 40 kV.*

4.5. Summary

In this chapter, a dry-etch fabrication process of 400 nm period silicon gratings was studied and the aspect ratio of 50 was obtained. This aspect ratio is higher than those achieved with wet-etching processes of metal assisted chemical etch and KOH etch when the grating walls are free standing. To-date, it is also the highest reported aspect-ratio in free-standing nanoscale gratings that we are aware of. Compared to previous cryo-etch fabrication of sub-micrometer period phase gratings[46], this process increased the aspect ratio by 40%, which raises the potential for applications at higher photon energies if conformal electroplating proves feasible in such deep trenches. A further discussion of future development is included in Chapter 5.

Chapter 5. Conclusion and future work

The presented dissertation research encompasses the fabrication and characterization of two types of x-ray optical elements to address current issues in focusing hard x-rays for microscopy and improving the sensitivity of phase-contrast imaging at high photon energies.

Focusing x-rays of photon energies above 10 keV is a particularly challenging task due to the fact that the refractive indices of all materials differ from vacuum by 10^{-5} or less, and scale inversely with the square of the photon energy, making them fairly ineffective in reflecting or refracting x-rays. The two methods to focus hard x-rays today are curved mirrors and compound refractive lenses. Both methods are used routinely in large-scale facilities such as synchrotron beamlines, but neither is well-suited for benchtop applications, since they are not able to focus hard x-rays to a sufficiently short focal length for compact systems. Miniature compound refractive lenses by high-resolution 3D printing is a nascent technology that holds promise to overcome the hurdle. The idea was independently proposed by my group and Snigirev's group. In 2017, Snigirev's team demonstrated a 3D printed polymer CRL capable of focusing soft x-rays to within 10 cm focal distance. My work is the first CRL capable of focusing hard x-rays to a focal length of 2 cm and less. With such a CRL, I was able to demonstrate benchtop hard x-ray imaging at 74 times magnification with a medical-grade flat panel detector. Generally, compact microscopy systems in the hard x-ray regime have relied on projection magnification, which cannot be used to evaluate light emitting objects such as the focal spot of x-ray tubes. The system I developed is shown to fill this un-met need, and is substantially faster than the traditional pin-hole imaging method.

My work of miniature polymer CRLs by direct 3D nanoprinting using two-photon polymerization included several iterations of designs and printing protocols. Two different approaches to achieve focusing in both directions of the transverse plane were tried. The first was an inline arrangement of a pair of perpendicular cylindrically focusing CRLs, the second was a CRL consisting of spherically focusing lens elements. The second approach was superior, and two design iterations of spherically focusing lenses were tested. The elongated bi-concave lens design with open parabolic surfaces proved successful and produced the final CRL for benchtop imaging tests.

With the 3D-printed miniature CRLs, I envision for the future an x-ray microscope of a focusing pin-hole design (Figure 79), which can collect orders of magnitude the amount of light of a pin-hole camera of the same resolution, and at the same time retain the ability to image both passive and light-emitting objects. It consists of circular apertures at both ends of the CRL that match the size of the lens elements to eliminate background light that bypasses the CRL, coupled to an efficient flat-panel x-ray detector. The system will rely on the short focal length and the resulting high magnification factor to achieve spatial resolution, without requiring high resolution detectors that compromise efficiency. The main engineering challenge to be anticipated in this system is the alignment and fixture of the apertures with the lens. Micrometer-scale apertures can now be drilled into tungsten sheets with laser beams. The substrate that holds the CRL can be modified to allow precise attachment of the apertures under x-ray imaging guidance.

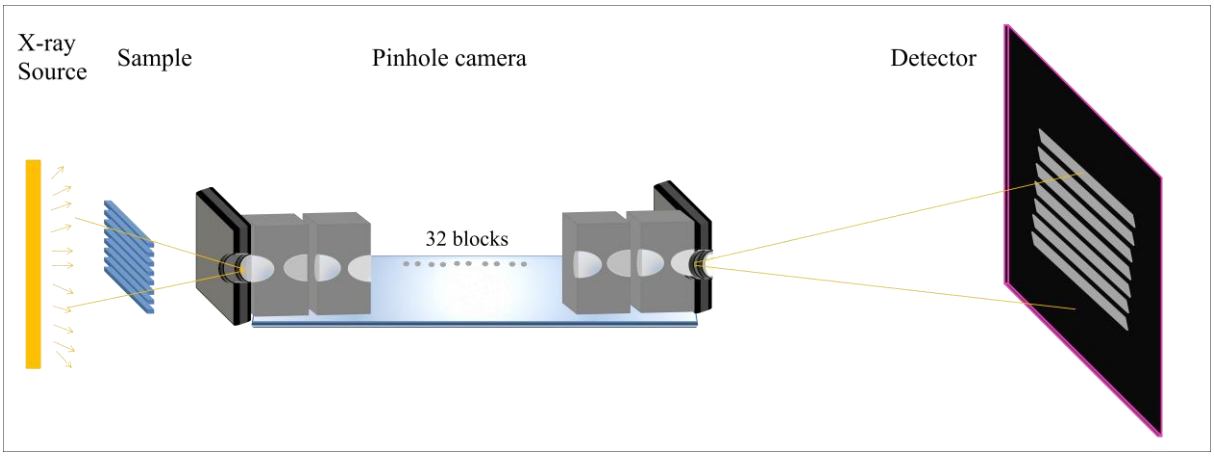

Figure 79. *Focusing-pinhole Microscope Design Based on the Nano-printed Micro CRL. Circular apertures are added to both ends of the CRL. The aperture diameters match that of the lenses in order to block light transmission that by-passes the CRL. The resulting microscope combines features of a pinhole camera with those of a lens-coupled microscope, which can be called a "focusing pinhole" microscope.*

The second part of my dissertation is focused on the fabrication of sub-micrometer period diffraction gratings for compact phase contrast imaging systems in the hard x-ray regime. Such systems are limited to conventional x-ray sources of broad spectral bandwidths and finite focal spots. Gratings are the optical element of choice to split and combine such beams. With the advent of the phase moiré effect, it is now possible to achieve high sensitivity in such systems with nanometric phase gratings. Again, due to the low refraction of x-rays by materials, the gratings need to have deep trenches that are filled with high-atomic number materials to cause sufficient phase modulation of the beam.

Prior to my work, a cryo-etch technique had been developed to produce 400 nm period silicon grating molds with up to 5 μm free-standing walls[46]. However, it could not go beyond this height. I developed an alternative dry-etch fabrication process that extended the trench depth to approximately 10 μm, corresponding to a maximum aspect ratio of 50, while retaining the free-

standing structure. This aspect ratio is higher than those achieved with wet-etching processes of metal assisted chemical etch and KOH etch when the grating walls are free standing. To-date, it is also the highest reported aspect-ratio in free-standing nanoscale gratings that we are aware of. A critical step of this process was creating the mask pattern for etching. A two-step procedure was developed to produce a dual layer mask that proved effective for the deep dry etch.

The value of the extended grating depth is that it allows phase contrast imaging at higher x-ray photon energies in thicker or denser objects, provided that the deep trenches can be filled by a heavy element. Although gold is the most commonly used element, I explored rhodium as an alternative to gold for several reasons: rhodium is more economical and sufficiently dense to cause significant phase shifts at high photon energies; rhodium plating is commonly performed in small-scale jewelry production and the plating solution is non-toxic and safe. My preliminary tests have created smooth rhodium layers on silicon substrates (Figure 80). The plating starts from a platinum seed layer on a silicon substrate. A 60 nm thick layer of rhodium was deposited over 1 minute of DC plating. In the future, conformal electroplating of high aspect-ratio gratings needs to be investigated to produce the final diffraction gratings for high energy x-rays.

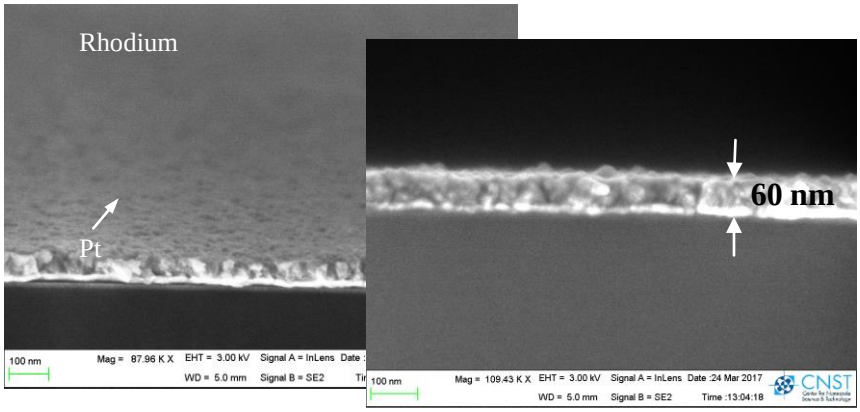

Figure 80. *Electroplated rhodium layers of 60 nm thickness on silicon substrates*

Publications

- M. Mirzaeimoghri, A. Morales, A. Panna, E. Bennet, D. DeVoe , H. Wen, "Nanoprinted Miniature Compound Refractive Lens for Desktop Hard X-Ray Microscopy", submitted.

- Miao Houxun, Lei Chen, Mona Mirzaeimoghri, Richard Kasica, and Han Wen. "Cryogenic Etching of High Aspect Ratio 400-nm Pitch Silicon Gratings." Journal of microelectromechanical systems: a joint IEEE and ASME publication on microstructures, microactuators, microsensors, and microsystems 25, no. 5 (2016): 963.

- M. Mirzaeimoghri, O. Barham, D. DeVoe "Millimeter Scale, Radial-Mode Bulk Piezoelectric Transformers Fabricated by Micro-Powder Blasting", to be submitted.

References

1. Röntgen, W. C. On a new kind of rays. *Science (80-.).* **3,** 274–277 (1896).

2. Brenner, D. J. & Hall, E. J. Computed tomography--an increasing source of radiation exposure. *N. Engl. J. Med.* **357,** 2277–2284 (2007).

3. Michelson, A. A. & Morley, E. W. On the relative motion of the Earth and the luminiferous ether. *Am. J. Sci.* **s3-34,** 333–345 (1887).

4. Born, M. & Wolf, E. *Principles of optics : electromagnetic theory of propagation, interference and diffraction of light*. (Pergamon Press, 1980).

5. Bonse, U. & Hart, M. AN X-RAY INTERFEROMETER. *Appl. Phys. Lett.* **6,** 155 (1965).

6. Clauser, J. F. Ultrahigh resolution interferometric x-ray imaging. (1997). doi:US 5812629 A

7. Miao, H., Gomella, A. A., Chedid, N., Chen, L. & Wen, H. Fabrication of 200 nm period hard X-ray phase gratings. *Nano Lett.* **14,** 3453–3458 (2014).

8. Wen, H. *et al.* Boosting phase contrast with a grating Bonse-Hart interferometer of 200 nanometre grating period. *Philos. Trans. A. Math. Phys. Eng. Sci.* **372,** 20130028 (2014).

9. Miao, H. *et al.* A universal moiré effect and application in X-ray phase-contrast imaging. *Nat. Phys.* **12,** 830–834 (2016).

10. Sakdinawat, A. & Attwood, D. Nanoscale X-ray imaging. *Nat. Photonics* **4,** 840–848 (2010).

11. Kang, H. C. *et al.* Nanometer linear focusing of hard X rays by a multilayer laue lens. *Phys. Rev. Lett.* **96,** (2006).

12. Snigirev, A., Kohn, V., Snigireva, I. & Lengeler, B. A compound refractive lens for focusing high-energy X-rays. *Nature* **384,** 49–51 (1996).

13. Miao, J., Charalambous, P., Kirz, J. & Sayre, D. Extending the methodology of X-ray crystallography to allow imaging of micrometre-sized non-crystalline specimens. *Nature* **400,** 342–344 (1999).

14. Denk, W., Strickler, J. H. & Webb, W. W. 2-Photon Laser Scanning Fluorescence Microscopy. *Science (80-.).* **248,** 73–76 (1990).

15. Barinov, A. *et al.* Synchrotron-based photoelectron microscopy. *Nucl. Instruments Methods Phys. Res. Sect. A Accel. Spectrometers, Detect. Assoc. Equip.* **601,** 195–202 (2009).

16. Donoghue, P. C. J. *et al.* Synchrotron X-ray tomographic microscopy of fossil embryos. *Nature* **442,** 680–683 (2006).

17. Jach, T. *et al.* Wide-field x-ray microscopy with Kirkpatrick-Baez optics. in (ed. McNulty, I.) **4499,** 38–44 (International Society for Optics and Photonics, 2001).

18. Gary, C. K. *et al.* High resolution x-ray microscope. *Appl. Phys. Lett.* **90,** (2007).

19. Lengeler, B. *et al.* Refractive x-ray lenses. *J. Phys. D. Appl. Phys.* **38,** (2005).

20. Dudchik, Y. I. *et al.* Using of a microcapillary refractive X-ray lens for focusing and imaging. *Spectrochim. Acta - Part B At. Spectrosc.* **62,** 598–602 (2007).

21. Aristov, V. *et al.* X-ray refractive planar lens with minimized absorption. *Appl. Phys. Lett.* **77,** 4058 (2000).

22. Schroer, C. G. *et al.* Beryllium parabolic refractive x-ray lenses. in (ed. Mancini, D. C.) 10 (International Society for Optics and Photonics, 2002). doi:10.1117/12.451013

23. Aristov, V. V. *et al.* X-ray focusing by planar parabolic refractive lenses made of silicon. *Opt. Commun.* **177,** 33–38 (2000).

24. Terentyev, S. *et al.* Linear parabolic single-crystal diamond refractive lenses for synchrotron X-ray sources. in *Journal of Synchrotron Radiation* **24,** 103–109 (2017).

25. Dudchik, Y. I. & Kolchevsky, N. N. A microcapillary lens for X-rays. *Nucl. Instruments Methods Phys. Res. Sect. A Accel. Spectrometers, Detect. Assoc. Equip.* **421,** 361–364 (1999).

26. Antipov, S. *et al.* Single-crystal diamond refractive lens for focusing X-rays in two dimensions. *J. Synchrotron Radiat.* **23,** 163–168 (2016).

27. Snigirev, A. *et al.* High energy X-ray nanofocusing by silicon planar lenses. in *Journal of Physics: Conference Series* **186,** (2009).

28. Nöhammer, B., Hoszowska, J., Freund, A. K. & David, C. Diamond planar refractive lenses for third- and fourth-generation X-ray sources. *J. Synchrotron Radiat.* **10,** 168–171 (2003).

29. Schroer, C. G. *et al.* Hard X-ray nanoprobe based on refractive X-ray lenses. in *AIP Conference Proceedings* **879,** 1295–1298 (2007).

30. Etrov, A. K. P. *et al.* Polymer X-ray refractive nano-lenses fabricated by additive technology. **25,** 3256–3259 (2017).

31. Mimura, H. *et al.* Hard X-ray Diffraction-Limited Nanofocusing with Kirkpatrick-Baez Mirrors. *Jpn. J. Appl. Phys.* **44,** L539–L542 (2005).

32. Attwood, D. Soft X-rays and Extreme Ultraviolet Radiation. *Soft X-Rays Extrem. Ultrav. Radiat. Princ. Appl.* 504 (1999). doi:10.1017/CBO9781139164429

33. Boye, P. *et al.* Nanofocusing refractive X-ray lenses: Fabrication and modeling. *J. Phys. Conf. Ser.* **186,** 12063 (2009).

34. James, R. *The optical principles of the diffraction of x-rays*. (G. Bell & Sons, 1962).

35. Lengeler, B., Schroer, C. & Richwin, M. A microscope for hard x rays based on parabolic compound refractive lenses. *Appl. Phys.* (1999).

36. Nazmov, V. *et al.* LIGA fabrication of X-ray Nickel lenses. *Microsyst. Technol.* **11,** 292–297 (2005).

37. Vaughan, G., Wright, J. & Bytchkov, A. X-ray transfocators: focusing devices based on compound refractive lenses. *J. synchrotron* (2011).

38. Zozulya, A. V. *et al.* Microfocusing transfocator for 1D and 2D compound refractive lenses. *Opt. Express* **20,** 18967 (2012).

39. DHAMGAYE, V. P., TIWARI, M. K., SAWHNEY, K. J. S. & LODHA, G. S. Microfocussing of synchrotron X-rays using X-ray refractive lens developed at Indus-2 deep X-ray lithography beamline. *Pramana* **83,** 119–129 (2014).

40. Schroer, C. G. *et al.* Hard x-ray nanoprobe based on refractive x-ray lenses. *Appl. Phys. Lett.* **87,** 124103 (2005).

41. Krywka, C. *et al.* Polymer compound refractive lenses for hard X-ray nanofocusing. in **1764,** 20001 (AIP Publishing, 2016).

42. Nazmov, V. P., Reznikova, E. F., Somogyi, A., Mohr, J. & Saile, V. Planar sets of cross x-ray refractive lenses from SU-8 polymer. in (eds. Snigirev, A. A. & Mancini, D. C.) 235 (International Society for Optics and Photonics, 2004). doi:10.1117/12.562615

43. Perry, J. W. *et al.* Two-photon polymerization initiators for three-dimensional optical data storage and microfabrication. *Nature* **398,** 51–54 (1999).

44. Thiel, M., Ott, J., Radke, A., Kaschke, J. & Wegener, M. Dip-in depletion optical lithography of three-dimensional chiral polarizers. *Opt. Lett.* **38,** 4252–5 (2013).

45. ASDN - Nanotools - Two-photon Polymerization. Available at: http://asdn.net/asdn/nanotools/two-photon_polymerization.php. (Accessed: 18th December 2016)

46. Miao, H., Gomella, A. A., Chedid, N., Chen, L. & Wen, H. Fabrication of 200 nm Period Hard X-ray Phase Gratings. *Nano Lett.* **14,** 3453–3458 (2014).

47. Ahn, M., Heilmann, R. K. & Schattenburg, M. L. Fabrication of 200nm period blazed transmission gratings on silicon-on-insulator wafers. *J. Vac. Sci. Technol. B Microelectron. Nanom. Struct.* **26,** 2179–2182 (2008).

48. Wu, B., Kumar, A. & Pamarthy, S. High aspect ratio silicon etch: A review. *Journal of Applied Physics* **108,** (2010).

49. Ahn, M. & Heilmann, R. Fabrication of ultrahigh aspect ratio freestanding gratings on silicon-on-insulator wafers. *J. Vac. Sci.* (2007).

50. Mukherjee, P. *et al.* Plasma etch fabrication of 60:1 aspect ratio silicon nanogratings with 200 nm pitch. *J. Vac. Sci. Technol. B Microelectron. Nanom. Struct.* **28,** C6P70 (2010).

51. Dimova-Malinovska, D. & Sendova-Vassileva, M. Preparation of thin porous silicon layers by stain etching. *Thin Solid Films* (1997).

52. Li, X. & Bohn, P. Metal-assisted chemical etching in HF/H2O2 produces porous silicon. *Appl. Phys. Lett.* (2000).

53. Huang, Z., Geyer, N., Werner, P. & Boor, J. De. Metal- assisted chemical etching of silicon: a review. *Advanced* (2011).

54. Chang, C. & Sakdinawat, A. Ultra-high aspect ratio high-resolution nanofabrication for hard X-ray diffractive optics. *Nat. Commun.* **5,** 4243 (2014).

55. Miao, H., Chen, L., Mirzaeimoghri, M., Kasica, R. & Wen, H. Cryogenic Etching of High Aspect Ratio 400-nm Pitch Silicon Gratings. *J. Microelectromechanical Syst.* **25,** 963–967 (2016).

56. Abdolvand, R. & Ayazi, F. An advanced reactive ion etching process for very high aspect-ratio sub-micron wide trenches in silicon. *Sensors Actuators, A Phys.* **144,** 109–116 (2008).

57. Bruccoleri, A. *et al.* Fabrication of nanoscale, high throughput, high aspect ratio freestanding gratings. *J. Vac. Sci. Technol. B Microelectron. Nanom. Struct.* **30,** 06FF03 (2012).

58. David, C. *et al.* Fabrication of diffraction gratings for hard X-ray phase contrast imaging. *Microelectron. Eng.* **84,** 1172–1177 (2007).

59. Yun, W. *et al.* Nanometer focusing of hard x rays by phase zone plates. *Rev. Sci. Instrum.* **70,** 2238 (1999).

60. Schattenburg, M. L., Anderson, E. H. & Smith, H. I. X-ray/VUV transmission gratings for astrophysical and laboratory applications. *Phys. Scr.* **41,** 13–20 (1990).

61. Noda, D. *et al.* Fabrication of large area diffraction grating using LIGA process. *Microsyst. Technol.* **14,** 1311–1315 (2008).

62. Gorelick, S., Vila-Comamala, J., Guzenko, V. A. & David, C. High aspect ratio nanostructuring by high energy electrons and electroplating. *Microelectron. Eng.* **88,** 2259–2262 (2011).

63. Znati, S. *et al.* Electrodeposition of Gold to Conformally Fill High-Aspect-Ratio Nanometric Silicon Grating Trenches: A Comparison of Pulsed and Direct Current Protocols. *J. Surf. Eng. Mater. Adv. Technol.* **5,** 207–213 (2015).